Spatiotemporal variations of the components of seismic hazard in the Chilean subduction zone

by

Carlos F. Herrera Ramírez

B.Sc., Universidad de Concepción, 2013

M.Sc., Universidad de Chile, 2016

A Dissertation Submitted in Partial Fulfillment of the Requirements for the Degree of

DOCTOR OF PHILOSOPHY

in the School of Earth and Ocean Sciences

Spatiotemporal variations of the components of seismic hazard in the Chilean subduction zone

by

Carlos F. Herrera Ramírez

B.Sc., Universidad de Concepción, 2013

M.Sc., Universidad de Chile, 2016

Supervisory committee:

Dr. John F. Cassidy *(School of Earth and Ocean Sciences)*
Co-Supervisor

Dr. Stan E. Dosso *(School of Earth and Ocean Sciences)*
Co-Supervisor

Dr. Jan Dettmer *(School of Earth and Ocean Sciences)*
Academic Unit Member

Dr. Michel Lefebvre *(Department of Physics and Astronomy)*
Non-Unit Member

Abstract

This dissertation presents an analysis of the spatiotemporal variations of strong ground shaking and style of faulting at regional scales in the Chilean subduction zone. These properties are part of the two main components of seismic hazard: ground motions and seismic source characterization. Results are interpreted to be related to the tectonic dynamics and heterogeneities in the region.

The ground motion component was evaluated using residual analysis between observed and predicted earthquake strong ground motions. By analyzing strong motions of interplate earthquakes along the Chilean subduction zone (from the northern border to the tectonic triple junction in the south), we corroborate the better predictive performance of locally-derived ground motion models over globally-derived models. The results presented here show a stronger short-period radiation generated by deeper interplate earthquakes in north and central Chile, which is not currently considered in local ground motion models. We interpret this depth-dependent radiation pattern as a result of frictional variations on the plate interface. Additionally, it is shown that not every aftershock sequence following a large interplate earthquake exhibits predominantly weaker short-period radiation, which could be dependent on whether there was precursory activity before the mainshock. This work also outlines the need of developing local ground motion models for crustal earthquakes, since ground motion observations from the M_W 5.7 Pica earthquake (a crustal reverse-oblique event in northern Chile with a large stress drop) are significantly larger than predictions from current global models, particularly at short periods.

The seismic source component was assessed for crustal earthquakes in northern Chile. Clear regionalization is found in the spatial patterns of style of faulting and the tectonic stress field. The coastal region exhibits a clear margin-parallel compressional regime shown by the mostly reverse and strike-slip earthquakes in this area, while the analyzed

portion of the Andean Precordillera shows a strike-slip regime with a compressional direction nearly parallel to the plate convergence direction. We interpret these two tectonic regimes as a result of the concave shape of the subduction margin and the effect of local topography, respectively. Our results show that these regimes do not show any temporal change during the ∼10 year analysis period, and likely have remained stationary for the last 10 Ma. Although the earthquake recurrence relations presented in this work show that crustal earthquakes happen less frequently and at smaller magnitudes than interplate and intraplate earthquakes in northern Chile, crustal earthquakes still pose an important hazard, with the possibility of occurrence of more earthquakes with damaging-level ground accelerations, such as the Pica earthquake.

Contents

List of Tables

List of Figures

Acknowledgements

This dissertation and the related publications are a reality thanks to the constant guidance and support from my co-supervisors John Cassidy and Stan Dosso. The very useful discussions with them almost every week, and their accurate feedback and teachings were essential to develop high-quality research. I also appreciate the numerous opportunities that they gave me to teach, to attend conferences, and to meet colleagues. I finish my doctorate program with a considerably wider experience than I could ever expected.

I also acknowledge the funding from the Natural Sciences and Engineering Research Council of Canada (NSERC) Discovery Grants, which I received from my co-supervisors, as well as funding from University of Victoria Graduate Awards and Fellowships. These sources funded my full stay as a graduate student in Canada, as well as several conference trips and purchase of computer equipment for research.

I also thank my additional committee members: Jan Dettmer for his throughout reviews that improved any weak point that we may have missed, and Michel Lefebvre, whose objective point of view from outside my discipline encouraged me to develop research that can be clear and useful for a wider audience.

This dissertation is a compilation of three research projects, and I would not have completed them without the valuable collaboration of my additional coauthors: Nicolás Bastías, Tuna Onur, Wasja Bloch, Christian Sippl, Pablo Salazar, Efraín Rivera, Sergio Ruiz, and Hannes Vasyura-Bathke. Each of them contributed with additional ideas, codes, and calculations that I could not have done by myself in such a short time.

A great advantage of studying Geophysics at the University of Victoria is the networking with more professors and fellow graduate students, as well as with research scientists at the Pacific Geoscience Centre (PGC). I am greatly thankful for all the productive discussions in the PGC group meetings, as well as for the camaraderie during break times or special events.

And last but not least, I thank God for His blessings and for the opportunities to keep exploring the marvels of nature.

Dedication

This work is dedicated to my parents: Cleria and Carlos.
Even from the long distance I always received their constant support and encouragement,
which was essential for me to keep going forward.

I also dedicate this work to the numerous professors and colleagues that I met
in all the institutions that I went to.
Their teachings and advice guided me through this amazing journey in science,
and helped me to succeed during my education, culminating with this doctorate work.

Chapter 1

Introduction

1.1 Overview and motivation

The Chilean subduction zone is one of the most seismically active regions in the world. Interplate, intraplate, and crustal earthquakes occur frequently in the region, favored by the relatively fast convergence rate (Kendrick et al., 2003) and fairly cold subducting slab (Wada and Wang, 2009). For this reason, correctly quantifying the seismic hazard generated by this activity becomes critical to reduce the associated risk to population. Seismic hazard has two main components: earthquake ground motions (e.g., ground shaking intensities, site effects) and seismic sources (e.g., style of faulting, earthquake recurrence, spatial seismicity patterns). Significant progress has been accomplished in the last few decades to better understand these hazard components in Chile. However, newly released databases have shown that there are still patterns and characteristics of seismicity that have not been fully studied. This dissertation aims to fill some of those gaps in the current knowledge of strong ground motions and seismicity characterization in the Chilean subduction zone.

The frequent occurrence of significant $M_W \geq 4.5$ interplate and intraplate earthquakes in Chile has led to the development of local ground motion models (GMM) for these events (e.g., Idini et al., 2017; Montalva et al., 2017). GMMs are essential to quantify the ground motion component of seismic hazard and they are especially useful for seismological and

engineering applications, since they provide ground shaking intensity predictions and their uncertainties for a variety of earthquake scenarios and site conditions.

Local interplate GMMs have proven to be a better representation of observed ground motions from interplate events in northern Chile than globally derived GMMs, and they have been used to identify spatiotemporal variations of ground motions in that region (Piña-Valdés et al., 2018b). Results have shown an increase of short-period radiation by deeper interplate events, as well as a drop of short period radiation before the 2014 M_W 8.1 Iquique earthquake, which continued during its aftershock sequence. In addition to the interpretations of the tectonic dynamics driving these variations, these results outline the need of incorporating depth variation terms in the GMMs to account for the increasing short-period radiation with depth. However, the cited study is restricted only to northern Chile, using a limited number of seismic stations. The outstanding question to be addressed is whether these patterns are also observed in central and southern Chile, where hundreds of stations have recorded many significant interplate events, including the 2015 M_W 8.3 Illapel (Ruiz et al., 2016) and 2010 M_W 8.8 Maule (Delouis et al., 2010) earthquakes. Extending this evaluation of earthquake ground motions to the entire Chilean portion of the Nazca subduction zone will allow a more comprehensive analysis of ground shaking patterns at a national scale, which will include more large earthquakes and will provide additional observations that can guide future improvements of local GMMs. Overall, this analysis will drive the creation of a nationwide database of strong ground motions and station characterization in terms of site conditions, which will be useful for seismology and engineering applications.

Another subject that is not well studied is the ground motion characterization of earthquakes within the continental crust. The lack of a large enough waveform database due to the infrequent occurrence of $M_W \geq 5.0$ crustal earthquakes has impeded the development of local crustal GMMs. Currently, any ground motion evaluation of crustal earthquakes

in Chile has to be done with GMMs developed with a global database. Onshore crustal events can pose a large hazard to population due to the rupture proximity to cities and towns. The 2008 M_W 5.7 Pica earthquake in northern Chile is such an example. Studying its ground motions will contribute to a better understanding of their properties (e.g., intensity levels and variations in frequency), and will provide an opportunity to evaluate the predictive performance of the global GMMs currently used for crustal earthquakes in Chile.

Regarding the characterization of the seismic source component of hazard, interplate and intraplate earthquakes have historically reached the largest magnitudes in Chile (Ruiz and Madariaga, 2018). Interplate earthquakes are characterized by reverse mechanisms of gentle fault dip (thrust mechanism) aligned with the plate interface geometry, and intraplate earthquakes have mostly normal mechanisms, since they occur within the subducting oceanic plate under the tension of the slab-pull process. However, a comprehensive source characterization of crustal seismicity in Chile is still a pending subject. Currently, only northern Chile has been properly instrumented with dense seismic networks to detect and locate with high accuracy thousands of crustal earthquakes (Bloch et al., 2014; Sippl et al., 2018). In Cascadia, another concave subduction zone with well studied crustal seismicity, it was found that crustal events exhibit a variety of fault mechanisms, mostly reverse and strike slip (Balfour et al., 2011). Results showed a margin-perpendicular compression within the crust near the trench, which shifted to margin-parallel compression further inland. With the recently published earthquake catalogues and available waveform database, it is now possible to carry out a similar study in northern Chile to investigate whether this region shows similar patterns. Dominant faulting regimes in the crust and their associated tectonic stress field can be obtained from smaller earthquakes, while the rupture properties of the largest and more hazardous events can be obtained via waveform modelling. For example, the Pica earthquake is one of the largest onshore crustal earthquakes recorded with modern networks. This type of earthquakes can pose an important hazard to population and critical infrastructure if they occur nearby. The rupture proper-

ties (e.g., fault plane, rupture slip, rupture area, stress drop) of this event have not been extensively studied yet, and their determination can provide helpful insights on the source characteristics of the largest crustal events. Additionally, recurrence parameters of these crustal events can be calculated from available global and local catalogues, which can also be compared with the recurrence of interplate and intraplate events. These occurrence rates, in addition to the style of faulting and rupture characterization of earthquakes, are essential in the formulation of the seismic source component of hazard.

1.2 Dissertation structure

This dissertation is based on three core chapters, each corresponding to a research project either published or ready to submit to a peer-reviewed journal. Therefore, each chapter describes its own motivation, data, methods, results, and conclusions. Although these are three distinct projects, their main findings have the common aim of addressing the questions outlined in the motivation of this dissertation. These chapters contribute new insights on their respective fields of study, and their combination provides an improved understanding of the seismic hazard in Chile, which could be applicable to other subduction zones globally.

This is the outline of the three chapters that comprise the core of this dissertation:

- **Chapter 2:** Spatiotemporal variations of earthquake ground motions are evaluated along the Chilean portion of the Nazca subduction under South America (extending ∼3100 km). The database consisted of $M_W \geq 4.0$ interplate earthquakes that occurred during the last decade. Residual analysis between observed and predicted ground motions was used to analyze spatiotemporal variability patterns. The auxiliary material of this project can be found in Appendix A.

- **Chapter 3:** We investigate the dominant style of faulting and the stress field within the continental crust in northern Chile. Over 800 focal mechanisms of local crustal earthquakes were calculated and then inverted to obtain stress tensors. Stress orientations are analyzed in space and in time. The auxiliary material of this project can the found in Appendix B.

- **Chapter 4:** The 2008 M_W 5.7 Pica crustal earthquake is studied. This is the largest onshore crustal event included in the database of Chapter 3. Its large ground accelerations are analyzed through residual analysis, and its source characteristics (including the centroid moment tensor, rupture size, average slip, and stress drop) are inferred via waveform and S-wave spectra inversion. Its occurrence is discussed within the seismotectonic context of northern Chile, which includes an earthquake recurrence analysis. The auxiliary material of this project can the found in Appendix C.

Chapter 2

Ground motion evaluation of moderate and large interplate earthquakes along the Chilean subduction zone

2.1 Article information

2.1.1 Author and coauthor contributions

The research presented in this chapter was published in the Bulletin of the Seismological Society of America (Herrera et al., 2020). The text and figures are taken directly from that article. The author C. Herrera collected and analyzed all strong motion data. The author also designed and wrote the manuscript. Coauthors J. F. Cassidy, S. E. Dosso, and T. Onur contributed with editing assistance and review of the manuscript before submission. Coauthor N. Bastías calculated all new inferred V_{30} values reported in this work, and provided editing assistance on the manuscript.

2.1.2 Citation

Herrera C., Cassidy, J. F., Dosso, S. E., Bastías, N., and Onur, T. (2020). Ground-Motion Evaluation of Moderate and Large Interface Earthquakes along the Chilean Subduction Zone. *Bulletin of the Seismological Society of America*, 110 (6), 2693–2710. DOI: https://doi.org/10.1785/0120190265

2.1.3 Author's names and affiliations

Carlos Herrera[1], John F. Cassidy[1,2], Stan E. Dosso[1], Nicolás Bastías[3], and Tuna Onur[4]

[1] *School of Earth and Ocean Sciences, University of Victoria, Victoria, BC, Canada*

[2] *Pacific Geoscience Centre, Geological Survey of Canada, Natural Resources Canada, Sidney, BC, Canada*

[3] *Gensis Ingeniería, Concepción, Chile*

[4] *Onur Seemann Consulting, Inc., Victoria, BC, Canada*

2.2 Abstract

Strong-motion observations of recent interplate earthquakes along the Chilean subduction zone are evaluated with two ground motion models (GMM). One GMM was developed with Chilean data and the other with global data. The GMM developed with local Chilean data is found to have an overall better prediction performance than the GMM developed using a global data set. Using residual analysis with the Chilean GMM as reference model due to its better performance, clear indications of an increase of short-period radiation for deeper earthquakes in north and central Chile were found, which may be related to frictional features on the plate interface such as interseismic coupling, as found previously for other regions, such as Japan. Also, the Iquique earthquake, which featured a clear precur-

sory slow-slip event, exhibits mostly negative between-event residuals at short periods for earthquakes before and after the mainshock, indicating predominantly weaker short-period radiation. However, this trend is not observed in the aftershock sequence of the Illapel earthquake, which did not feature a significant slow-slip event nor precursory seismicity in its rupture area. Finally, a poor predictive performance was found for the Chilean GMM in southern Chile, overpredicting most of the observations. Based on these results, it is proposed that future local GMMs should include corrections for depth, regional effects and include earthquakes from southern Chile, as new data are becoming available in this region.

2.3 Introduction

The Chilean subduction zone is one of the most seismically active regions in the world. The Nazca plate subducts beneath the South American plate with a convergence rate of ∼70 mm/yr (e.g., Kendrick et al., 2003; Vigny et al., 2009), resulting in frequent occurrence of interplate (thrust), intraplate, and crustal earthquakes along the subduction zone. Recent and historical large earthquakes have been reported and analyzed along Chile from the northern border at latitude 18°S to the triple junction in the south at 46°S (e.g., Lomnitz, 2004; Ruiz and Madariaga, 2018). Interplate earthquakes can reach the largest magnitudes, causing large surface ground motions and severe tsunamis that can significantly affect the population.

Because of the significant seismic hazard along the country, building codes have been improved on an ongoing basis, and seismic hazard assessments are carried out frequently, in which ground motion models (GMMs) constitute an essential component. GMMs predict the ground-motion intensity at a given site based on parameters related to the earthquake source, path effects, and site effects. In Chile, Ruiz and Saragoni (2005) developed the

first attenuation relations using Chilean interplate and intraplate earthquakes. However, their model only predicts peak ground acceleration (PGA), and it does not have a published standard deviation, making it unsuitable for modern GMM evaluation techniques. Contreras and Boroschek (2012) developed the first GMM for Chile that included the prediction of spectral accelerations at specific periods (SA(T)), in addition to PGA. Their model was developed using only Chilean interplate earthquakes from 1985 to 2010, including data from the 2010 M_W 8.8 Maule earthquake. But it has some limitations, such as an oversimplification of site effects to only two classes and a narrow range of SA(T) with periods between 0.04 and 2 s. Later, Idini et al. (2017) developed a new GMM for Chile that predicts PGA and SA(T) in a broader range of periods (between 0.01 and 10 s), using a larger data set that incorporated interplate and intraplate earthquakes from 1985 to 2014, including the 2014 M_W 8.1 Iquique earthquake. However, the site-effect term of this GMM is not appropriate for sites with $V_{S30} < 400$ m/s, which is the case of many seismic stations in Chile. In the same year, Montalva et al. (2017) proposed another GMM for interplate and intraplate events in Chile, predicting PGA and SA(T) between 0.02 and 10 s. They used a larger strong-motion data set and a wider V_{S30} range (108 m/s $< V_{S30} <$ 1951 m/s) than Idini et al. (2017), with a functional form that follows Abrahamson et al. (2016). Additionally, both the Idini et al. (2017) and Montalva et al. (2017) models separate the between-event and within-event residual components, which is essential to properly separate source and path effects.

With the growing strong-motion data set available for Chile, several studies have evaluated the GMM predictive performance in the country. Bastías et al. (2015) evaluated four GMMs with a nationwide ground-motion data set. Two of these models were derived using global data (Atkinson and Boore, 2003, 2008; Abrahamson et al., 2016), one was derived using only Chilean data (Contreras and Boroschek, 2012), and one was derived using Japanese data (Zhao et al., 2006). From those five models, Bastías et al. (2015) found that the BC Hydro GMM (Abrahamson et al., 2016) shows the best fit to observed

ground motions at long periods, whereas Zhao et al. (2006) shows the best fit at short periods. Piña-Valdés et al. (2018b) carried out a ground-motion evaluation in northern Chile, taking advantage of the data provided by a permanent seismic network deployed on rock since 2006. They used two GMMs (Abrahamson et al., 2016; Montalva et al., 2017) to evaluate the observed ground motions, and found that the Abrahamson et al. (2016) GMM better describes observations at short periods, whereas the Montalva et al. (2017) GMM better fits observations at long periods. Piña-Valdés et al. (2018b) also found an increase of short-period ground-motion radiation with earthquake depth, as well as a decrease of short-period ground motions prior to the 2014 M_W 8.1 Iquique earthquake, which can provide clues about the variation of frictional properties on the plate interface before the mainshock.

In this article, the ground-motion evaluation is expanded to the entire Chilean portion of the Nazca subduction zone, dividing the country into three regions: north, central, and south. Making use of the increasing amount of waveform data available from the deployment of new digital seismic stations over the last decade, an overall ground-motion evaluation is carried out using two GMMs: one derived with a local database and another derived with a global database. Given its advantages with respect to other Chilean GMMs, the Montalva et al. (2017) interplate GMM is used as the local model. The BC Hydro interplate GMM (Abrahamson et al., 2016) is chosen as global model, which has been used in similar studies in Chile (e.g., Piña-Valdés et al. (2018b)). This model includes between-event and within-event separation and its V_{S30} range (90 m/s $\leq V_{S30} \leq$ 1800 m/s) is similar to the V_{S30} range of the Montalva et al. (2017) model. The Abrahamson et al. (2016) model was developed using an ergodic assumption, which is, the variability of ground motions at many (global) sites is identical to the variability at a single site. Conversely, the Montalva et al. (2017) model can be considered partially non-ergodic, because it is based on the specific attenuation properties for Chilean earthquakes, and, as such, should have reduced variability. The Montalva et al. (2017) GMM was developed using

$M_W \geq 5.0$ Chilean interplate events not deeper than 50 km, whereas the Abrahamson et al. (2016) GMM was developed using global $M_W \geq 6.0$ interplate events in the same depth range, some of them from Chile. The BC Hydro GMM has also been updated (Abrahamson et al., 2018), using a larger database and introducing regionalization. However, regional terms for locations other than Cascadia were still incomplete at the time of this study, because the updated GMM was primarily intended for application to the Cascadia region.

Between these two GMMs, the model that best fits the national scale observed data is used to study ground-motion variations in space and time along Chile. The possible causes of these variations are studied by analyzing the source, path, and site components of the ground motions, and their correlation with other geophysical data sets.

2.4 Study area, seismic networks, and earthquake catalogue

Instead of evaluating ground motions along the entire Chilean subduction zone all at once, the country is divided into three regions that are analyzed separately: north, central, and south (see maps in Figure 2.1), to explore possible regional differences. Northern Chile comprises the region between latitudes 18°S and 27°S, which includes the 2007 M_W 7.7 Tocopilla and 2014 M_W 8.1 Iquique earthquakes. The 27°S limit is roughly equidistant between the Tocopilla and the 2015 M_W 8.3 Illapel earthquakes. Central Chile comprises the region between latitudes 27°S and 39°S, which includes the 2010 M_W 8.8 Maule and the Illapel earthquakes. The 39°S limit corresponds to the southern edge of the Maule rupture area, which also roughly coincides with the southern limit of the data used to develop the Montalva et al. (2017) GMM. Southern Chile is a smaller region between

latitudes 39°S and 45°S, which includes the 2016 M_W 7.6 Chiloé earthquake. Earthquake occurrence in southern Chile is less frequent, and events in this region have not been used for GMM development or evaluation to date. The 45°S limit is close to the triple junction, defining the southern edge of the subducting Nazca plate.

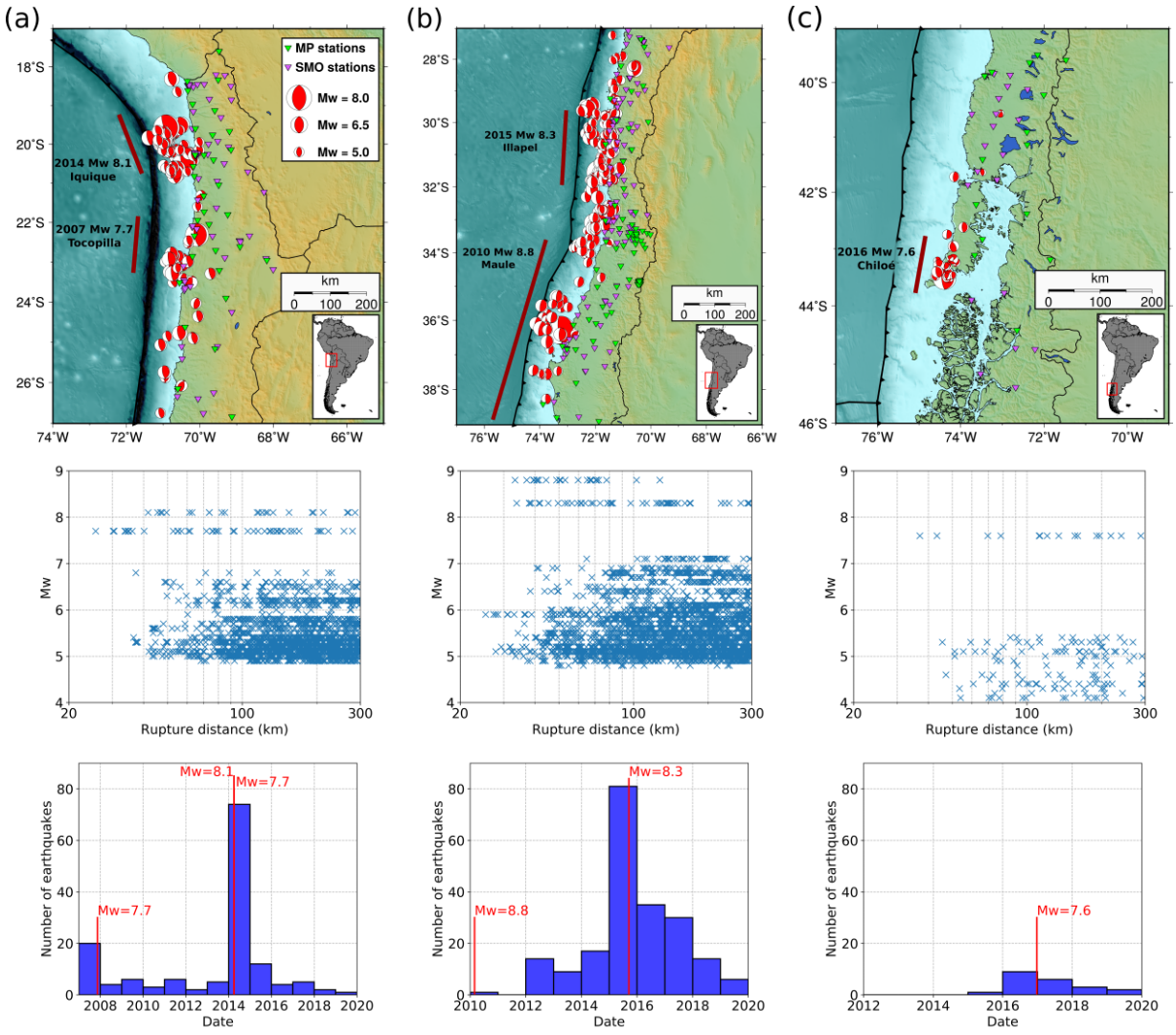

Figure 2.1: Nationwide database divided in three regions, as shown in columns (a), (b), and (c), for northern, central, and southern Chile, respectively. The maps in the top row show the lower-hemisphere projection of the focal mechanisms of interplate earthquakes. MP and SMO correspond to multiparametric and strong-motion-only stations, respectively. Rupture lengths along strike of the $M_W \geq 7.5$ megathrust earthquakes are also highlighted. The middle row shows the distribution of observations as a function of earthquake magnitude and rupture distance. The bottom row shows the earthquake occurrence as a function of time, with the main megathrust earthquakes highlighted. The red rectangle in the small inset shows the location of the map within South America.

New digital seismic stations are being deployed on an ongoing basis by the Centro Sismológico Nacional (CSN) and its partner institutions in Chile. The country is covered

by several seismic networks of continually recording multiparametric stations (broadband seismometer, accelerometer, and other sensors), and their data are available through the International Federation of Digital Seismograph Networks (FDSN). The CSN also manages another network of earthquake-triggered strong-motion stations (accelerometer only). The database used in this work includes strong-motion waveforms from four continually recording networks: Chilean National Seismic Network (FDSN code: C), Red Sismológica Nacional (Universidad de Chile, 2012), GEOFON Seismic Network (GEOFON Data Centre, 1993), and Integrated Plate Boundary Observatory Chile (GFZ and CNRS-INSU, 2006), as well as the earthquake-triggered strong-motion network of the CSN (see Data and Resources section). The maps in Figure 2.1 show all the stations included in these networks.

The first stage of the earthquake selection is based on the availability of enough strong-motion data and published focal mechanism solutions in each of the three regions. At the time of this study, there is a considerable amount of digital waveform data available from seismic networks since 2007 in northern Chile, since 2012 in central Chile, and since 2015 in southern Chile. Data of the 2010 Maule earthquake in central Chile were also used, because this event was well recorded by the earthquake-triggered RENADIC strong-motion network (see Data and Resources section). Within these dates, $M_W \geq 4.8$ events not deeper than 70 km were selected. The Global Centroid Moment Tensor (GCMT) catalogue was used to obtain the nodal planes and moment magnitudes of these events, but the CSN catalogue was used to obtain their locations, because we consider these to be more accurate.

Very few earthquakes are reported by the GCMT catalogue in southern Chile to date. To increase the number of events with moment magnitude and focal mechanisms in southern Chile, the local magnitude of the events reported by the CSN were converted to moment magnitude using the relationships proposed by Leyton et al. (2018), because

southern Chile is included in their analyses, and the events with $M_W \geq 4.0$ were selected. Then, their focal mechanisms were estimated using HASH (Hardebeck and Shearer, 2002, 2003) by inverting P-wave polarities and S/P amplitude ratios. For this, velocity time series from broadband or from integrated strong-motion channels were used. To highlight the P-wave polarities for visual picking, the velocity records were integrated, and a 1 Hz high-pass Butterworth filter was applied. The S/P ratios were calculated by dividing the maximum S- and P-wave amplitudes obtained from the Cartesian sum of the three components. Azimuth and takeoff angles were computed using ray propagation through a regional 1-D velocity model provided by the CSN for this region. Finally, polarities and amplitude ratios were inverted with HASH to find the focal mechanism solution that best fits the observed radiation pattern. The stability of the solution was evaluated by rerunning the inversion with randomly perturbed azimuth and takeoff angles with a maximum deviation of 5°. Estimating focal mechanisms was particularly challenging in this region due to the small number of stations and earthquakes. Also, some of these stations are earthquake triggered and, therefore, may not record some small events. Because of these limitations in the data set, focal mechanisms were calculated for earthquakes with at least five unambiguous first-motion measurements. Only few events were considered with three and four first-motion observations, after carefully evaluating the station distribution and the stability of the inversion. In total, focal mechanism solutions of 46 earthquakes were properly constrained.

The second stage is the selection of only interplate events for analysis. The classical expert classification method based on earthquake location and focal mechanisms (e.g., Bastías and Montalva, 2016) was used to select earthquakes. Earthquakes with reverse and reverse-oblique mechanism were selected based on the rake angle, and, considering their location, we assumed that these are interplate earthquakes in the considered depth range for analysis.

After this two-stage earthquake selection, the following earthquake catalogues and observations were obtained for the three regions:

- In northern Chile, the data selection resulted in 2207 observations from 144 $M_W \geq 4.8$ earthquakes. Earthquake occurrence is strongly influenced in space and time by the 2007 M_W 7.7 Tocopilla and 2014 M_W 8.1 Iquique earthquakes (see map and graphs in Figure 2.1a).

- In central Chile, 2928 observations from 207 $M_W \geq 4.8$ earthquakes were obtained, which constitutes the largest regional data set. The 2015 M_W 8.3 Illapel earthquake and its aftershocks contributed significantly to the catalogue. In this region, earthquakes are more evenly distributed in space and time, compared with northern Chile. After 2012, several significant events still occur on the M_W 8.8 Maule rupture area (see Figure 2.1b).

- In southern Chile, 143 observations from 21 $M_W \geq 4.0$ earthquakes were obtained. Events are less frequent in this region, and the catalogue is dominated by the occurrence of the 2016 M_W 7.6 Chiloé earthquake and its aftershocks (see Figure 2.1c). Focal mechanism solutions of four interplate events were reported by the GCMT, and the solutions for the rest were obtained from the focal mechanism calculation carried out in this work. From the calculated focal mechanisms, 17 were selected as interplate, which are reported in Figure A.1 of Appendix A.

2.5 Data processing, distances, and site characterization

Prior to signal processing, each waveform record was trimmed to the relevant part of the earthquake signal and deconvolved with the instrument response to obtain physical units of acceleration. Then, the sampling rate of all records was standardized to a common

value of 100 Hz, the mean and linear trend were removed, and a noncausal fourth-order Butterworth band-pass filter between 0.2 and 25 Hz was applied. This frequency band was chosen to be consistent with the filter already applied to the processed RENADIC records of the 2007 Tocopilla and 2010 Maule earthquakes. Finally, a Hanning taper was applied at each end of the seismograms.

Strong ground motions can be described in terms of various intensity measures, including PGA and SA(T). The observed PGA at each station was obtained by calculating the geometric mean of the maximum accelerations of the horizontal components (north–south and east–west). To obtain the observed SA(T) at each station, a 5% damped response spectrum was applied to each horizontal component, following the method of Nigam and Jennings (1969), and SA(T) was calculated as the geometric mean of the two horizontal response spectra.

The type of source–station distance must be the same as the distance defined in the GMM model parameters. The Abrahamson et al. (2016) and Montalva et al. (2017) GMMs use rupture distance, which is the distance from the station to the closest point on the earthquake rupture surface. To calculate the rupture distance of the set of observations, published rupture areas were used for the $M_W \geq 7.5$ earthquakes: 2007 M_W 7.7 Tocopilla (Béjar-Pizarro et al., 2010), 2010 M_W 8.8 Maule (Delouis et al., 2010), 2014 M_W 8.1 Iquique (Ruiz et al., 2014), 2015 M_W 8.3 Illapel (Ruiz et al., 2016), and 2016 M_W 7.6 Chiloé (Ruiz et al., 2017). For the smaller events with no published rupture areas, the relations proposed by Strasser et al. (2010) were used to obtain the rupture dimensions from moment magnitudes, following Bastías and Montalva (2016). Those ruptures were assumed to be centered at the hypocentre, and oriented based on the strike and dip of the rupture plane given by the focal mechanism. The rupture plane was identified from each focal mechanism based on its orientation with respect to the plate interface.

The main site parameter used by the GMMs in this case is the travel-time weighted average shear-wave velocity in the top 30 m (V_{S30}), which ideally should be measured for all stations. However, V_{S30} measurements are not available for many stations in Chile. To construct the site data set, a V_{S30} catalogue of the Chilean stations was compiled, starting with the values measured using surface-wave dispersion curve inversions (Kayen et al., 2014; Leyton et al., 2018). For the stations not included in those studies, we used the values inferred from the topographic slope and predominant frequency reported by Bastías and Montalva (2016). Finally, for the remaining stations without characterized V_{S30}, the method of Bastías and Montalva (2016) was used in this study to infer their V_{S30} and complete the current Chilean site database. Station locations were used for the topographic slope analysis, and strong-motion records of $M_W > 5.0$ earthquakes within 400 km of each station were used for the predominant frequency analysis. These new inferred V_{S30} values are reported in Table A.1 of Appendix A.

2.6 Overall ground-motion evaluation

The observed ground motions in the three Chilean regions were compared with the Montalva et al. (2017) interplate GMM (hereafter, Mea17) and the Abrahamson et al. (2016) BC Hydro interplate GMM (hereafter, Aea16). The GMMs are used to obtain the ground-motion predictions of each station–earthquake pair for PGA and SA(T) at periods 0.2, 0.5, and 2 s. These are native periods for both GMMs (no interpolation was required) located within the usable frequency of the filter applied to the observed records. These PGA and SA(T) predictions are compared with the observed values obtained from the response spectrum of each station–event pair for rupture distances less than 300 km, to be within the distance calibration range of both GMMs.

Observations and predictions are compared using residual analysis. Because a GMM can be represented by a standardized normal density function (zero mean, unit standard deviation), then normalized residuals are calculated. The normalized total residual $Z_t^{ij}(T)$ at station j for the earthquake i at period T is defined as:

$$Z_t^{ij}(T) = \frac{\log_e[I_{obs}^{ij}(T)] - \log_e[I_{pred}^{ij}(T)]}{\sigma(T)},$$

where $I_{obs}^{ij}(T)$ and $I_{pred}^{ij}(T)$ correspond to the observed and predicted ground motions at station j for the earthquake i at period T, respectively, and $\sigma(T)$ is the total standard deviation of the GMM at period T, usually provided in $\log_e$ units.

Total residuals (Z_t) can be separated into between-event residuals (Z_b) and within-event residuals (Z_w) (Abrahamson and Youngs, 1992; Strasser et al., 2009; Atik et al., 2010). Nonzero between-event residuals indicate that there is variability of complex earthquake source-related factors that are not accounted for by the corresponding GMM source parameters (magnitude, type of faulting, and source depth). Nonzero within-event residuals indicate that there is variability of path and site effects that could be caused by the complex tectonic and local structure that are not accounted for by the corresponding GMM path and site parameters (earthquake–station distance and site classification). The equations described in Piña-Valdés et al. (2018b) were used to calculate between-event and within-event residuals. The normalized between-event residual $Z_b^i(T)$ of the earthquake i at period T is defined as:

$$Z_b^i(T) = \frac{\psi(T) \cdot \sum_{j=1}^{n} \{\log_e[I_{obs}^{ij}(T)] - \log_e[I_{pred}^{ij}(T)]\}}{n \cdot \psi^2(T) + \phi^2(T)},$$

where n is the total number of stations that recorded the earthquake i. $\psi(T)$ and $\phi(T)$ are the standard deviations of the between-event and within-event components of the GMM at period T, respectively, both in $\log_e$ units. The between-event residual was calculated only for earthquakes that were recorded by at least four stations.

The normalized within-event residual $Z_w^{ij}(T)$ at station j for the earthquake i at period T is defined as:

$$Z_w^{ij}(T) = \frac{\log_e[I_{obs}^{ij}(T)] - \log_e[I_{pred}^{ij}(T)] - Z_b^i(T) \cdot \psi(T)}{\phi(T)}$$

Figure 2.2 summarizes the overall residual analysis in the three Chilean regions for both Aea16 and Mea17 GMMs. Normalized residuals are represented by histograms and their best-fit Gaussian distributions, which are compared with the GMMs, represented by the standard Gaussian distribution (zero mean, unit standard deviation). Based on the Z_t plots, the overall predictive performance of both models varies, depending on the periods and the region. The observed offset of the Z_t distribution with respect to the GMM distribution in some plots is mainly contributed by the offset of the Z_b component, related to earthquake source effects. Conversely, Z_w distributions show that both GMMs perform well for the path and site-effect component of ground motions in almost all cases, predicting well intensities (mean close to zero) and their variability (standard deviation close to one).

For northern Chile, Z_t and Z_b plots in Figure 2.2a show a slight intensity underprediction of Aea16 at all periods and an overprediction of Mea17 at PGA and SA(0.2). Figure A.2 shows Z_t and Z_b residuals with respect to different variables. As shown in Figure A.2, the Aea16 underprediction is contributed by the slightly larger number of positive residuals at all depths, rupture distances, and magnitudes, whereas the Mea17 overprediction at PGA and SA(0.2) is mostly contributed by the predominantly negative Z_t and Z_b residuals of $M_W < 7.0$ events between 10 and 50 km depth at these periods. No clear magnitude or event-to-station azimuth dependence is observed for Aea16 and Mea17 residuals in this region. But an increase of positive residuals is observed at depths greater than 45 km for both GMMs.

Figure 2.2b shows that Mea17 fits well the intensities and variabilities at all periods in

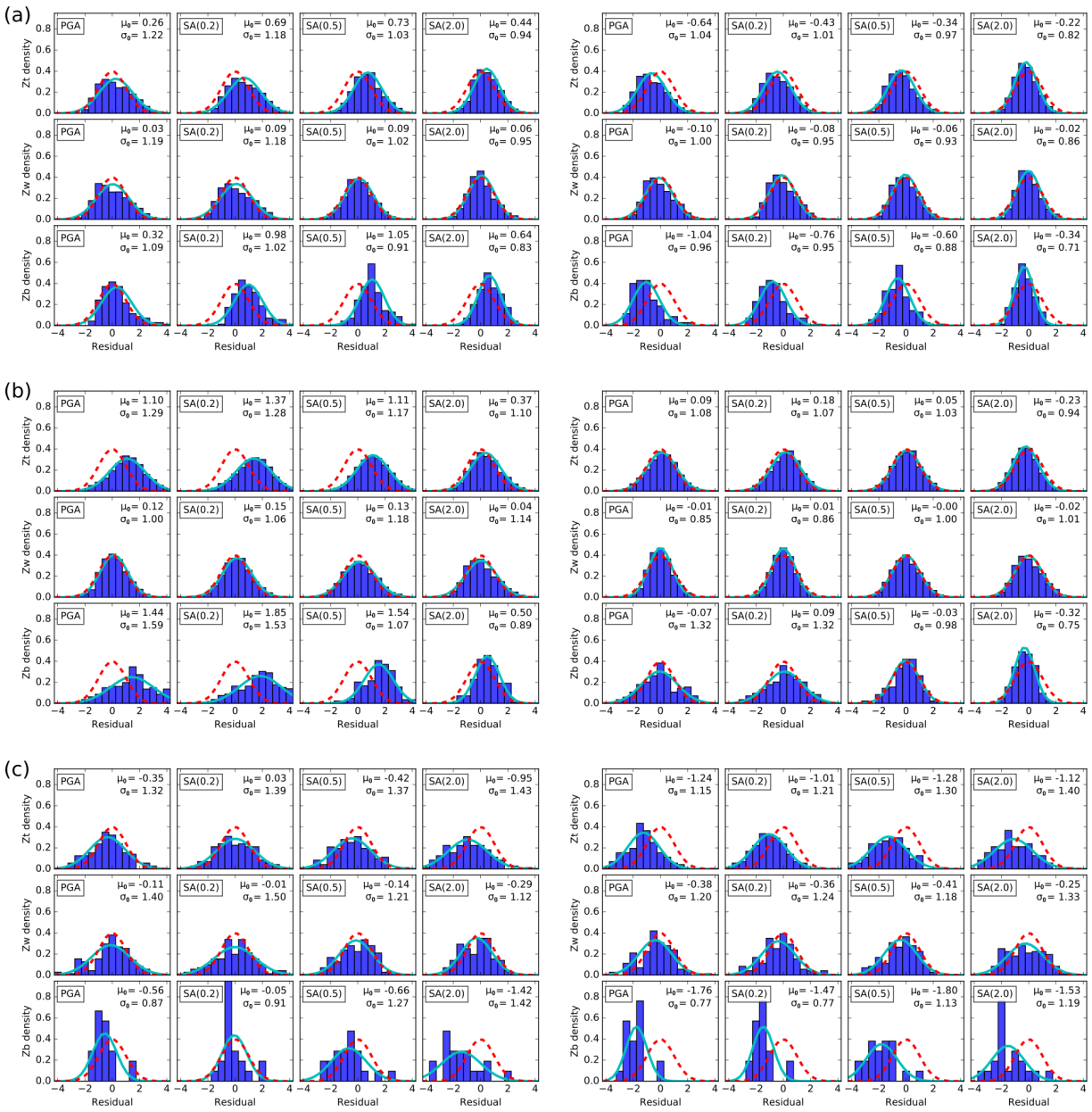

Figure 2.2: Total (Z_t), between-event (Z_b), and within-event (Z_w) histograms of residuals with respect to the Aea16 ground motion model (GMM) in the left column and the Mea17 GMM in the right column. Rows (a), (b), and (c) show comparisons for northern, central, and southern Chile, respectively. The histograms are fitted with Gaussian distributions. The mean (μ_0) and standard deviation (σ_0) of these distributions are also given. Dashed curves represent the normal density function of the GMM.

central Chile. But Aea16 underpredicts observations considerably, particularly at PGA, SA(0.2), and SA(0.5), as shown by Z_t and Z_b distributions. This is due to predominantly positive Aea16 residuals of $M_W < 7.5$ earthquakes at all depths and rupture distances. Only at SA(2.0), residuals are more aligned along zero (see Figure A.3), but in this case, Z_t residuals increase with rupture distance. Aea16 and Mea17 residuals in central Chile do not show any significant magnitude or azimuth dependence, but a clear increase of residuals with depth is observed, starting at approximately 40 km depth, particularly at PGA and SA(0.2).

Figure 2.2c shows that Mea17 overpredicts observations at all periods in southern Chile, as shown by the Z_t and Z_b distributions. The fit is slightly better for the Aea16 residuals. As shown in Figure A.4, the overprediction of Mea17 is contributed by the mostly negative residuals at all magnitudes, depths, rupture distances, and azimuths. Particularly, the deeper events (around 50 km depth) show the most negative Aea16 and Mea17 residuals at SA(0.5) and SA(2.0). In this case, magnitude dependence is observed for $4.0 \leq M_W \leq 6.0$, but not a clear azimuth dependence.

To quantitatively assess the predictive performance of the GMMs in the three regions, total residuals are evaluated using the likelihood (LH) method (Scherbaum et al., 2004) and the average sample log-likelihood (LLH) method (Scherbaum et al., 2009), which are both data-driven procedures. The LH method uses the concept of the LH value calculated for each residual value, which scales between 0 and 1. Based on the median of the LH values, Scherbaum et al. (2004) define four classes to evaluate the capability of a model to predict the observation: class A is the highest capability (median LH ≥ 0.4), class B is intermediate capability ($0.3 \leq$ median LH < 0.4), class C is the lowest accepted capability ($0.2 \leq$ median LH < 0.3), and class D is unacceptable capability (median LH < 0.2). The LLH method is based on information theory, which quantifies the Kullback–Leibler distance between observations and predictions. This distance is calculated as the loga-

rithm of the probability density function of the standard normal distribution evaluated at each normalized residual. The LLH value is obtained by averaging the Kullback–Leibler distances of all residuals. In this work, the negative average is used, which means that the closer the observations and the predictions, the lower the associated LLH value.

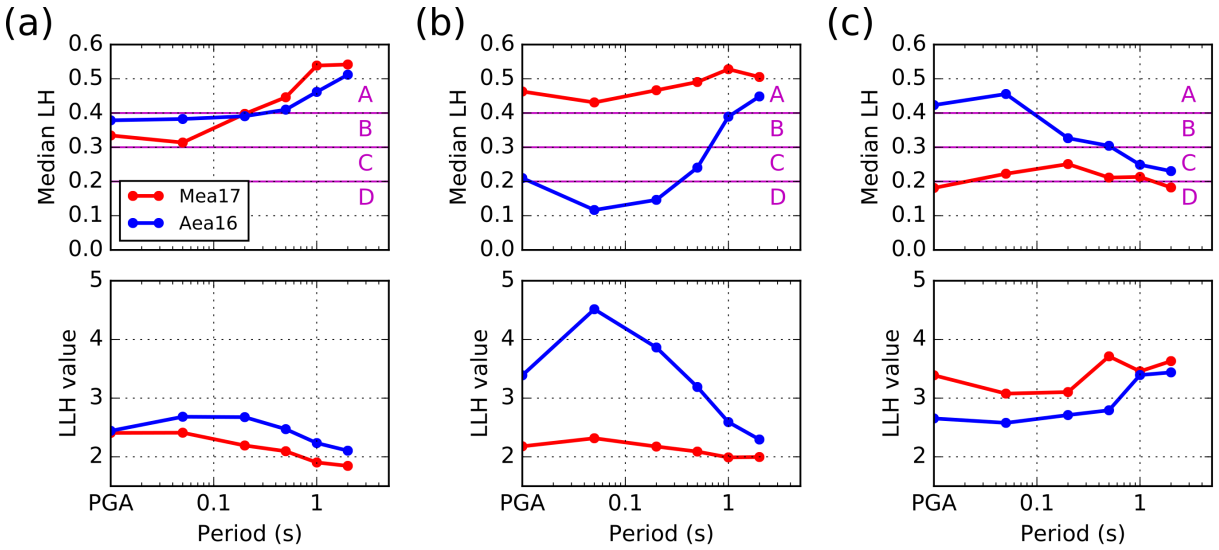

Figure 2.3: Goodness of fit of the GMMs calculated from total residuals at different periods. Columns (a), (b), and (c) show the evaluation for northern, central, and southern Chile, respectively. LH, likelihood; LLH, log likelihood.

To evaluate the predictive performance of both GMMs under equal conditions, a subset of observations was selected per region. Only residuals with rupture distances equal or less than 300 km from $M_W \geq 6.0$ earthquakes not deeper than 50 km were used, to be within the calibration ranges of both GMMs. Figure 2.3 shows the median LH and LLH values calculated from the total residuals. In general, results of both methods are consistent. Both GMMs perform generally well in northern Chile (Figure 2.3a). Aea16 performs better at short periods, and Mea17 performs better at long periods. Central Chile contains most of the observations. In this region, the Mea17 GMM shows the best overall fit to observations at all periods, with median LH values closer to 0.5 (higher capability classes) and low LLH values (Figure 2.3b), whereas Aea16 shows unacceptable fit capability at some periods. This is consistent with the Z_t distributions shown in Figure 2.2b. Results in southern Chile (Figure 2.3c) are based on just one $M_W > 6.0$ event (the

M_w 7.6 Chiloé earthquake). For this single event, Mea17 shows poor predictive performance at all periods, whereas Aea16 shows good performance only at short periods, with decreasing performance toward longer periods. These results are consistent with the Z_t distributions in this region in Figure 2.2c. The Abrahamson et al. (2018) (Aea18) GMM with Cascadia coefficients was also included in the goodness of fit analysis shown in Figure A.5. Overall, Aea18 performs better than Aea16, but still worse than Mea17 particularly in central Chile, where most of the data used in this work were recorded.

Considering that the Mea17 GMM generally provides a better fit to most of the observations in Chile, it was used as reference model in the spatiotemporal residual analysis per region to evaluate the ground-motion variations and discuss possible causes.

2.7 Northern Chile

Figure 2.2a (right) shows the total, within-event, and between-event residual distributions of Mea17 for northern Chile. The mean of the total residual distribution is shifted to negative values at short periods (PGA and 0.2 s), indicating that the model overpredicts ground-motion observations in this period range, mainly influenced by an overprediction of the source-related component of ground motions (between-event residuals), but its predictions are better for longer periods (0.5 and 2 s). Within-event residuals show that Mea17 fits well the site- and path-related component of ground motions at all periods, with a mean close to zero (adequate ground-motion intensity predictions) and standard deviations close to one (adequate description of ground-motion variability). Although total residuals in northern Chile do not show significant azimuth dependence, within-event residuals are larger at 90° azimuth at PGA and SA(0.2), then decrease toward 180° azimuth (see Figure A.6), indicating that stations located to the east of the earthquakes

recorded in average larger short-period ground motions. However, this change is small compared with the residual variability.

To evaluate a possible bias in single-station residuals, the site term proposed by Rodriguez-Marek et al. (2011) was calculated, which averages within-event residuals of the earthquakes recorded at each station. The site term is calculated for every station that recorded at least 10 earthquakes of the catalogue. Results of the seismic network in this region are shown in Figure A.7. The stations analyzed show no significant bias due to possible site effects. Stations with inferred V_{S30} tend to have slightly larger site term variability than those with measured V_{S30} by Leyton et al. (2018). Also, both groups of stations show a decrease of the site term standard deviation toward longer periods. Similar behavior was found for the KiK-net array in Japan by Stafford et al. (2017). Finally, no latitudinal dependency is observed in the site term, and no correlation is observed between the site term and V_{S30}. This lack of correlation could be due to already correcting for V_{S30} in the residual calculation. Therefore, the variability of the site term is due to site (or other) effects that are not modelled by the V_{S30}.

All these results are consistent with those reported by Piña-Valdés et al. (2018b), who also studied this region using a catalogue of $M_W \geq 4.0$ interplate events between 2007 and 2014. Piña-Valdés et al. (2018b) found an increase of between-event residuals with depth at short periods. They corroborated this by calculating ratios of the smoothed horizontal Fourier spectra of similar events at different depths, thus interpreting the variations of between-event residuals as changes of the frequency-dependent energy released from the earthquake source.

A similar approach as Piña-Valdés et al. (2018b) was followed to analyze the Mea17 between-event residual distribution of the selected $M_W \geq 4.8$ earthquake catalogue for northern Chile. Figure 2.4 shows these residuals as a function of magnitude, latitude,

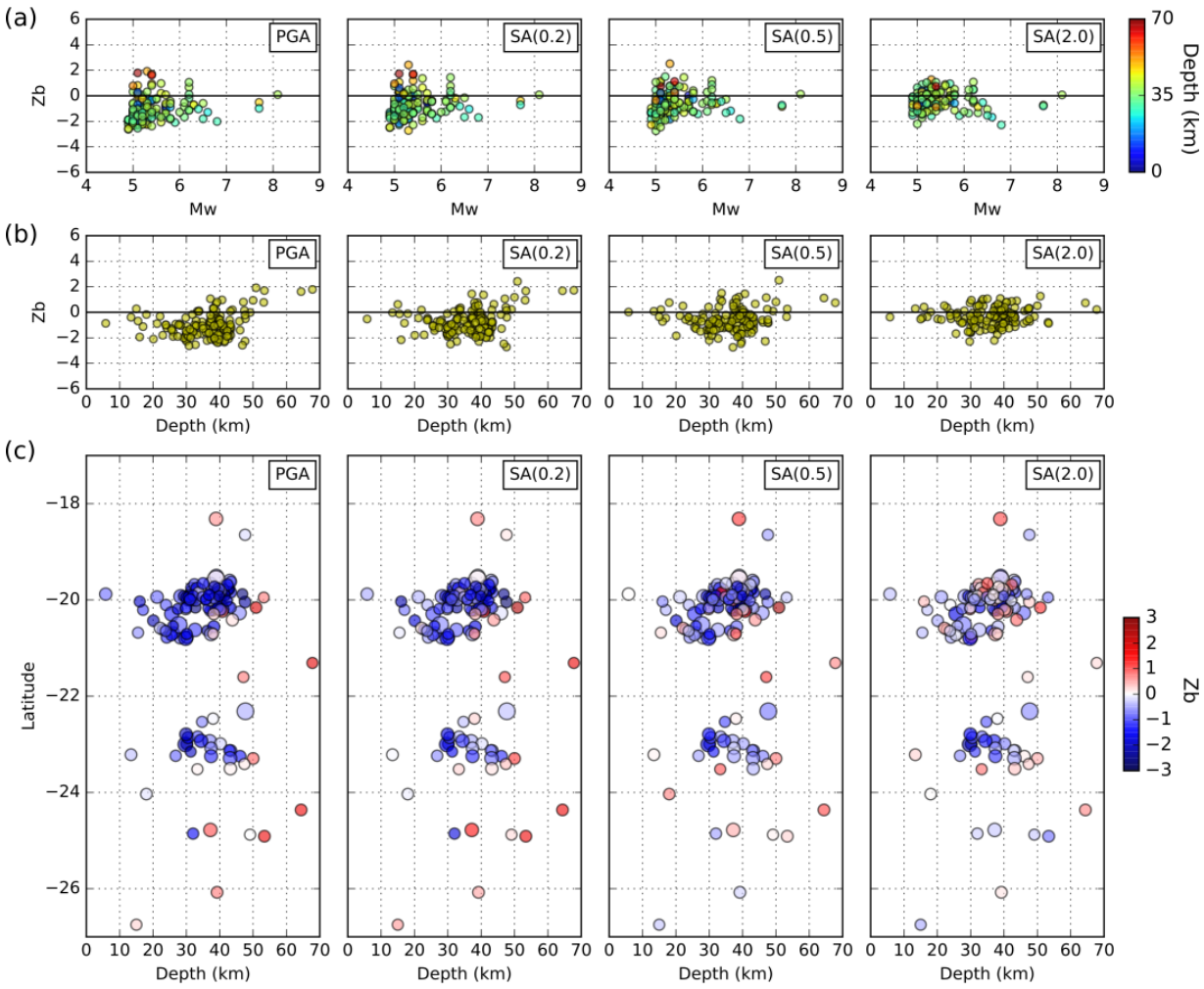

Figure 2.4: Mea17 between-event residuals in northern Chile for PGA, SA(0.2), SA(0.5), and SA(2.0). (a) Residuals as a function of moment magnitude and depth; (b) residuals as a function of depth; (c) residuals as a function of latitude and depth.

and depth. There is no magnitude dependency of the residuals at any period, and the larger positive residuals at short periods (PGA and 0.2 s) are mostly produced by deeper moderate-magnitude events, which is not obvious at longer periods (0.5 and 2 s). This is corroborated in Figures 2.4b and 2.4c. At short periods, only positive between-event residuals are observed toward greater depths. This suggests that deeper events radiate more short-period energy than shallower events, with a change occurring at around 45 km depth. This segmentation along dip is less evident at longer periods, in which residuals are more aligned around zero. However, Figure 2.4c shows that the earthquakes between latitudes 19°S and 21°S (M_W 8.1 Iquique earthquake area) tend to release more long-period energy than the earthquakes between latitudes 22°S and 24°S (M_W 7.7 Tocopilla

earthquake area), especially at SA(2.0).

Lay et al. (2012) proposed a down-dip segmentation of the plate interface based on observations of large interplate earthquake ruptures, where the short-period energy mainly emanated from the deeper rougher portion of the rupture, and the shallower smoother portion concentrates the larger coseismic displacement, but with weaker short-period radiation. Variations of these frictional features on the plate interface have shown some correlation with the interseismic coupling distribution (e.g., Hetland and Simons, 2010; Scholz and Campos, 2012), which indicates the degree of locking on the plate interface. In this context, Piña-Valdés et al. (2018a) found a negative correlation between interseismic coupling and short-period between-event residuals of interplate events in Japan, which could be also investigated in the Chilean subduction zone.

To assess whether the segmentation of short-period between-event residuals is related with interseismic coupling, the PGA between-event residuals of Mea17 were compared with the interseismic coupling model for Chile calculated by Metois et al. (2016). Figure 2.5a shows this comparison. Interseismic coupling is highly heterogeneous in northern Chile along strike and dip. Nevertheless, Figure 2.5a shows that events with larger positive residuals (stronger short-period radiation than predicted) tend to be mostly located at the deeper edges of the coupled zones, toward areas of low coupling. This suggests a first-order correlation between deeper earthquakes with more short-period radiation and lower coupling on the edge of the coupled patch. Some events with stronger short-period radiation also coincide with two important low coupling zones (LCZs) identified by Metois et al. (2016). Shallower earthquakes exhibit predominantly weaker short-period radiation, which would be expected to occur in areas of higher coupling. However, such correlation is not clear for the seismicity in the 2014 Iquique earthquake area. This area is particularly challenging for interpretation with the interseismic coupling model, because its resolution here is lower than elsewhere, especially toward the trench, where most of the seismicity

occurred. Compared with other megathrust earthquakes in Chile, Metois et al. (2016) also found a weaker correlation between high interseismic coupling and the Iquique coseismic rupture, which could be explained by the lack of model resolution or the effects of the slow-slip event in the area before the mainshock.

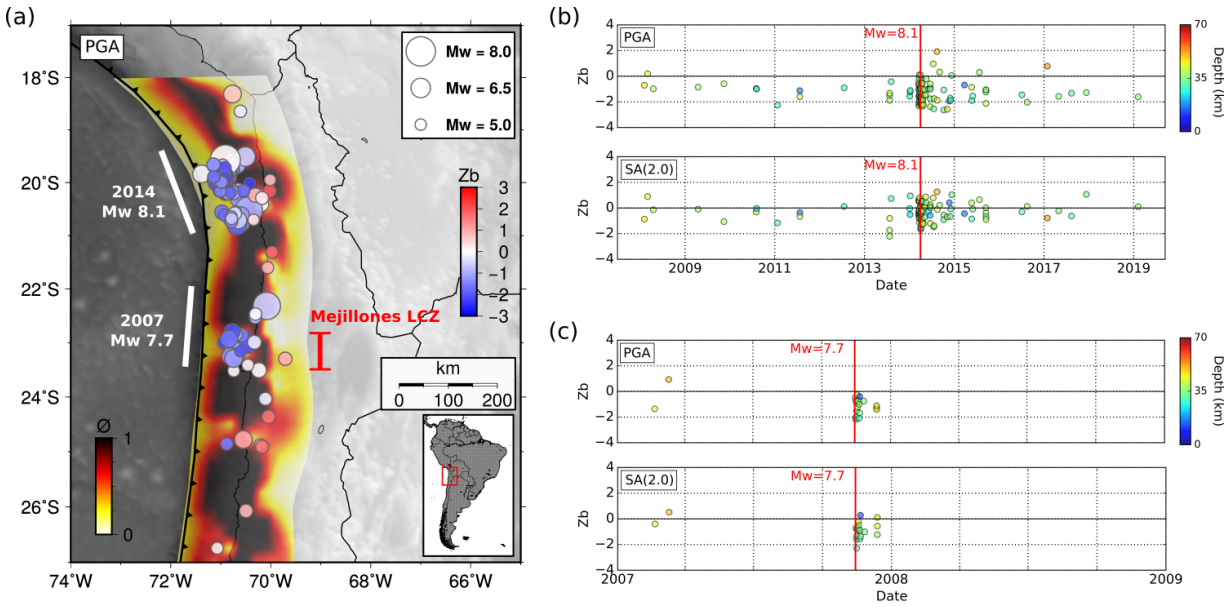

Figure 2.5: Mea17 between-event residuals in northern Chile. (a) Map showing the earthquake locations, their respective PGA between-event residuals, and the interseismic coupling model calculated by Metois et al. (2016). The approximate along-strike rupture lengths of the two major earthquakes and the trench line proposed by Bird (2003) are also shown. Temporal variations of short- and long-period between-event residuals are shown in (b) and (c) for the areas of the 2014 M_W 8.1 Iquique and 2007 M_W 7.7 Tocopilla earthquakes, respectively. LCZ, low coupling zone. The red rectangle in the small inset shows the location of the map within South America.

Temporal variations of between-event residuals were also analyzed in the areas of the 2014 M_W 8.1 Iquique and the 2007 M_W 7.7 Tocopilla earthquakes. The Iquique earthquake featured a clear slow-slip event and significant small- to moderate-magnitude seismicity several weeks before the mainshock, which occurred in a zone of intermediate seismic coupling (Ruiz et al., 2014; Schurr et al., 2014; Metois et al., 2016). From their $M_W \geq 4.0$ catalogue, Piña-Valdés et al. (2018b) found a decrease of short-period between-event residuals in this area starting in August 2013 (preseismic period), which continued for the aftershock sequence (postseismic period). Although the catalogue used in this work has fewer events due to the higher magnitude threshold ($M_W \geq 4.8$), Figure 2.5b shows that

events with negative short-period PGA between-event residuals are observed several years before the Iquique mainshock, and continued for the aftershock sequence, indicating a longer time period of events with predominantly weaker short-period radiation before and after the Iquique earthquake. This trend is less obvious for long periods (2 s), in which the residuals tend to be more aligned around zero, showing a better predictive performance of the GMM at these periods.

The Tocopilla earthquake nucleated in a region of intermediate coupling and propagated southward along the deeper coupled seismogenic zone (Béjar-Pizarro et al., 2010), stopping within the Mejillones LCZ, which is a small segment where the coupled patch narrows. Aseismic slip has been reported in the Mejillones segment, especially after the 1995 M_W 8.1 Antofagasta earthquake (Chlieh et al., 2004). As discussed in Béjar-Pizarro et al. (2010), the reported postseismic sequence of the Tocopilla earthquake included a combination of aftershocks and aseismic creep, due to the structural complexity of this area. Based on the model of Metois et al. (2016), the mainshock and aftershocks seem to occur in an area of intermediate coupling. The aftershock sequence lasted for a few months, featuring mainly negative between-event residuals at all periods particularly for shallower aftershocks (Figures 2.4c and 2.5c), indicating weaker ground motions than predicted for these events.

2.8 Central Chile

The Mea17 GMM shows the best predictive performance in central Chile (Figures 2.2b and 2.3b), likely because most of the data used to derive this model come from earthquakes that occurred in this region. Total, within-event, and between-event residuals in Figure 2.2b (right) show an overall good predictive capability of the GMM. Only between-event

residuals at short periods (PGA and 0.2 s) show a slightly larger standard deviation than the model, indicating that the GMM has slightly less capability in describing the observed source-related ground-motion variability at these frequencies. The between-event residual distribution at SA(2.0) also shows a slight shift of the mean toward negative values, indicating that more events are overpredicted by the GMM at longer periods. Unlike northern Chile, within-event residuals in central Chile do not exhibit a slight increase at 90° azimuth, with no evident azimuth dependence at any period (see Figure A.6).

Within-event residuals in Figure 2b (right) show that the Mea17 GMM fits well intensities and variabilities associated with path and site effects. The site term of the stations located in this region shows no significant bias or outliers. Also, no latitudinal dependence nor correlation with V_{S30} is observed at any period (see Figure A.8). This region has several stations with either inferred or measured V_{S30} values, and Figure A.8 shows similar site term variability for both groups of stations.

Figure 2.6 shows the distribution of between-event residuals as a function of magnitude, latitude, and depth. The Mea17 residuals do not exhibit magnitude dependence, but the positive between-event residuals at short periods (PGA and 0.2 s) are mostly contributed by the deeper moderate-magnitude earthquakes. This differentiation is not clear toward longer periods (0.5 and 2 s), similar to the results obtained in northern Chile. Figures 2.6b and 2.6c show a clear increase of short-period between-event residuals with increasing depth for earthquakes deeper than 40 km, which indicates that deeper events exhibit stronger short-period radiation than predicted by the GMM. These deeper earthquakes are mostly concentrated between latitudes 28.5°S and 32°S. This clear along-dip differentiation observed in northern and central Chile may occur because the Mea17 GMM does not include a correction for depth in its functional form, and the larger short-period radiation of deeper earthquakes is not currently accounted for in the model. Conversely, this down-dip differentiation of between-event residuals is less evident at longer periods

(0.5 and 2 s), in which residuals are mostly concentrated around zero, with some predominance of negative between-event residuals at SA(2.0).

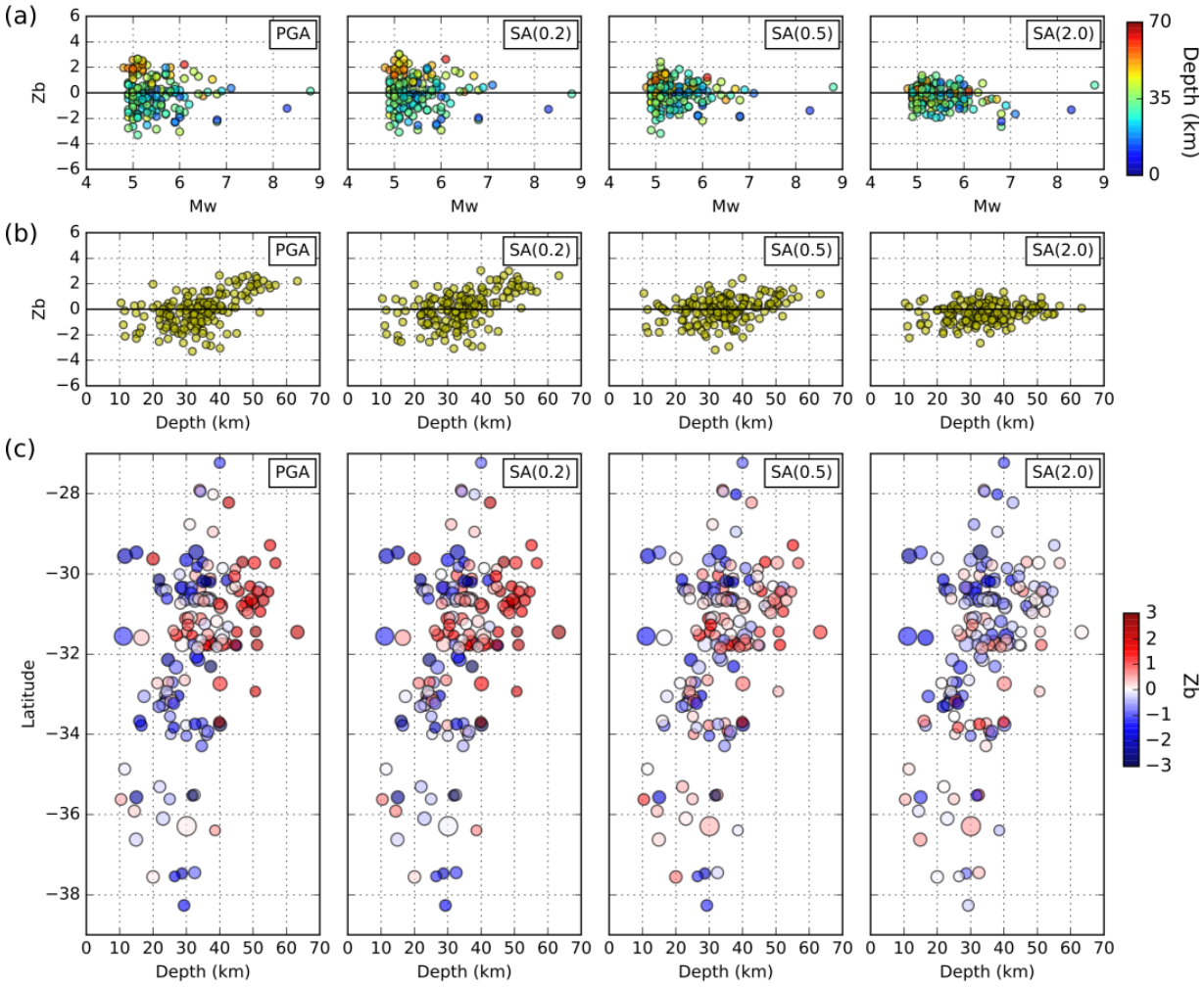

Figure 2.6: Mea17 between-event residuals in central Chile for PGA, SA(0.2), SA(0.5), and SA(2.0). (a) Residuals as a function of moment magnitude and depth; (b) residuals as a function of depth; (c) residuals as a function of latitude and depth.

When comparing the down-dip differentiation of short-period between-event residuals with the interseismic coupling model of Metois et al. (2016), the mentioned area between latitudes 28.5°S and 32°S coincides with a region where the locked patch is narrower along dip (see Figure 2.7a) compared with the adjacent sections. This narrower locked section is bounded by the Challenger fault zone in the north and by the Juan Fernández ridge in the south and includes the identified La Serena LCZ in its north section. Most of the earthquakes with stronger radiation at short periods are located on the deeper edge of this

narrower coupled zone, toward areas of low coupling.

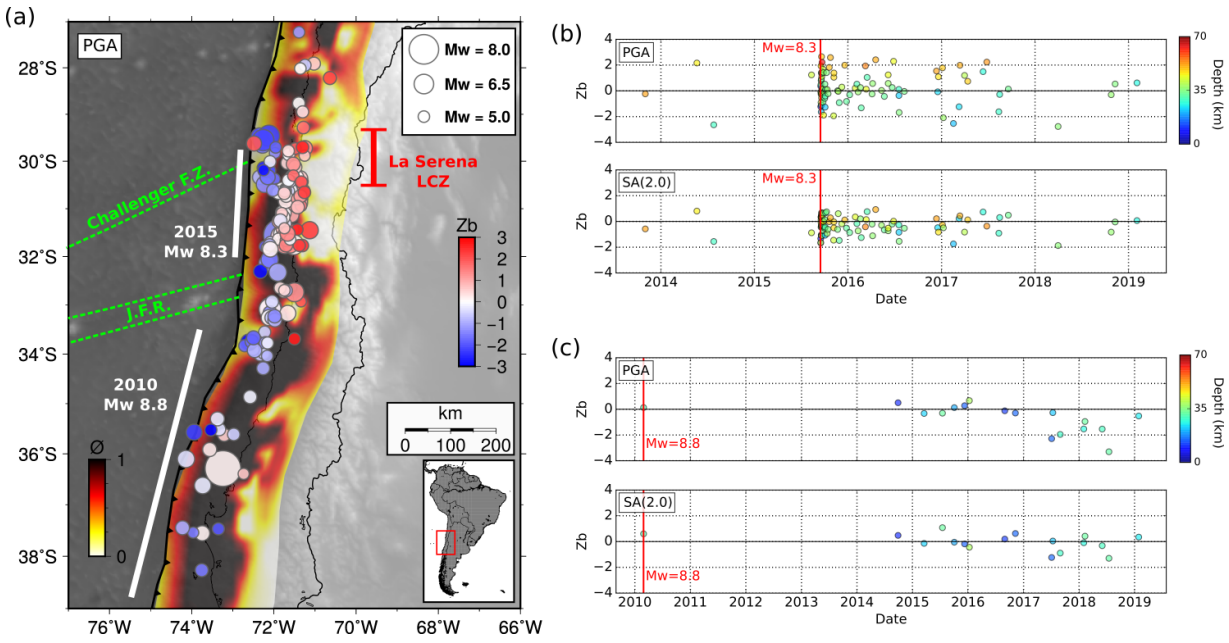

Figure 2.7: Mea17 between-event residuals in central Chile. (a) Map showing the earthquake locations, their respective PGA between-event residuals, and the interseismic coupling model calculated by Metois et al. (2016). The Challenger fault zone and the Juan Fernández ridge (J.F.R.) are also highlighted, as well as the approximate along-strike rupture lengths of the two major earthquakes and the trench line proposed by Bird (2003). Temporal variations of short- and long-period between-event residuals are shown in (b) and (c) for the areas of the 2015 M_W 8.3 Illapel and 2010 M_W 8.8 Maule earthquakes, respectively. The red rectangle in the small inset shows the location of the map within South America.

The occurrence of the 2015 M_W 8.3 Illapel earthquake within this narrower coupled section allowed a clearer observation of the along-dip differentiation of between-event residuals through the analysis of its aftershocks. Although a transient upper-plate deformation was reported in the Illapel area due to the 2010 Maule earthquake (Ruiz et al., 2016), this area did not exhibit a clear slow-slip event or significant precursory seismicity several weeks before the mainshock, as in Iquique, but it exhibited an abundant aftershock sequence, as shown in Figure 2.7b. In this case, the aftershocks do not show predominantly weaker short-period ground motions, as observed in the Iquique earthquake sequence, but rather a residual distribution centered around zero for both short periods (PGA) and long periods (2 s). Residuals are more scattered at short periods (PGA), allowing the clear identification of the along-dip residual differentiation, with deeper earthquakes contributing to positive between-event residuals and shallower earthquakes showing mostly negative

between-event residuals. Conversely, residuals are more concentrated around zero at long periods (2 s), indicating a less evident along-dip differentiation and a better intensity prediction of the GMM at these periods. Figure A.9 shows the spatial distribution of these aftershocks, where the aftershocks closer to the area of significant coseismic slip exhibit near-zero or negative PGA between-event residuals, whereas the deeper aftershocks farther away from the area of significant moment release show positive PGA between-event residuals (stronger short-period radiation), and are located in a region of lower interseismic coupling, consistent with the proposed frictional model of Lay et al. (2012).

Although it was not possible to study in detail the aftershock sequence of the 2010 M_W 8.8 Maule earthquake between latitudes 33.5°S and 39°S due to the lack of native strong-motion records in the database between 2010 and 2014, the increased data availability since 2014 allowed the study of some of the $M_W \geq 4.8$ events that occurred within the Maule rupture area. Figures 2.6c, 2.7a, and 2.7c show that the earthquakes in this area are shallower than 40 km and occurred within a wider locked zone along dip. Mostly, negative short-period between-event residuals are observed especially for events after 2017, and residuals more aligned along zero for longer periods.

2.9 Southern Chile

The worst predictive performance of the Mea17 GMM was found in the southern Chile region (Figures 2.2c and 2.3c). The mean of the total residual distribution is shifted toward negative values at all periods, indicating that the GMM overpredicts most of the ground-motion intensities in this region, which is greatly influenced by the overprediction of the source-related between-event residuals. However, it must be noted that the small population of between-event residuals due to the small number of earthquakes does not

yet provide enough sampling to draw robust conclusions under the Gaussian fit assumption. The observed standard deviations of total and within-event residuals are larger than those predicted by the GMM at all periods, showing that the GMM also does not fit well the observed ground-motion variability. For this small number of events, within-event residuals do not show significant azimuth dependence (see Figure A.6). This poor fit for southern Chile is not surprising, because no earthquakes in this region were considered for the development and calibration of the Mea17 GMM due to the infrequent seismicity and lack of stations compared with north and central Chile. However, the occurrence of the 2016 M_W 7.6 Chiloé earthquake and its aftershock sequence allowed the evaluation of some of the ground motions in this region.

The within-event residual distribution shows a larger standard deviation than that predicted by the model at all periods, as shown by Figure 2.2c (right). The site term was analyzed for the stations in this region and results are shown in Figure A.10. The seismic network in southern Chile is currently sparse and several stations were deployed recently, leading to fewer suitable stations for site term calculation. The site term values of this small station population are more scattered, showing a slightly larger standard deviation compared with north and central Chile. Finally, Figure A.10 shows no apparent correlation of the site term with latitude or V_{S30}. Although some of these site term results are similar to the results found for the rest of the country, a larger number of stations and records is required to obtain more robust results for the network in this region, which should be possible in the future, as more recorded earthquakes occur.

As discussed previously, earthquakes down to $M_W \geq 4.0$ were considered in this region due to the infrequent occurrence of moderate and large earthquakes in the last few years. For the events considered, Figure 2.8a shows a positive correlation of between-event residuals with magnitude, particularly at longer periods (0.5 and 2 s), in which the smallest events exhibit the most negative between-event residuals. This would suggest that the

Mea17 GMM is biased for smaller magnitude earthquakes (e.g., the Mea17 was developed using $M_W \geq 5.0$ earthquakes). However, Piña-Valdés et al. (2018b) did not observe such bias for their $M_W \geq 4.0$ catalogue in northern Chile. Therefore, the bias in Figure 2.8a might be an artifact generated by the lack of completeness of the considered earthquake catalogue for this region. More earthquakes need to be recorded and analyzed in this region to fully test this hypothesis.

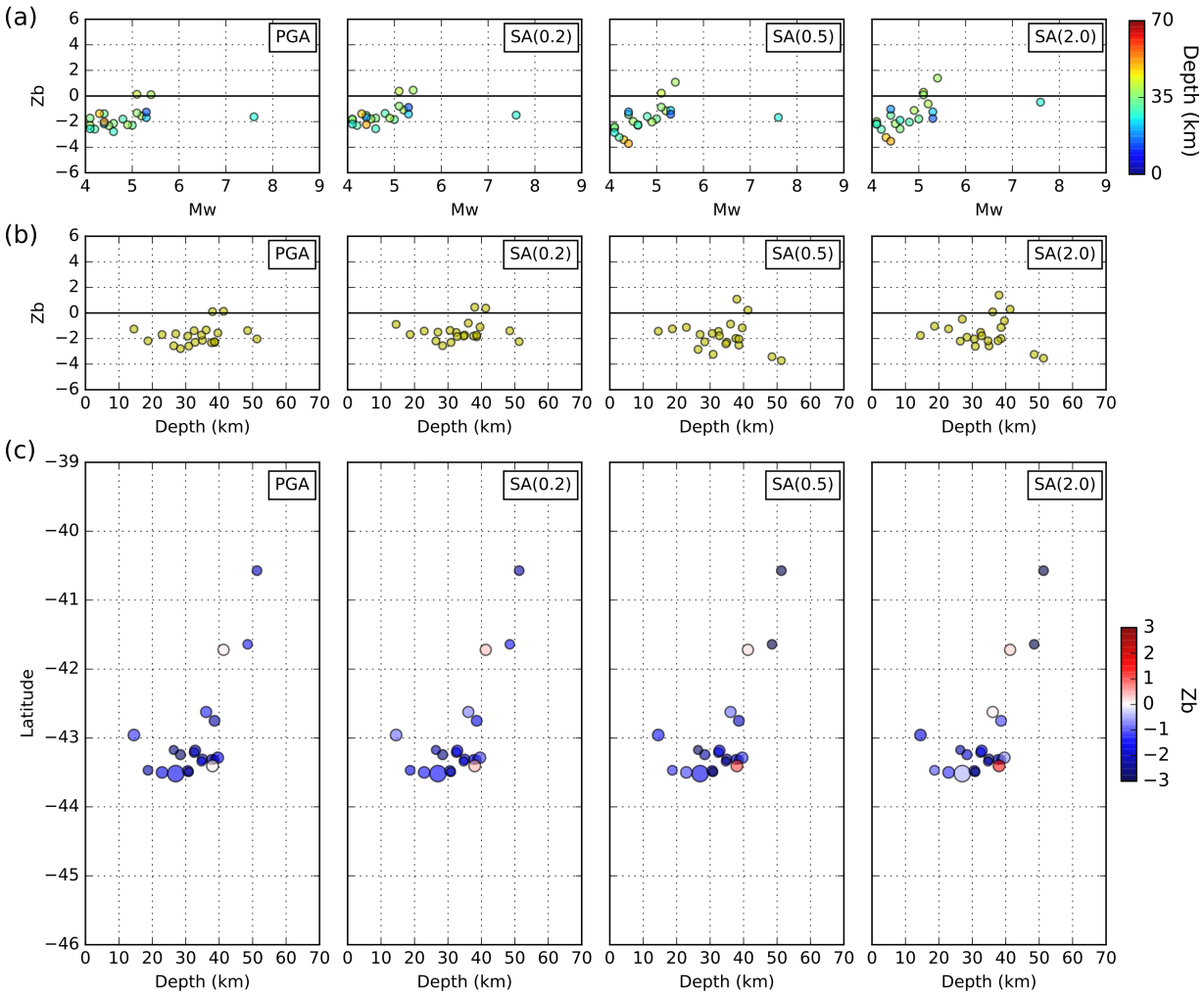

Figure 2.8: Mea17 between-event residuals in southern Chile for PGA, SA(0.2), SA(0.5), and SA(2.0). (a) Residuals as a function of moment magnitude and depth; (b) residuals as a function of depth; (c) residuals as a function of latitude and depth.

Figures 2.8b and 2.8c show that most of the earthquakes in this region are shallower than 40 km, particularly the seismic sequence of the 2016 Chiloé earthquake between latitudes 42.5°S and 44°S. Most earthquakes exhibit weaker ground motions than predicted

at all periods, and, due to their shallow locations, it was not possible to evaluate an eventual increase of short-period between-event residuals with depth, as observed in north and central Chile. The interseismic coupling model of Metois et al. (2016) does not consider this region. Therefore, the interseismic coupling model calculated by Ruiz et al. (2017) was used. Figure 9a shows this comparison. The Chiloé earthquake nucleated next to a highly locked patch, and its aftershocks occurred in the vicinity, progressing toward less locked areas. As shown in Figure 2.9b, the aftershock sequence was short, with most of the ground motions overpredicted by the GMM. This is similar to the seismic sequence of the 2007 Tocopilla earthquake (see Figure 2.5c), which may suggest some similarities in the source-related properties and frictional conditions where these two events occurred.

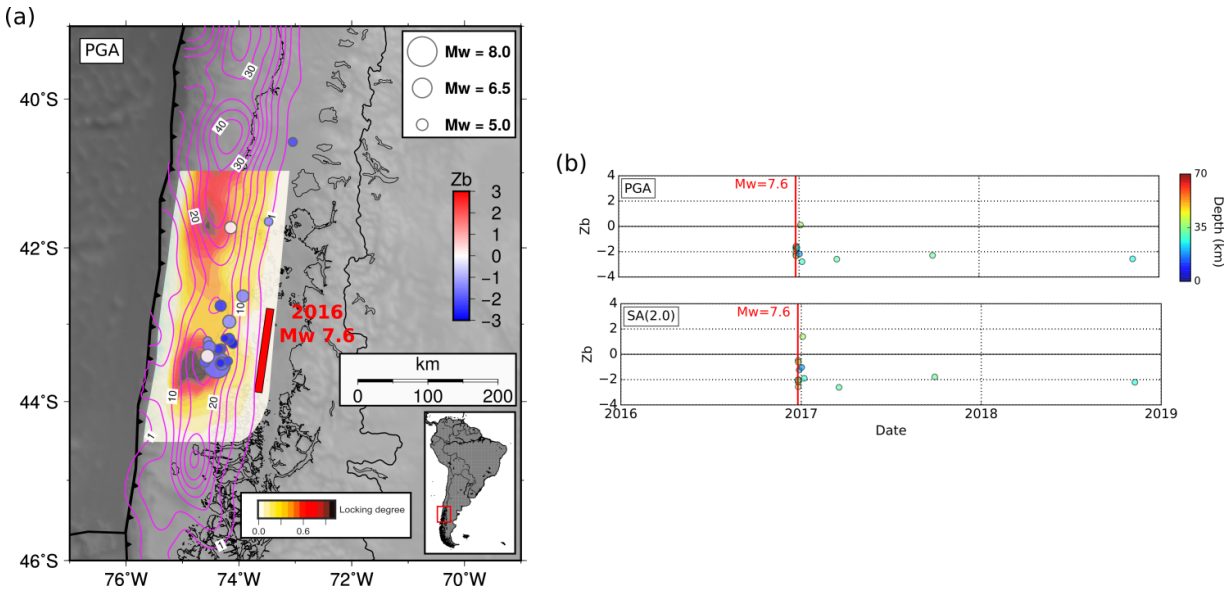

Figure 2.9: Mea17 between-event residuals in southern Chile. (a) Map showing the earthquake locations, their respective PGA between-event residuals, and the interseismic coupling model calculated by Ruiz et al. (2017). The approximate along-strike rupture length of the Chiloé earthquake is shown, as well as the contours of the coseismic slip (m) of the 1960 M_W 9.5 Valdivia earthquake (Moreno et al., 2009). The trench line is proposed by Bird (2003). (b) Temporal variations of the short- and long-period between-event residuals in the area of the 2016 M_W 7.6 Chiloé earthquake. The red rectangle in the small inset shows the location of the map within South America.

Overall, the ground-motion evaluation with this small data set in southern Chile shows an overprediction of most observations by the Mea17 GMM at all periods. As new data are becoming available over time, we propose that future GMMs for Chile should include events in this region for calibration, because after the occurrence of the 1960 M_W 9.5 Val-

divia earthquake (see Figure 2.9a), it is proposed that the 2016 Chiloé earthquake starts the gradual reawakening of moderate-to-large seismicity in the region (Ruiz et al., 2017). These newly recorded events should be included in future seismic hazard assessments.

2.10 Conclusions

Using the increasing amount of strong-motion data available along Chile in recent years, ground motions and the predictive performance of two GMMs were evaluated along the Chilean subduction zone. The Mea17 GMM was found to perform better than the Aea16 GMM in north and central Chile, where most of the data were recorded. The better fit of the Mea17 GMM to the used catalogue could be explained by the fact that the earthquakes considered in this catalogue occurred in the same region and have a similar range of magnitudes as those used for the development of Mea17. Conversely, the Aea16 GMM was developed using a global interplate earthquake catalogue with a higher magnitude threshold ($M_W \geq 6.0$). In southern Chile, both GMMs have poor predictive performance, with Mea17 being the worst, likely because no earthquakes in this region were used to develop GMMs. In addition, the catalogue considered for southern Chile has a lower magnitude threshold ($M_W \geq 4.0$) to include more events, which could negatively impact the fit to observations.

Although a higher magnitude threshold was used in this work, the obtained results of the Mea17 residual analysis are similar to those of Piña-Valdés et al. (2018b) in northern Chile, showing a slight overprediction of the GMM at short periods, mainly influenced by a bias in the between-event component at these periods, and a better intensity prediction at longer periods. The Mea17 GMM shows the best predictive performance in central Chile, performing well for ground-motion intensities and their variations at all periods.

Finally, of the two interplate models considered, this GMM shows the worst predictive performance in southern Chile, overpredicting intensities and underpredicting their variations at all periods.

By analyzing the source-related Mea17 between-event residuals, a clear along-dip segmentation at short periods (PGA and 0.2 s) was found in north and central Chile, where deeper events exhibit stronger short-period ground motions than shallower events, with a change-over depth at 40-45 km, which roughly coincides with the intersection of the continental Moho with the plate interface in these regions (Tassara and Echaurren, 2012). The deeper earthquakes with stronger short-period radiation mostly occur on the deeper edges of the locked zones, toward areas of low coupling, whereas shallower earthquakes with weaker short-period ground motions generally occur within the highly coupled segments. This suggests a frictional origin of this segmentation on the plate interface. As proposed by Lay et al. (2012), the deeper section of the plate interface is less-locked, rougher, and features smaller asperities that could generate earthquakes with stronger short-period radiation, whereas the shallower section of the plate interface is smoother, highly locked, and features large asperities that can favor larger ruptures and weaker short-period radiation. A similar relation of between-event residuals and interseismic coupling was found in steady-coupling areas in Japan (Piña-Valdés et al., 2018a). Finally, the discussed along-dip segmentation is not observed at long periods (0.5 and 2 s), in which between-event residuals tend to be aligned around zero and no clear depth dependency is observed, suggesting that long-period radiation is less affected by frictional changes on the plate interface.

Even though the frictional model proposed by Lay et al. (2012) is consistent with the spatial variations of short-period residuals in this catalogue (assuming that there are only interplate earthquakes in the database), there might be additional considerations that cannot be completely ruled out, such as the possibility that some of these deep events (50-70 km depth) with reverse mechanism might be intraplate earthquakes radiating stronger

short-period energy, or possible short-period energy dissipation due to different wave paths depending on the earthquake depth. However, such causes are beyond the scope of this study, and they should be addressed in the future.

In terms of temporal variations, the 2014 Iquique earthquake featured a clear slow-slip event and foreshock activity several weeks before the mainshock. Previous studies showed a drop in short-period radiation before the mainshock that continued for the aftershock sequence (Piña-Valdés et al., 2018b). Similar results are observed in this work, but predominantly weaker short-period radiations in the $M_W \geq 4.8$ seismicity are also observed several years before the Iquique earthquake. The 2011 Tohoku earthquake in Japan also featured a slow-slip event before the mainshock, and a drop in short-period radiation was also reported (Piña-Valdés et al., 2018a). These cases suggest that there may be additional mechanisms controlling the earthquake ground motions, in which slow-slip events and foreshocks may change frictional properties on the plate interface, degrading the fault roughness and favoring weaker short-period radiations. Conversely, the 2015 Illapel earthquake sequence did not exhibit a slow-slip event or significant precursory seismicity before the mainshock. In this case, the aftershock sequence does not show predominantly weaker short-period radiations. These aftershocks rather illuminate better the discussed along-dip segmentation of short-period ground motions, where the aftershocks with weaker short-period radiations are located in the shallower part of the plate interface, closer to the area of significant moment release of the mainshock, and the deeper aftershocks show stronger short-period radiation, located on an area of lower coupling.

In conclusion, the along-dip segmentation of between-event residuals shows that new interplate GMMs developed for Chile should include a depth correction in their functional form, accounting for the stronger short-period radiation of deeper interplate earthquakes. In addition, differences of GMM predictive performance along the different regions suggest that a regional term that accounts for this segmentation should be included in the next

GMM for Chile. Finally, because new data are becoming available in southern Chile, this region should be considered in the development of future GMMs, particularly now that significant seismicity could occur more frequently in the region after the occurrence of the 1960 Valdivia earthquake, starting with the 2016 Chiloé earthquake.

2.11 Data and Resources

Waveform data from acceleration channels of continually recording multiparametric stations were obtained from the International Federation of Digital Seismograph Networks (FDSN) using ObsPy (Beyreuther et al., 2010). Waveform data from earthquake-triggered accelerometer stations were obtained from the Centro Sismológico Nacional (CSN) EvtDB website (evtdb.csn.uchile.cl). Waveform data of the 2007 M_W 7.7 Tocopilla and 2010 M_W 8.8 Maule earthquakes were obtained from the Red de Cobertura Nacional de Acelerógrafos (RENADIC; terremotos.ing.uchile.cl), which were already corrected and processed. All websites were last accessed in June 2019. Numerical processing of waveform data was performed using ObsPy. Ground motion models (GMMs) were imported to our codes from the hazard library of the OpenQuake Engine (Pagani et al., 2014). All maps were created using Generic Mapping Tools (Wessel et al., 2013). The electronic supplement of the published article associated to this chapter includes a flat file that contains the full site, event, and observed ground-motion database of Chile used in this work.

2.12 Acknowledgements

This research was supported by the Natural Sciences and Engineering Research Council (NSERC) grants and the University of Victoria Fellowship. The authors thank Felipe

Leyton from the Centro Sismológico Nacional (CSN) for providing the raw CSN catalogue, 1-D velocity models for Chile, and tools for fast download of the EvtDB data set. The authors thank Jesús Piña-Valdés from the ISTerre and Camille Brillon from the Geological Survey of Canada for their useful help on clarifying the methods and codes. The authors finally thank Trevor Allen and another anonymous reviewer for their evaluation of this article. This is Natural Resources Canada (NRCan) Contribution Number 20190298.

Chapter 3

The crustal stress field inferred from focal mechanisms in northern Chile

3.1 Article information

3.1.1 Author and coauthor contributions

The research in this chapter was published in Geophysical Research Letters (Herrera et al., 2021). The text and figures are taken directly from that article. The author C. Herrera collected and analyzed all waveform data, and carried out the inversions of focal mechanisms, centroid moment tensors, and stress field. The author also designed and wrote the manuscript. Coauthors J. F. Cassidy, S. E. Dosso, and P. Salazar contributed with editing assistance and review of the manuscript before submission. Coauthors J. Dettmer and W. Bloch provided support with inversion and data processing codes, as well as with the review of the manuscript before submission. Coauthor C. Sippl contributed with an extended version of his earthquake catalogue for this work and with the review of the manuscript before submission.

3.1.2 Citation

Herrera, C., Cassidy, J. F., Dosso, S. E., Dettmer, J., Bloch, W., Sippl, C., and Salazar, P. (2021). The Crustal Stress Field Inferred From Focal Mechanisms in Northern Chile. *Geophysical Research Letters*, 48(8), e2021GL092889. DOI: https://doi.org/10.1029/2021GL092889

3.1.3 Author's names and affiliations

Carlos Herrera[1], John F. Cassidy[1,2], Stan E. Dosso[1], Jan Dettmer[3], Wasja Bloch[4], Christian Sippl[5], and Pablo Salazar[6,7]

[1] *School of Earth and Ocean Sciences, University of Victoria, Victoria, BC, Canada*

[2] *Pacific Geoscience Centre, Geological Survey of Canada, Natural Resources Canada, Sidney, BC, Canada*

[3] *Department of Geoscience, University of Calgary, Calgary, AB, Canada*

[4] *Deutsches GeoForschungsZentrum, Potsdam, Germany*

[5] *Institute of Geophysics, Czech Academy of Sciences, Prague, Czech Republic*

[6] *Departamento de Ciencias Geológicas, Universidad Católica del Norte, Antofagasta, Chile*

[7] *Centro de Investigación para la Gestión Integrada del Riesgo de Desastres (CIGIDEN), Santiago, Chile*

3.2 Abstract

We study the spatial variability of the crustal stress in northern Chile. A margin-parallel compressive crustal stress regime is inferred along the coastal region between 19°S and 23.5°S, similar to stress observations in Cascadia and Japan. The Andean Precordillera

shows a distinct stress field associated with a strike-slip faulting regime around 21°S. These results are constrained by over a decade of observations, for which earthquake catalogues report thousands of events in the continental crust. We present focal mechanisms for 817 of these crustal earthquakes, including mechanism qualities. The best mechanisms were grouped and inverted to infer the stress-field variability. We interpret the margin-parallel compression to be caused by the concave shape of the margin and the locking of the plate interface. The inferred strike-slip regime in the Andes agrees with previous studies and has been proposed to be mostly caused by local stresses imposed by a thicker crust.

3.3 Introduction

The subduction zone between 19°S and 24°S in northern Chile exhibits frequent occurrence of interplate, intraslab and crustal earthquakes. Most of this seismicity is related to the relatively fast convergence rate (∼63 mm/yr) of the subducting Nazca plate beneath South America in this region (Kendrick et al., 2003).

Interplate earthquakes reach the largest magnitudes, with several historical and recent large earthquakes documented (Ruiz and Madariaga, 2018). Modern seismic networks have allowed the study of the source properties and rupture mechanisms of large interplate earthquakes in northern Chile (e.g., Peyrat et al., 2010; Ruegg et al., 1996; Ruiz et al., 2014), as well as the foreshock and aftershock sequences of the 2014 Iquique earthquake (González et al., 2015; Soto et al., 2019). Source properties of large intraslab earthquakes within the Nazca plate in this region are also well studied (e.g., Herrera et al., 2017; Kausel and Campos, 1992; Peyrat et al., 2006; Ruiz and Madariaga, 2011). Additionally, the stress field inferred from interplate and intraslab earthquakes is predominantly compressional on the locked plate interface (from 20 km to about 60 km depth), and mostly

extensional within the Nazca plate (Bloch et al., 2018; Delouis et al., 1996).

In contrast, the crustal seismicity within the continental plate in northern Chile has been studied much less. Crustal earthquakes generally have smaller magnitudes, and large-magnitude events are rare. Therefore, earthquake detection and location are challenging, particularly using sparse seismic networks. Despite this, the small number of large crustal earthquakes still pose a significant seismic hazard in the region. For example, offshore crustal faults can create $M_W \geq 6.0$ earthquakes, such as the M_W 6.7 foreshock that intensified the sequence that after 16 days triggered the 2014 M_W 8.2 Iquique earthquake (e.g., González et al., 2015; Ruiz et al., 2014). Further inland, the 2001 M_W 6.3 Aroma earthquake and its M_W 5.8 aftershock ruptured on crustal strike-slip faults in the Andean Precordillera (Farías et al., 2005; Legrand et al., 2007). Additionally, a M_W 5.8 crustal earthquake struck in the Central Valley between the Coastal and Andes cordilleras on September 10, 2008 (discussed in the following sections), generating ground accelerations up to ∼0.6 g in the nearby town of Pica (as recorded by the RENADIC strong-motion network: terremotos.ing.uchile.cl).

Two recent earthquake catalogues (Bloch et al., 2014; Sippl et al., 2018) report high-precision detections and locations of interplate, intraslab, and crustal earthquakes in northern Chile. By using dense arrays of permanent and temporary seismic networks, these studies detected and located a considerable number of earthquakes that were previously unreported by the Centro Sismológico Nacional (CSN) of Chile, particularly in the continental crust. These new catalogues show an improved imaging of the seismicity distribution and enable a better analysis of crustal earthquakes and the associated stress field. This provides an opportunity to determine whether fault-slip observations at the surface (e.g., Allmendinger et al., 2005a; Victor et al., 2004) and crustal earthquakes beneath could be created by the same stress field.

In this work, the focal mechanism distribution and stress field in the continental crust of northern Chile are investigated using earthquakes from these two catalogues. High-precision locations and waveforms from dense seismic networks are used to constrain focal mechanisms for smaller events and centroid moment tensors for the largest events. This is allowed by the frequent crustal seismicity detected along the coastal region and in some parts of the Andes (Figure 3.1). The calculated focal mechanisms are grouped and inverted to infer the spatial variability of the crustal stress field at regional scale.

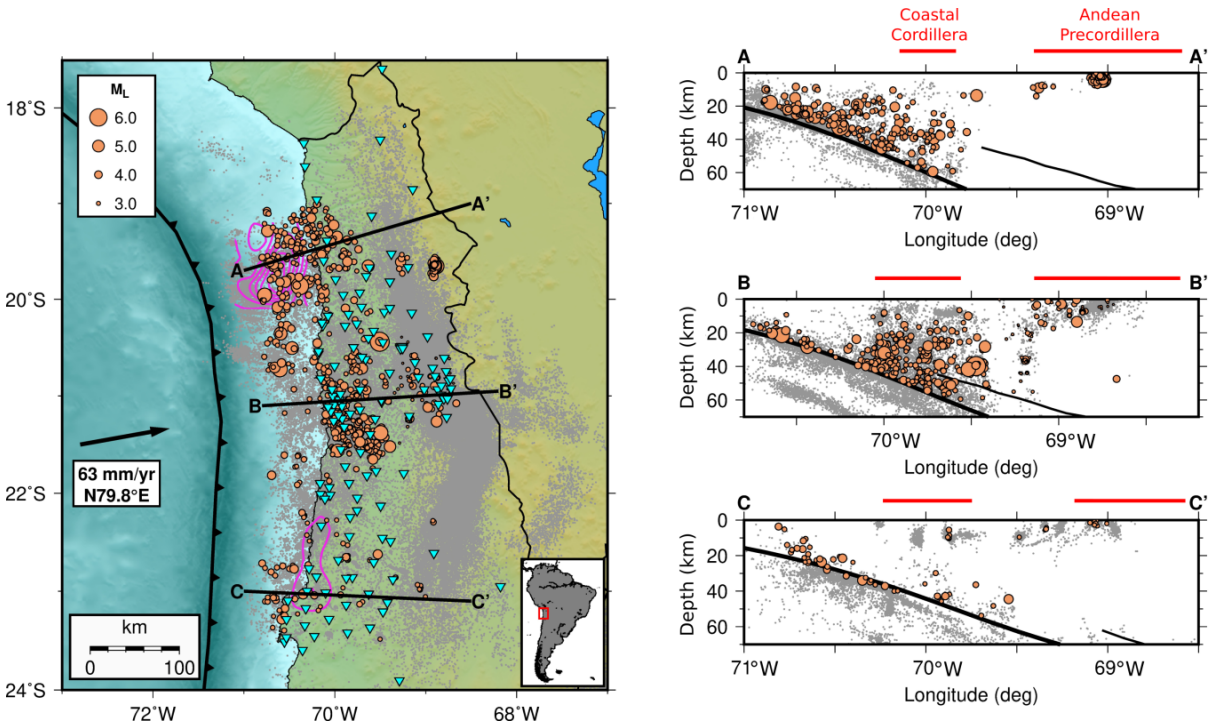

Figure 3.1: Seismicity in northern Chile reported by Bloch et al. (2014) and Sippl et al. (2018). Coseismic slip of the Tocopilla (Béjar-Pizarro et al., 2010) and Iquique (Ruiz et al., 2014) earthquakes are shown with 1 m purple contours. Seismic stations used in this study are shown with triangles. Large brown circles show the events analyzed in this work. The rest of the seismicity is shown with grey dots. Convergence vector from Kendrick et al. (2003) and trench location from Bird (2003). The inset shows the location of the map within South America. Cross sections show the plate interface (Hayes et al., 2018) and the continental Moho (Yuan et al., 2000) with thick and thin lines, respectively.

3.4 Data set

Origin times and hypocentre locations from Bloch et al. (2014) and Sippl et al. (2018) are used. The Bloch et al. (2014) catalogue (catalogue 1) contains the 2005–2012 seismicity distribution between 20°S and 21.5°S down to 120 km depth. However, no magnitudes are reported. Abundant crustal seismicity is observed onshore, particularly beneath the Coastal Cordillera and the Andean Precordillera (cross section B-B' in Figure 3.1). The Sippl et al. (2018) catalogue (catalogue 2) reports the 2007–2014 seismicity between 18°S and 25°S down to 250 km depth, with a magnitude of completeness of M_L ~2.8. Most of the crustal seismicity in catalogue 2 occurs north of 21.6°S, mostly beneath the Coastal Cordillera, consistent with catalogue 1. Catalogue 2 also reports a decrease in crustal earthquake occurrence in the coastal region south of 21.6°S (cross section C-C'). Although there are surface faults and scarp systems in the Coastal Cordillera (e.g., Allmendinger et al., 2005a), the seismicity underneath this tectonic structure seems to be pervasive, and no evident association to large faults is observed.

Stations from several permanent and temporary seismic networks have operated in northern Chile since 2005. In this work, broadband waveforms were used from the Chilean National Seismic Network (FDSN code: C), Red Sismológica Nacional (Universidad de Chile, 2012), Global Seismograph Network (ASL/USGS, 1988), IPOC Network (GFZ and CNRS-INSU, 2006), Iquique Local Network (Cesca et al., 2009), Tocopilla Project (Sobiesiak and Schurr, 2007), and Hart-Pisagua Project (Asch et al., 2014), as well as short-period waveforms from the West-Fissure and Atacama-Fault Seismic Network (Wigger et al., 2016).

First, local magnitudes (M_L) were calculated for catalogue 1 using the Hutton and Boore (1987) method (this catalogue is reported as a separate CSV file in the electronic supplement of the published article associated to this chapter), following Sippl et al. (2018). Then, earthquakes within the continental crust were selected from both catalogues con-

sidering the 3-D plate interface geometry (Hayes et al., 2018; Sippl et al., 2018) and a maximum depth of 60 km as spatial limits. The crustal subset of catalogue 1 shows a magnitude of completeness of M_L ~1.3, while the subset of slab-related earthquakes shows a higher proportion of large-magnitude events, decreasing the slope of the completeness curve (see Section B.1 in Appendix B). Finally, the crustal subsets of catalogue 1 and catalogue 2 (extended to 2017) were combined and repeated events were removed, resulting in a combined catalogue from 2005 to 2017.

3.5 Focal mechanisms and style of faulting

Region-wide, earthquakes with $M_L \geq 3.0$ were selected for focal mechanism calculations. The good coverage of the Wigger et al. (2016) seismic network in the Andean Precordillera around 21°S (cross-section B-B' in Figure 3.1) aids the study of this area. Because seismicity is less frequent in the Andes, $M_L \geq 2.0$ earthquakes were selected in that area.

For the selected events, seismograms recorded within 300 km epicentral distance were integrated and a 1 Hz high-pass filter was applied. P-wave polarities were picked from the vertical components and S/P amplitude ratios were calculated from the maximum S- and P-wave amplitudes of the three-component Cartesian sum. Azimuth and takeoff angles were calculated using ray propagation through a 1-D velocity model. Following Bloch et al. (2014), Bloch et al. (2018) and Sippl et al. (2018), we considered three velocity models for the region (Graeber and Asch, 1999; Husen et al., 1999; Oncken et al., 2003); from these, the Husen et al. (1999) model was selected for this study. Finally, polarities and amplitude ratios were inverted with HASH (Hardebeck and Shearer, 2002, 2003) to obtain the optimal double-couple focal mechanism that fits the observed radiation pattern. The stability of the solution was considered by randomly perturbing the azimuth and takeoff

angles by 5° in the inversion. Based on the solution stability (spread of the set of solutions with respect to the preferred solution), the focal mechanism quality was assigned to one of four classes ranging from A (stable solution) to D (unstable solution) (see Section B.2). This analysis resulted in a focal mechanism catalogue of 817 crustal events that have at least 5 unambiguous polarity observations, which are shown with brown circles in Figure 3.1 (this catalogue is included as CSV file in the electronic supplement of the published article associated to this chapter).

Centroid Moment Tensor (CMT) inversions were carried out for the largest earthquakes ($M_L \geq 4.5$). Regional Green's functions were calculated and stored using QSEIS (Wang, 1999) and Pyrocko-GF (Heimann et al., 2019) for the Husen et al. (1999) velocity model. The broadband velocity seismograms were inverted using the BEAT software (Vasyura-Bathke et al., 2020), which uses a nonlinear approach to estimate the full CMT. Waveforms were modelled in various frequency bands defined within the 0.02 and 0.15 Hz range. The sequential Monte Carlo method (Del Moral et al., 2006) was used to sample the parameter space (centroid location, source time function, and components of the full CMT). With this method, proper waveform modelling was achieved for seven $M_L \geq 4.5$ crustal earthquakes. The resulting CMT components, uncertainties and waveforms are shown in Section B.3. Overall, the full CMT results confirm the fault geometries and pressure (P) and tension (T) axis orientations obtained with HASH, with relatively low (∼20°) Kagan angles (Kagan, 1991) between the two methods for five of the seven events (see Section B.4). The differences on fault orientations between HASH and BEAT could be attributable to station coverage limitations affecting the HASH solution, limitations of the velocity model, or a complex rupture propagation that is better represented by a CMT solution. This could be the case for the largest event (that occurred on September 10, 2008), which exhibits the largest Kagan angle between the two methods.

Figure 3.2 summarizes the predominant faulting types and P-axis orientations of the

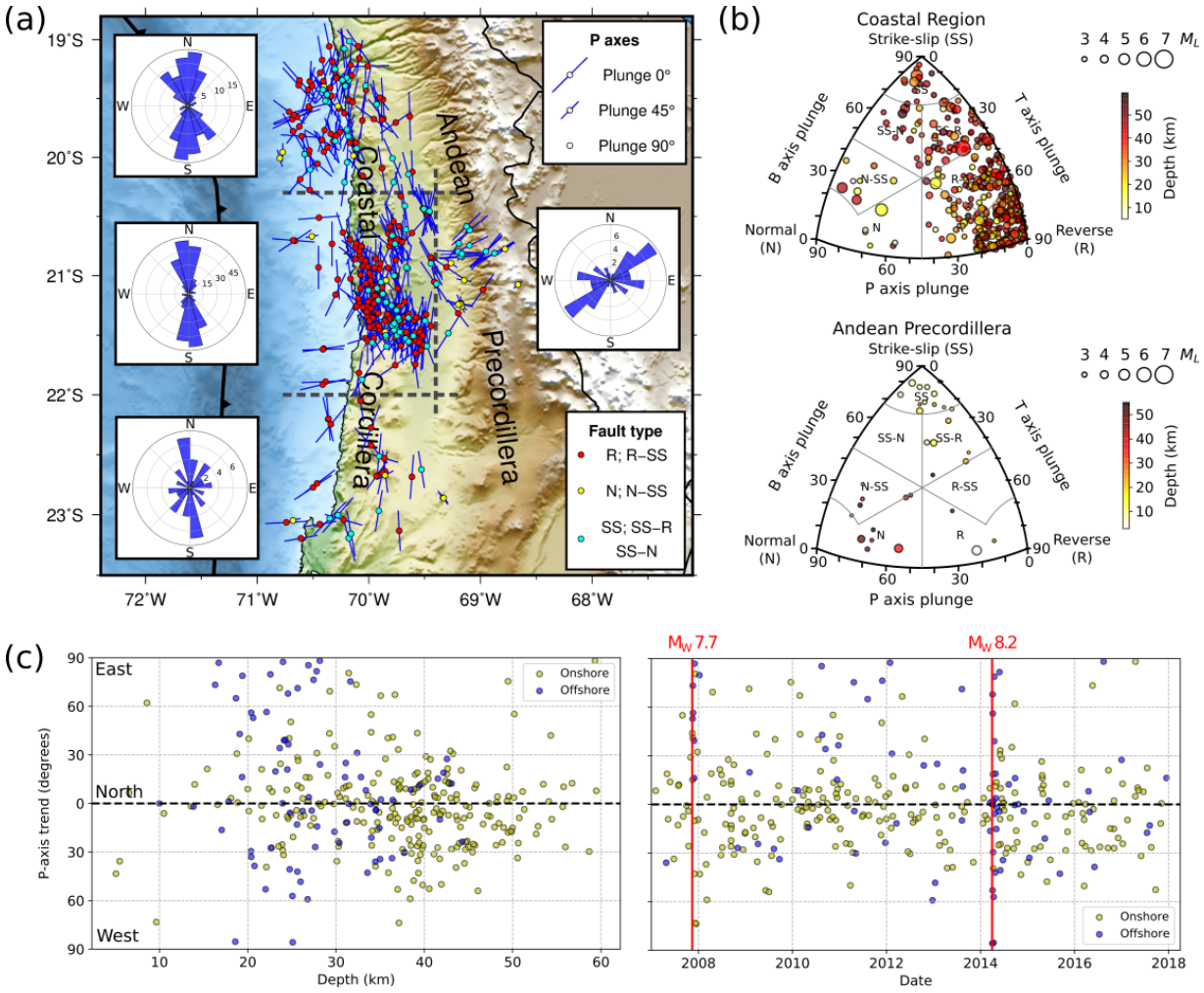

Figure 3.2: Fault characterization of crustal earthquakes. (a) Spatial distribution of fault types and P-axis orientations obtained from focal mechanisms. Rose diagrams summarize dominant P-axis trends on areas delimited by grey dashed lines. (b) Ternary plots characterizing the type of faulting in the Coastal and Andes regions. (c) P-axis trend distribution as a function of depth and time for events that occurred in the coastal region. The 2007 Tocopilla and 2014 Iquique earthquakes are highlighted with red lines.

best focal mechanism solutions. This is a subset of 355 events that only considers quality A and B mechanisms that had at least 10 unambiguous polarity observations and a stereographic station gap smaller than 180°. P-axes of offshore and onshore events along the coast show a predominantly margin-parallel orientation, especially beneath the Coastal Cordillera (Figure 3.2a). This is consistent with the mechanisms of coastal events reported by González et al. (2015). Ternary plots (Álvarez-Gómez, 2014; Kaverina et al., 1996) in Figure 3.2b show that these mechanisms in the coastal region correspond to predominantly reverse (thrust) earthquakes, which occur throughout the crust. Their orientations appear to be stationary in time over the decade of observations, particularly for the onshore events, which are not affected by the occurrence of large interplate earthquakes (Figure 3.2c). Conversely, P-axis orientations of the seismicity in the Andean Precordillera (east of 69.4°W at 21°S) show a predominantly NE-SW orientation (Figure 3.2a). The faulting style corresponds to mostly shallow strike-slip mechanisms (some of them with oblique component), and some deeper normal-faulting events (Figure 3.2b). These results suggest a different faulting style in the Andean Precordillera compared with the coastal region.

3.6 Stress field

The Bayesian method developed by Arnold and Townend (2007) was used to estimate the stress tensor by inverting the strike, dip, and rake angles of a group of focal mechanisms, including focal mechanism uncertainties. The subset of best focal mechanisms (355 events in Figure 3.2) was used as input data to estimate the crustal stress field in northern Chile. The RMS angle obtained from HASH (Section B.2) was used to define the average uncertainty of each focal mechanism. The method estimates the three stress tensor components ($S_1 > S_2 > S_3$), the stress ratio $R = (S_2 - S_3)/(S_1 - S_3)$ that describes the shape of the

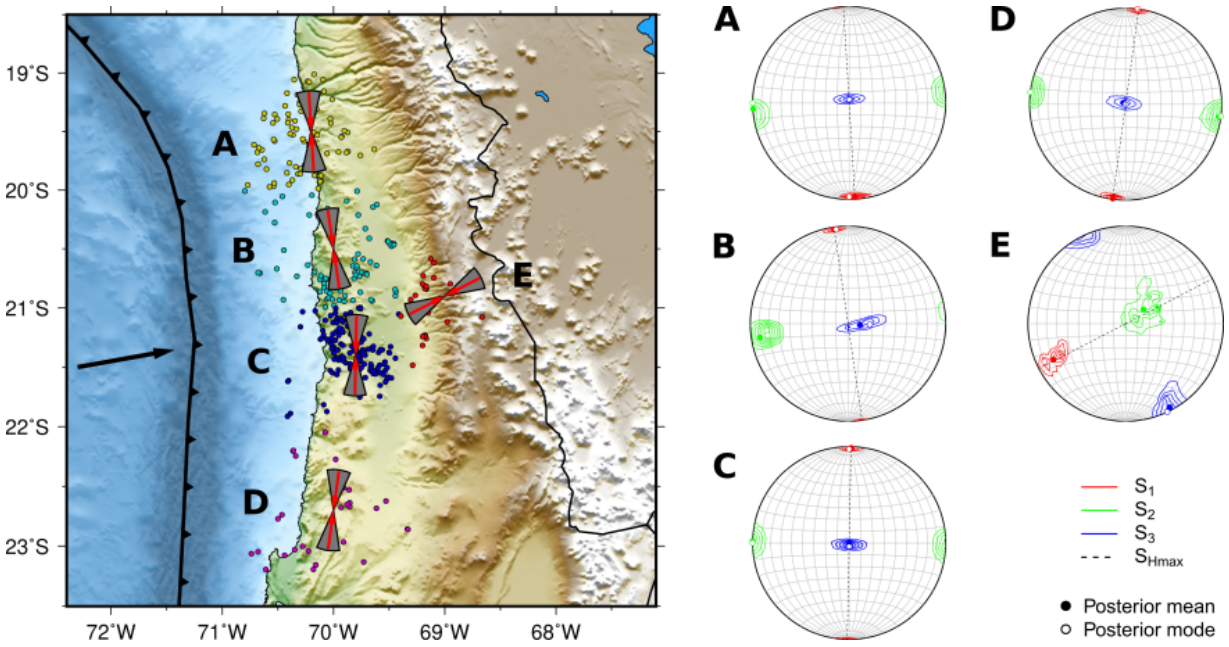

Figure 3.3: Crustal stress field in northern Chile. Red arrows on the map show the direction of S Hmax with wedges that show the 95% credibility interval of the result. Earthquakes are colored according to their group. Stereographic projections of the stress tensors are shown on the right. Contours show the posterior probability densities of the three principal stress components.

stress ellipsoid, and the maximum horizontal compressive stress direction, S_{Hmax} (Lund and Townend, 2007).

To analyze the spatial variability of the stress field, seismicity was divided into groups and a stress tensor was calculated for each group. Following Balfour et al. (2011), we assumed that the stress is constant throughout the crust thickness. Seismicity along the Coastal Cordillera was divided into groups at equal latitudinal spacing, and the seismicity in the Andean Precordillera around 21°S was defined as another group.

Stress field results are summarized in Figure 3.3 and Section B.5. Stress tensors reflect the clear trends shown by the focal mechanisms. Tensors A, B, and C were obtained from sets of 78, 75, and 141 focal mechanisms, respectively, while D and E were obtained from somewhat smaller sets of 29 and 32 focal mechanisms, respectively, due to the less frequent seismicity occurrence in those regions. Along the coast, S_1 and S_3 are almost horizontal and vertical, respectively, due to the predominance of thrust earthquakes in the

region. S_{Hmax} of the four stress tensors along the coastal region show a clear horizontal margin-parallel compression. Stress tensor E in the Andean Precordillera exhibits larger uncertainties for its components due to the smaller number of events and the more balanced occurrence of strike-slip and normal events. Nevertheless, this stress tensor shows a predominantly strike-slip regime in this area, with nearly horizontal S_1 and S_3 components, and an S_{Hmax} oriented ENE-WSW, suggesting an abrupt shift in kinematics compared with the coastal region.

3.7 Discussion

Pervasive seismicity occurs throughout the crust in the coastal region. These earthquakes have mostly reverse mechanisms with margin-parallel P-axes at all depths, indicating a margin-parallel compressional stress field in the region. These results are even clearer for the onshore events beneath the Coastal Cordillera (Figure 3.2c). This likely indicates an abrupt change of stress regime from the plate interface to the overlying crust in the coastal region.

The Coastal Cordillera in northern Chile is the remnant of a magmatic arc that was active during the Jurassic and early Cretaceous periods of the Mesozoic era (e.g., Mpodozis and Ramos, 1990), during the birth of the modern Andes. Its most important structure is the Mesozoic-Cenozoic Atacama Fault System (AFS) (e.g., Cembrano et al., 2007; González et al., 2003), extending from 21°S to 29.5°S with mostly normal and dextral strike-slip faults. Additionally, the Coastal Cordillera features several scarps between 19°S and 21.6°S striking perpendicular to the margin with reverse-fault kinematics, indicating a margin-parallel shortening (Allmendinger et al., 2005a). Geochronology analysis suggests that these scarps are more recent, having been active during the late Miocene and

Pliocene epochs (Allmendinger et al., 2005a), with some still active today (Allmendinger and González, 2010). These scarps and the crustal earthquakes occurring beneath exhibit the same fault kinematics and compression direction (Figures 3.2a and 3.4a), indicating that both may have been created by the current crustal stress field inferred in this study, which could then be long-lasting.

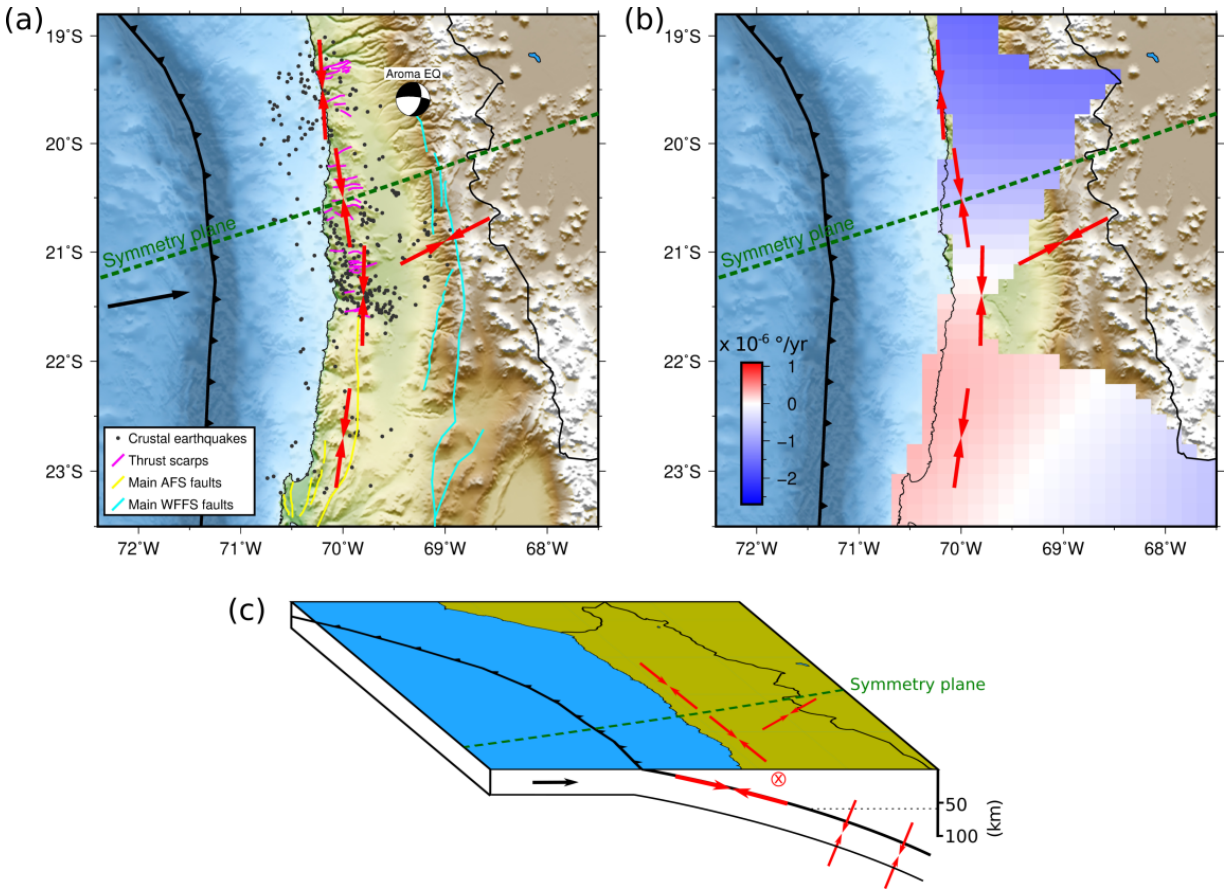

Figure 3.4: Interpretation of the crustal stress field. (a) S_{Hmax} orientations (red arrows) in a seismotectonic context. The focal mechanism shows the 2001 M_W 6.3 Aroma earthquake (Legrand et al., 2007). (b) S_{Hmax} orientations and the grid of vertical axis rotation rates (Allmendinger et al., 2007; R.W. Allmendinger pers. comm., 2021). (c) Cartoon summarizing the crustal (this study) and slab-related (Bloch et al., 2018) S_1 orientations, which are shown by the red arrows and the circled cross (representing stress into the page).

Margin-parallel compression in the continental crust has also been observed in other concave subduction regions; for example, in Cascadia (e.g., Balfour et al., 2011; Johnson et al., 2004) and in Hokkaido, Japan (e.g., Kusunoki and Kimura, 1998). Earlier work discussed how variations of plate convergence obliquity along the margin (depending on the

forearc geometry) can produce variations of margin-parallel strain; these strain rates were estimated using deflections of interplate earthquake slip vectors from plate convergence directions in several subduction zones (McCaffrey, 1992, 1996). Although results have considerable uncertainties, it was found that northern Chile was one of the few regions that exhibit margin-parallel compression (McCaffrey, 1996). Later, Bevis et al. (2001) used a concave forearc geometry with a fully locked plate interface to properly model the observed interseismic velocity field of the central Andes. This results in both a margin parallel shortening and a change in the sense of vertical axis rotation across the symmetry plane of the Andean orogen (Gephart, 1994) (Figure 3.4). This change in sign was later corroborated using GNSS and paleomagnetic data (Allmendinger et al., 2005b, 2007) (Figure 3.4b).

Therefore, the margin-parallel shortening observations along the coastal region (e.g., crustal stress field, thrust scarps) are likely caused by two simultaneous factors: (1) the concave margin geometry creating a bending of the orocline's inner arc (coastal region). The symmetry plane crosses northern Chile roughly at the centre of our study area (Figure 3.4), where bending forces would be largest. (2) High friction on the plate interface (Bevis et al., 2001; Boutelier et al., 2014), which is consistent with the large patches of intermediate and nearly full interseismic coupling observed by Metois et al. (2016) in northern Chile.

The stress field beneath the Andean Precordillera was analyzed only in a local region around 21°S (east of 69.4°W in cross-section B-B' in Figure 3.1), where good station coverage allowed the calculation of high-quality focal mechanisms in the Andes. Seismicity in this area shows a west-dipping distribution following a rheological boundary (350°C isotherm), where fluid migration may facilitate seismicity occurrence (Bloch et al., 2014; Salazar et al., 2017). Stress tensor E in Figure 3.3 shows that this area exhibits a strike-slip regime with an ENE-WSW oriented S_{Hmax} that is nearly parallel to the plate convergence direction. The observed shallow strike-slip earthquakes seem to make the largest contri-

bution to the stress tensor. Our set of best focal mechanisms for this area is smaller and less diverse than that reported by Salazar et al. (2017); nevertheless, the resulting stress tensor from the two studies is highly consistent.

The main structure in this area of the Andean Precordillera is the West Fissure Fault System (WFFS), featuring faults with diverse slip kinematics striking sub-parallel to the margin (e.g., Salazar et al., 2017; Victor et al., 2004). In particular, a strike-slip fault regime has been observed in higher altitude areas of the Andean Precordillera (Farías et al., 2005; Victor et al., 2004), near the locations of the shallow strike-slip earthquakes shown in Figure 3.2. The local vertical stresses exerted by the gravitational forces of the elevated topography have been proposed to be the cause of the strike-slip regime in the Andes (Salazar et al., 2017). These forces change the regime from reverse faulting at lower altitudes to strike-slip faulting at higher altitudes, since the increase of the vertical stress at higher altitudes would surpass the minimum horizontal stress component, resulting in a nearly vertical S_2 component. Similar spatial variations of stress orientations with topography have also been discussed for the arc-backarc region of Japan (Yoshida et al., 2015).

Although it was not possible to analyze more earthquakes over a wider area in the Andean Precordillera, there is evidence of a dextral strike-slip regime in the Andes between 19.5°S and 21°S (Farías et al., 2005). In fact, the large 2001 M_W 6.3 Aroma crustal earthquake ruptured on a dextral strike-slip fault (Farías et al., 2005; Legrand et al., 2007) in the Andean Precordillera near 19.5°S (Figure 3.4a). Its kinematics are consistent with our stress regime inferred further south.

3.8 Conclusions

A focal mechanism catalogue of crustal earthquakes and the associated crustal stress field were inferred for northern Chile. The catalogue contains focal mechanisms of 817 earthquakes. A subset of 355 earthquakes with high-quality focal mechanisms were inverted to infer the crustal stress field.

To date, this data set provides the most complete estimate and coverage of the contemporary crustal stress field in northern Chile. Crustal stress field results show different regimes for the Coastal Cordillera and the Andean Precordillera. The Coastal Cordillera region exhibits margin-parallel compression within a reverse-fault regime, which is consistent with the fault kinematics of the scarps observed in the region. This could be due to the interplay of a concave margin geometry and a coupled plate interface that extends down to 60 km depth (Figure 3.4c), creating a bending of this coastal region (inner arc of the Bolivian Orocline). Conversely, the inferred stress in the Andean Precordillera suggests a strike-slip regime around 21°S. Its S_{Hmax} direction is oriented nearly parallel to the plate convergence direction. This regime could mostly result from local stresses imposed by the thicker crust in the higher Andes. In the future, the deployment of dense seismic networks over a wider area into de Andean Orogen will allow a better determination of the spatial extent of the inferred crustal stress field.

3.9 Data and Resources

Waveform data were downloaded from the International Federation of Digital Seismograph Networks (FDSN) web services using the ObsPy toolkit (Beyreuther et al., 2010). ObsPy was also used to process the downloaded seismic data. CMTs were estimated using BEAT (Vasyura-Bathke et al., 2020) and Pyrocko (Heimann et al., 2017). Maps were created

using Generic Mapping Tools (Wessel et al., 2013).

3.10 Acknowledgements

This research was supported by the Natural Sciences and Engineering Research Council of Canada (NSERC) grants and funding from the University of Victoria. Finally, the authors thank Richard W. Allmendinger and another anonymous reviewer for their helpful feedback that improved this work. This is NRCan Contribution Number 20200715.

Chapter 4

Source parameters of the M_W 5.7 Pica crustal earthquake in northern Chile

4.1 Article information

4.1.1 Author and coauthor contributions

The research in this chapter has not been published yet at the time of writing of this dissertation. The text and figures correspond to the proposed manuscript to be submitted to a peer-review journal that fits the scope of this research. The considered journals are: Seismological Research Letters, Geophysical Journal International, Journal of Geophysical Research: Solid Earth, or Journal of South American Sciences. The author C. Herrera collected and analyzed most of the waveform data, and carried out most of the modelling and analyses. The author also designed and wrote the manuscript. Coauthors J. F. Cassidy, S. E. Dosso, and S. Ruiz contributed with editing assistance and review of the manuscript before submission. Coauthor E. Rivera carried out the S-wave spectrum analysis and inversion. Coauthors J. Dettmer and H. Vasyura-Bathke provided support with the waveform inversion software, as well as with the review of the manuscript before submission.

4.1.2 Author's names and affiliations

Carlos Herrera[1], John F. Cassidy[1,2], Stan E. Dosso[1], Jan Dettmer[3], Efraín Rivera[4], Sergio Ruiz[4], and Hannes Vasyura-Bathke[5]

[1] *School of Earth and Ocean Sciences, University of Victoria, Victoria, BC, Canada*

[2] *Pacific Geoscience Centre, Geological Survey of Canada, Natural Resources Canada, Sidney, BC, Canada*

[3] *Department of Geoscience, University of Calgary, Calgary, AB, Canada*

[4] *Departamento de Geofísica, Universidad de Chile, Santiago, Chile*

[5] *University of Potsdam, Potsdam, Germany*

4.2 Abstract

On September 10^{th}, 2008, a M_W 5.7 crustal earthquake occurred under the Central Valley of northern Chile, near the town of Pica, at a depth of ∼33 km. We find this earthquake to be a high stress-drop, reverse-oblique event that generated unusually high ground accelerations of up to ∼0.7 g. Overall, its observed ground motion intensities are considerably larger than those predicted by ground motion models, particularly at short periods. The source properties inferred through waveform modelling indicate reverse-oblique fault motion on a ∼75 km^2 plane dipping to the NE, which is corroborated by the located aftershock distribution. Stress drop values of the mainshock and larger aftershocks were estimated through S-wave spectrum modelling, with values up to ∼250 MPa for the mainshock. The event occurred in a cold section of the continental crust under the Central Valley, and its fault kinematics and orientation are consistent with the dominant style of faulting under the neighbouring Coastal Cordillera. Although our recurrence analysis shows that crustal events in the region occur at a lower rate than interplate and intraplate events, crustal events of similar or higher magnitude than the Pica earthquake have occurred, on aver-

age, approximately once every three years in northern Chile, which could pose important hazard on nearby population or critical infrastructure.

4.3 Introduction

Historic records show that the largest earthquakes in the Chilean subduction zone are usually interplate (or thrust) and intraplate events (e.g., Ruiz and Madariaga, 2018). Their frequent occurrence during recent decades allowed the development of local ground motion models (GMMs) for these two earthquake types (Idini et al., 2017; Montalva et al., 2017), and multiple detailed studies on the seismic ruptures of the largest events have been carried out. Conversely, significant earthquakes within the continental crust are infrequent and smaller in magnitude. In fact, the largest crustal events recorded in Chile have been interpreted to be linked to megathrust earthquakes: the M_W 6.9 and M_W 7.0 Pichilemu aftershocks of the 2010 M_W 8.8 Maule earthquake (Farías et al., 2011) and the M_W 6.7 precursor to the 2014 M_W 8.1 Iquique earthquake (e.g., Ruiz et al., 2014; González et al., 2015).

The dense arrays of permanent and temporary seismic stations in northern Chile have allowed detailed mapping of the crustal earthquake distribution of this region of the Chilean subduction zone (Bloch et al., 2014; Sippl et al., 2018). Northern Chile also features three important onshore crustal earthquakes recorded with modern seismic networks: the 2001 M_W 6.3 Aroma earthquake under the Andean Cordillera (Farías et al., 2005; Legrand et al., 2007), a M_W 5.7 earthquake in 2008 near the town of Pica under the Central Valley, and the 2020 M_W 6.3 Río Loa earthquake under the Coastal Cordillera (González et al., 2021).

There are reported examples worldwide of moderate ($M_W < 6.5$) onshore crustal earthquakes that generated large ground accelerations, some of damaging level, posing a significant hazard to nearby populated areas (e.g., Alvarado et al., 2009; Sigbjörnsson et al., 2009; Kaplan et al., 2010; Krishna Singh et al., 2020). The 2008 M_W 5.7 Pica earthquake is such an event. This earthquake was recorded by both broadband and strong motion stations from different local seismic networks. In particular, the closest station, located ∼21 km from the epicentre, recorded a maximum horizontal ground acceleration of nearly 0.7 g, one of the largest ever recorded by native strong motion instruments for a Chilean crustal earthquake.

To contribute to the knowledge of important crustal events in Chile, the goal of this study is to infer the source properties of the Pica earthquake and to understand its occurrence within the seismotectonic context of northern Chile. Considering its larger than expected observed ground accelerations, we first evaluate these with crustal GMMs. The source properties are inferred by modelling waveforms and S-wave spectra using different source models, as well as by locating and characterizing the earthquake's aftershock sequence. The current knowledge of the dominant style of faulting, as well as the recurrence of regional seismicity are used to discuss the characteristics of the Pica earthquake and its context.

4.4 The Pica earthquake

4.4.1 Strong motion observations

The Pica mainshock occurred on September 10^{th}, 2008, at 16:12:03 UTC in the Central Valley between the Coastal and the Andes cordilleras (Figure 4.1a) at 20.45°S, 69.49°W, and a depth of 34.2 km (Centro Sismológico Nacional, CSN). The mainshock and its after-

shocks were recorded by several local seismic stations: multiparametric stations (including broadband and strong motion sensors) from the IPOC network (GFZ and CNRS-INSU, 2006), short-period stations from the West-Fissure and Atacama-Fault network (Wigger et al., 2016), and earthquake-triggered strong motion stations from the Red de Cobertura Nacional de Acelerógrafos (RENADIC) network.

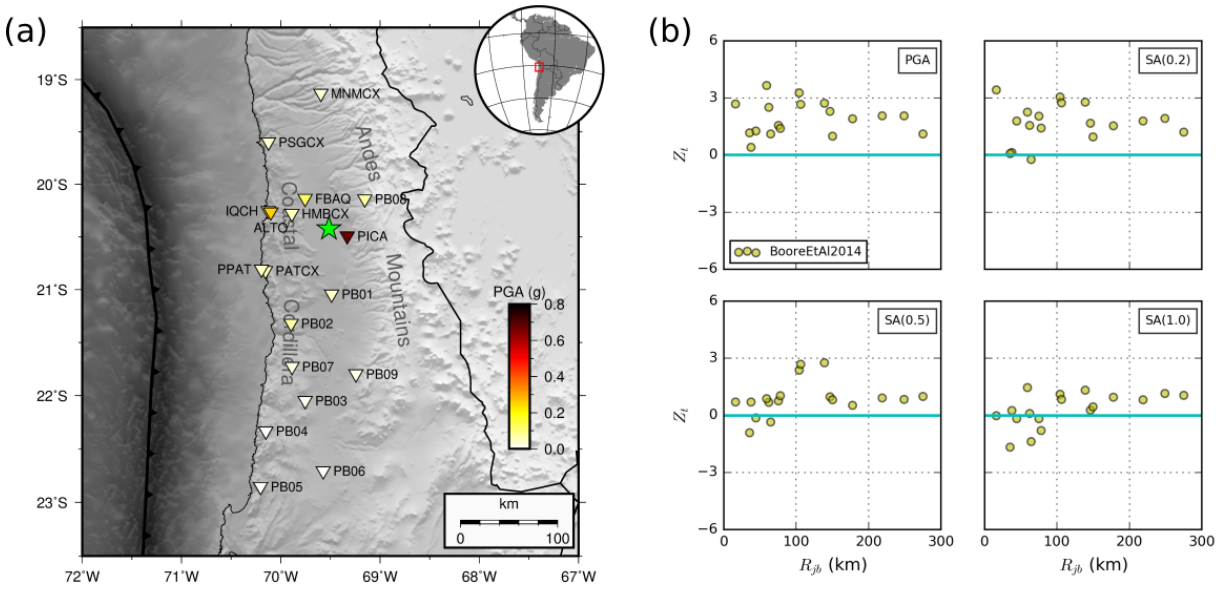

Figure 4.1: Strong motion analysis of the Pica earthquake. (a) PGA values generated by the Pica earthquake. The mainshock is shown with a green star and stations are colored based on their observed PGA. (b) Total residuals with respect to the Boore et al. (2014) GMM for PGA and SA(T) at three periods. Each sample is associated with a single station.

Ground motion intensities generated by the mainshock were analyzed in terms of Peak Ground Acceleration (PGA) and Spectral Acceleration as a function of period (SA(T)). First, strong motion waveforms were deconvolved with the instrument response and a baseline correction was applied. Then, waveforms were filtered with a fourth-order Butterworth bandpass filter between 0.1 Hz and 35 Hz, and a Hanning taper was applied at each end of the seismograms. The PGA of each station was calculated as the geometric average of the maximum accelerations recorded by the two horizontal components, while SA(T) was obtained from the geometric average of the 5% damped response spectrum (Nigam and Jennings, 1969) of the two horizontal components. These observed intensities were evaluated through residual analysis by comparing them with predictions from appro-

priate GMMs. These models were used as a reference framework to evaluate the variability of observations. Normalized total residuals $Z_t^j(T)$ were calculated for each station:

$$Z_t^j(T) = \frac{\log_e[I_{obs}^j(T)] - \log_e[I_{pred}^j(T)]}{\sigma(T)},$$

where $I_{obs}^j(T)$ and $I_{pred}^j(T)$ are the observed and predicted ground motion intensities at station j for period T, respectively, and $\sigma(T)$ is the standard deviation of the GMM for period T, usually provided in $\log_e$ units. Due to the lack of a sufficient database because of the infrequent occurrence of large (i.e., $M_W > 4.5$) crustal earthquakes in Chile, there are no local GMMs developed with Chilean crustal earthquakes at the time of this study. Therefore, the Boore et al. (2014) GMM (developed with a global database of crustal earthquakes) was selected to calculate residuals. This GMM is part of the ground motion component for "active shallow crust" regions of the Hazard Model for South America v2016 (Global Earthquake Model Foundation, GEM). To obtain the predicted intensities, this GMM requires the Joyner-Boore distance, R_{jb} (closest distance to the surface projection of the fault plane), the V_{S30} of the site (travel-time weighted average shear-wave velocity in the top 30 m), earthquake magnitude, and rake angle (which defines the fault type). Magnitude, rake, and fault size and orientation are estimated in this study through waveform modelling and aftershock distribution analysis, which are discussed in the following section. V_{S30} values were obtained from the site database compiled by Herrera et al. (2020).

As shown in Figure 4.1a, this earthquake generated large ground accelerations, with PGA up to 0.67 g at the closest station PICA (R_{jb} = 16 km). Another three stations (IQCH, ALTO, and FBAQ) registered maximum accelerations between 0.1 and 0.3 g. Observed PGA for the remaining 14 stations are all below 0.1 g. Even though ground motion attenuation with distance is clear in the overall trend of observations (Figure C.1 in Appendix C), local site amplification could also play a role in the observed intensities. Earthquake H/V ratios provide information on horizontal-to-vertical seismic amplification that could occur at specific periods at a site. In this work, these ratios are calculated by

dividing the geometric average of the response spectra of the horizontal components by the response spectrum of the vertical component. Spectra were calculated for the relevant part of the signal from $M_W \geq 5.5$ earthquakes in northern Chile. Results are summarized in Figure C.2. The four stations with the largest PGA values are part of the RENADIC network and belong to the group of stations that feature peaks of spectral amplitude, usually at periods between 0.1 and 0.5 s, where the horizontal energy is significantly amplified with respect to the vertical. This is typically an effect of shallow less-consolidated layers overlying more competent rock layers. Conversely, most of the IPOC stations do not show site amplification (flat H/V ratio) since these stations were deployed on rock sites. Even the closest IPOC station to the earthquake (HMBCX at $R_{jb} = 38$ km) shows an observed PGA of only 0.06 g, smaller than observations from some slightly farther RENADIC stations.

Figure 4.1b shows the total residuals calculated for the mainshock. The GMM underestimates the observed short-period intensities of this earthquake (PGA and SA($T = 0.2$)) for most of the stations, as shown by the mostly positive residual values at all distances. Only towards longer periods the GMM does exhibit better predictive performance, where residuals are in general closer to zero. Similar residual trends were found with the other two crustal GMMs included in the Hazard Model for South America (Akkar et al., 2014; Bindi et al., 2014) (Figure C.3), which were derived with European data. This shows that the short-period ground intensities generated by this earthquake were overall larger than those predicted by the GMMs developed with global datasets that are used for this region. The total residual can be partitioned into between-event and within-event variabilities (e.g., Atik et al., 2010). Particularly, the between-event variability describes the variations of source factors between events, such as stress drop and complex rupture kinematics that are not included in the GMM rupture parameters (magnitude, rake, depth, etc.). Following the formulation described in Herrera et al. (2020) and references therein, we calculated the between-event residuals for the Pica mainshock, which are summarized

in Table C.1 of Appendix C for each period. It is observed that the PGA residuals are the largest, and decrease towards longer periods, following the observed trend of total residuals. In the following sections, we estimate the rupture properties of this earthquake to investigate possible relations to these large observed residuals at short periods.

4.4.2 Source properties of the mainshock and aftershocks

We located the hypocentre of the mainshock at 20.4228°S, 69.5147°W and at 33.3 km depth using the NonLinLoc software (Lomax et al., 2000), which could be considered within mid to lower crustal depths. This result is very similar to the hypocentre reported by the CSN. The hypocentre location was carried out in this study by picking P- and S-wave arrivals from available broadband and short-period stations (see Figure C.4) using the Husen et al. (1999) 1-D layered velocity model.

Velocity waveforms from broadband channels were used to estimate the full Centroid Moment Tensor (CMT) of the Pica mainshock. To simulate the source-receiver wave propagation, regional Green's functions (GFs) were computed and stored using QSEIS (Wang, 1999) and Pyrocko-GF (Heimann et al., 2019) based on the Husen et al. (1999) model. Then, the low-frequency velocity waveforms (filtered between 0.02 and 0.1 Hz) were inverted to estimate the parameters of the CMT source model using the BEAT software (Vasyura-Bathke et al., 2020). Prior uniform distributions within defined bounds were set for the model parameters and the sequential Monte Carlo method (Del Moral et al., 2006) was used to sample the parameter space. Station corrections were allowed in the inversion to optimize for time shifts.

Parameter estimations are given as posterior probability densities (PPDs) around maximum a-posteriori (MAP) values that are associated to the best fit solution. Inversion

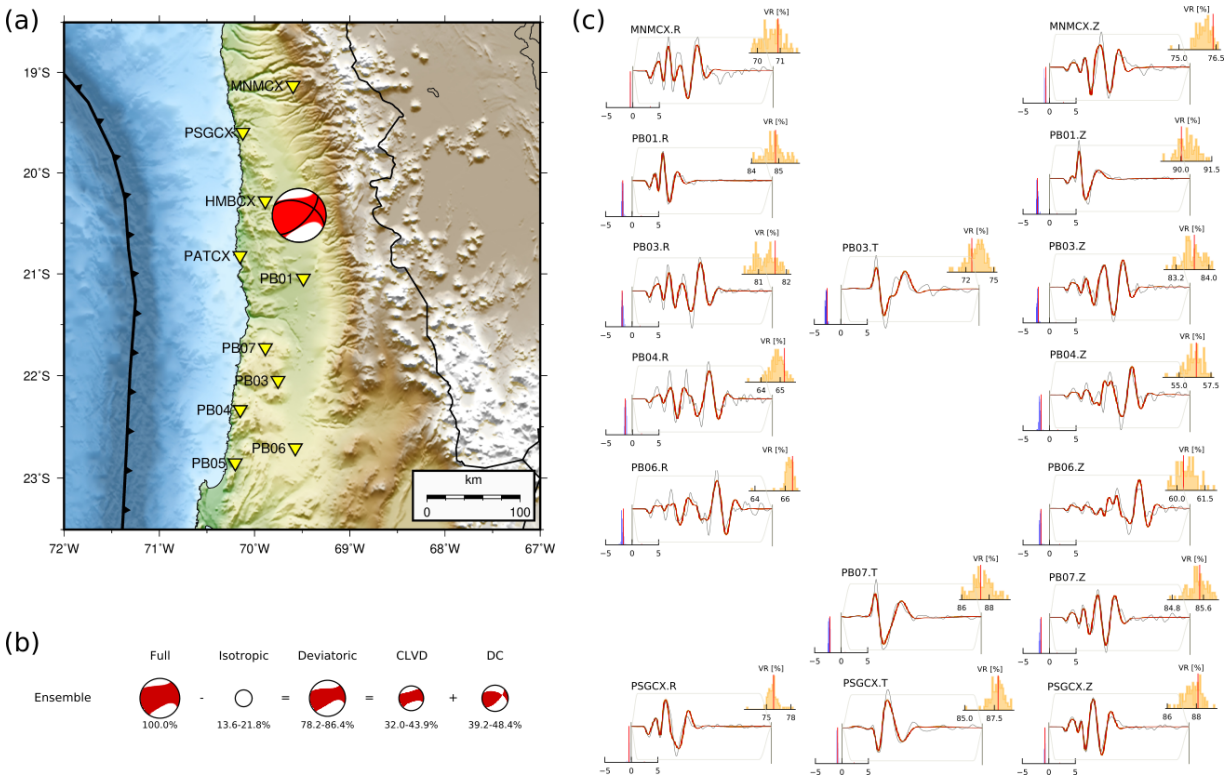

Figure 4.2: CMT solution of the Pica mainshock calculated using local stations. (a) Map showing the stations used for waveform inversion. The mainshock is shown by the fuzzy red CMT, which was obtained from an ensemble of 100 CMT solutions drawn from the PPD. Nodal planes of the MAP CMT solution are plotted on top. (b) Observed (grey) and synthetic (red) seismograms of the stations with at least two modelled channels. The shading around the red seismograms is composed of 100 random synthetic seismograms drawn from the PPD. VR and station time shifts (s) histograms from these ensembles are also shown in each plot. (c) CMT ensemble decomposition into its components.

results estimate a rupture with a MAP seismic moment of $M_0 = 3.915 \times 10^{17}$ Nm (equivalent to M_W 5.7) within a tight 95% confidence interval from 3.85×10^{17} Nm to 4.12×10^{17} Nm (Table C.2 and Figure C.5 summarize the CMT parameter estimations). The fault geometry associated to the estimated CMT is oblique slip: reverse dip-slip with a strike-slip component (Figure 4.2a). Similar style of faulting is shown by the focal mechanisms calculated for nine of the largest aftershocks (Herrera et al., 2021), with mostly oblique-reverse and pure reverse mechanisms with nearly N-S oriented pressure axes (Figure C.6). The full CMT ensemble of the mainshock shows a similar contribution of compensated linear vector dipole (CLVD) and double-couple (DC) components of up to ∼44% and ∼48%, respectively. The isotropic component varies between a non-negligible ∼14% to ∼22% (Figure 4.2b). Theory errors (e.g., simplifications of the velocity model) usually lead to relatively large isotropic and CLVD components in the CMT parameters in order

to minimize residuals (Vasyura-Bathke et al., 2021). This solution was obtained considering channels that exhibit a variance reduction (VR) between observations and predictions of at least ∼50% (Figure 4.2c and Figure C.7), where 100% VR is a perfect waveform fit. The Global Centroid Moment Tensor (GCMT) catalogue (Dziewonski et al., 1981; Ekström et al., 2012) also reports a CMT solution for the Pica mainshock. Although the GCMT best solution is within the prior bounds defined in this study, its parameter values are closely outside the 95% confidence intervals of our resulting PPDs (see Table C.2). Both solutions are consistent in terms of fault geometry and orientation (Figure C.8), but some important differences are the slightly larger magnitude of the GCMT solution and the larger isotropic component of our CMT solution.

The extended Sippl et al. (2018) catalogue reports 49 aftershocks that occurred near the mainshock until 2017. The temporal seismicity distribution in the area shows no indication of precursory activity, but rather a mainshock with subsequent aftershocks, most of them occurring during the first two months after the mainshock (Figure C.9). We located these aftershocks following the same method and station database used for the location of the mainshock. Figure 4.3 shows the spatial distribution of aftershocks near the mainshock during the first two months. Aftershock epicentres align along the NW striking fault plane (strike=291°, dip=49°, rake=147°) of the mainshock MAP CMT solution, occurring mostly SE of the epicentre, towards the Pica station. The along-strike length of this aftershock distribution does not extend beyond ∼10 km. Cross-section A-B was defined perpendicular to this fault plane and shows that aftershocks are closely aligned with the dip of this plane, occurring updip from the hypocentre. These observations confirm that the rupture occurred on the NW striking fault plane, which dips towards the NE.

With the fault plane selected, it is possible to estimate additional rupture properties via waveform inversion. For this, a rectangular source model was used, which, among other parameters, includes the length, width, average slip, and rupture duration. Strike, dip,

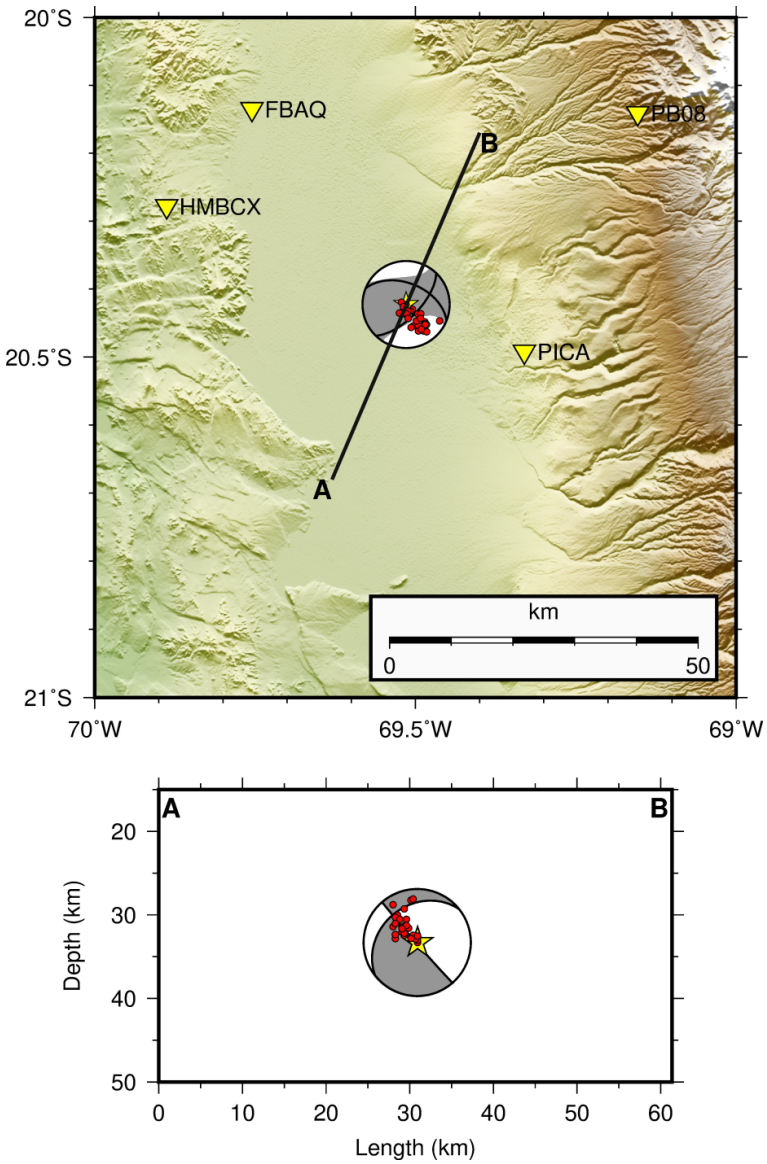

Figure 4.3: Aftershock distribution of the Pica earthquake. Hypocentres of the mainshock and aftershocks are shown with the yellow star and red dots, respectively. The MAP CMT inferred in this study and its associated nodal planes are also shown. Cross section A-B is perpendicular to the strike of the selected fault plane.

and rake angles that define the orientation of the rectangular fault are also model parameters. The strike, dip, and rake angles of the selected fault plane were used to constrain the prior distributions of these parameters. The inversion was carried out with BEAT using the same method and channels as in the CMT inversion. Results show that the rectangular source model fits the waveforms with similar VR ranges as the CMT source model (Figure C.10). Based on the 95% confidence interval obtained in the inversion, the seismic data is explained at those VR percentages by a slip on a $5.4 - 11.5$ km long

and $5.6 - 10.4$ km wide rectangular fault, with a MAP solution of 9.2 km long by 8.1 km wide. This fault size agrees with the extent of the aftershock distribution shown in Figure 4.3. Resulting PPDs of the strike, dip, and rake of this plane show well constrained high probability regions very close to the angles of the fault plane determined previously. Also, the estimated MAP average slip and duration are 0.12 m and 1.95 s, respectively (see also Table C.3 and Figure C.11 for a summary of the posteriors of these parameters). Using a shear modulus of $\mu = 4.92 \times 10^{10}$ Pa inferred from the velocity model, this rupture area and slip are equivalent to $M_0 = 4.437 \times 10^{17}$ Nm ($M_W = 5.7$), consistent with the M_0 previously estimated from the CMT model.

4.4.3 Stress drop estimation from the S-wave displacement spectrum

We computed the Fourier amplitude spectrum of the S wave for the Pica mainshock and its largest aftershocks using velocity waveforms from broadband channels of the nearby IPOC stations. First, temporal windows of variable length (depending on the earthquake magnitude) were selected, starting 1 s before the S-wave arrival, and ending where the coda attenuated to near the noise level (see example in Figure 4.4a). The available earthquake database allowed window lengths ranging from 4 s for the smallest selected aftershocks to 50 s for the mainshock. The spectrum was computed within these windows using a multitaper algorithm (Park et al., 1987; Prieto et al., 2009) to ensure that the spectrum is well estimated across most of the frequency band. The spectrum was integrated to displacement in the frequency domain, and a smoothing filter was applied to remove the abrupt oscillations in the spectrum (Konno and Ohmachi, 1998).

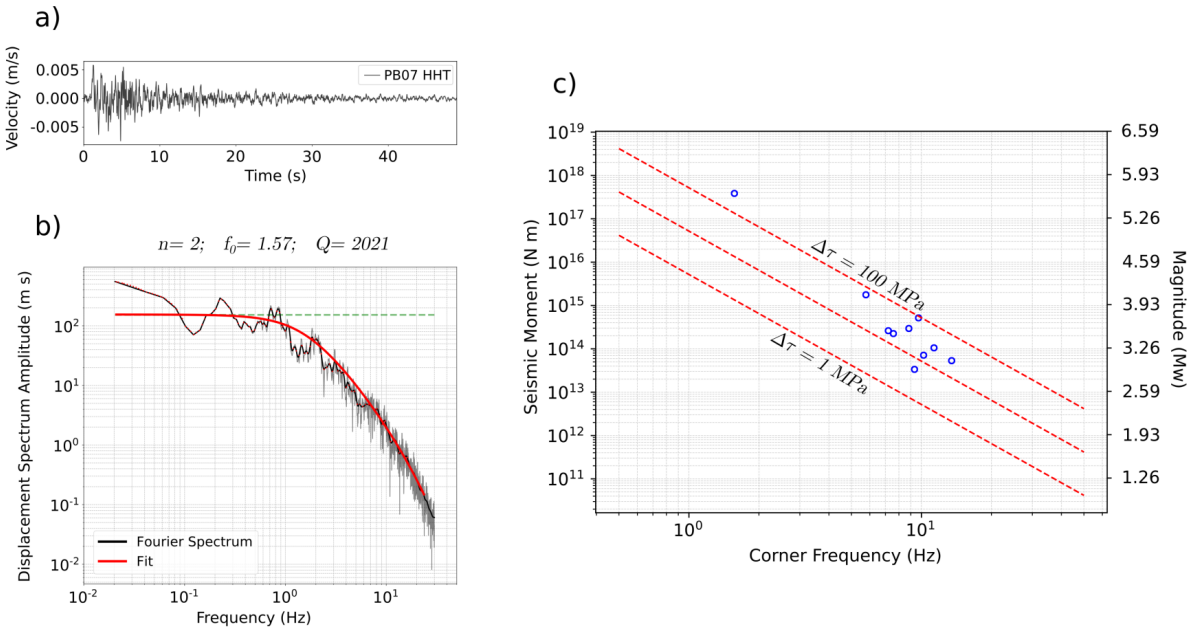

Figure 4.4: (a) S-wave window of the Pica mainshock recorded by the transverse component of station PB07. (b) Displacement spectrum of this station. Observed spectra with and without smoothing are shown in black and grey, respectively. The modelled spectrum is shown in red, and the estimated f_0 and Q values are given. The dashed green line shows the spectrum amplitude Ω_0 chosen at the low-frequency asymptote. (c) Relationship between M_0 and f_0 for a constant stress drop ($\Delta\tau$). Blue circles show the analyzed earthquakes of the Pica sequence, where the mainshock is the sample with the largest seismic moment.

We used the following amplitude spectrum model:

$$\Omega(f) = \frac{\Omega_0}{1 + \left(\frac{f}{f_0}\right)^n} \exp\left(\frac{-\pi f t}{Q}\right),$$

where the two model parameters to be estimated are the corner frequency (f_0) and the quality factor (Q) of the medium through which the waves travel and attenuate. The other values are the spectrum amplitude (Ω_0) that was picked at the low-frequency asymptote, the frequency (f), the travel time of the wave (t), and the spectrum decay parameter (n) towards higher frequencies. We set $n = 2$ in this problem, which converts $\Omega(f)$ into a f^{-2} Brune-type spectral model (Brune, 1970) with attenuation. The observed spectrum was inverted using the neighbourhood algorithm (Sambridge, 1999a,b) to infer the parameters of $\Omega(f)$, applying a clustering method that considers all earthquakes of a seismic sequence (mainshock and aftershocks) originating from approximately the same point (Ko et al., 2012). This implies two assumptions: f_0 is the same for all the stations that recorded

a specific earthquake, and wave paths from any earthquake in the seismic sequence to a particular station are all the same, from which it follows that Q must be the same. These considerations reduce the number of degrees of freedom in the inversion.

This analysis considered as many stations per earthquake as possible, particularly selecting stations for which the spectral shape provided a clear choice for f_0. This typically resulted in five to eight stations for each event. Figure 4.4b shows the modelling of the S-wave displacement spectrum of the Pica mainshock at station PB07 (results for all the stations used to model the mainshock are shown in Figure C.12). The resulting Q values are large for all the stations (see Table C.4), consistent with the fact that most of the IPOC stations are installed on rock, for which signal attenuation is low. M_0 was estimated directly from Ω_0. For the mainshock, the average M_0 from the set of spectra of the recording stations is 3.85×10^{17} Nm ($M_W = 5.65$), consistent with the results obtained by the waveform inversions using the CMT and rectangular source models.

Once f_0 and M_0 were obtained for every analyzed earthquake of the Pica seismic sequence, the Brune-type stress drop ($\Delta\tau$) was calculated following the circular source model formulation (Eshelby, 1957; Brune, 1970; Madariaga, 1976):

$$\Delta\tau = \frac{7}{16} M_0 \left(\frac{f_0}{\kappa\beta} \right)^3 ,$$

where β is the S-wave velocity and κ is a constant that comes from the average corner frequencies for a theoretical source model. In this case, following Folesky et al. (2021), we assume $\kappa = 0.28$ for the S wave.

Figure 4.4c shows $\Delta\tau$ as a function of f_0 and M_0. It is observed that the aftershocks have stress drops between 10 and 100 MPa, while the Pica mainshock has the largest stress drop: 255 MPa. The entire sequence roughly follows the f^{-3} decay defined by the dashed lines of constant $\Delta\tau$. Table C.5 summarizes the estimated M_0, f_0, and $\Delta\tau$ for all

the earthquakes considered.

4.5 Regional earthquake recurrence

To evaluate the overall recurrence of crustal earthquakes in northern Chile and compare it with interplate and intraplate earthquakes, we calculated Gutenberg-Richter relations (Gutenberg and Richter, 1944) from catalogue data during the instrumental era (since 1900). The selected study region covers most of northern Chile (Figure 4.5a). Five earthquake catalogues were used to compile the reported earthquakes within this region: the GCMT catalogue, CSN catalogue, two catalogues from the International Seismological Centre (ISC) (International Seismological Centre, 2021a,b), and the Sippl et al. (2018) catalogue extended to 2017.

To create the full catalogue of the study area, these five catalogues were merged, and repeated events were removed, prioritizing hypocentral locations reported by local catalogues or by revised global catalogues. This resulted in a full catalogue with ∼145,000 events reported between 1900 and 2017. Then, magnitude harmonization to M_W was carried out. The use of several catalogues allowed the report of multiple magnitude types for many events, where M_W, M_L, M_S, M_b, and M_d are the most common. If M_W was not available for an earthquake, other available magnitudes were converted to M_W. Conversion relations between M_W and other magnitude types were inferred using a database of earthquakes that have M_W and other magnitude types reported. General orthogonal regression was used when uncertainties were available for both variables (e.g., from events with at least three independent reports of the same magnitude type). Otherwise, classic orthogonal regression was applied. The resulting conversion relations show clear linear trends between each magnitude type and M_W (Figure C.13). Then, when M_W is not

available, the hierarchy of preferred magnitudes for conversion to M_W was set as: M_L, M_b, M_S, and M_d. Only for larger events (converted $M_W \geq 6.5$) M_S was prioritized first for conversion when available, considering the possibility of saturation of the other three magnitude scales.

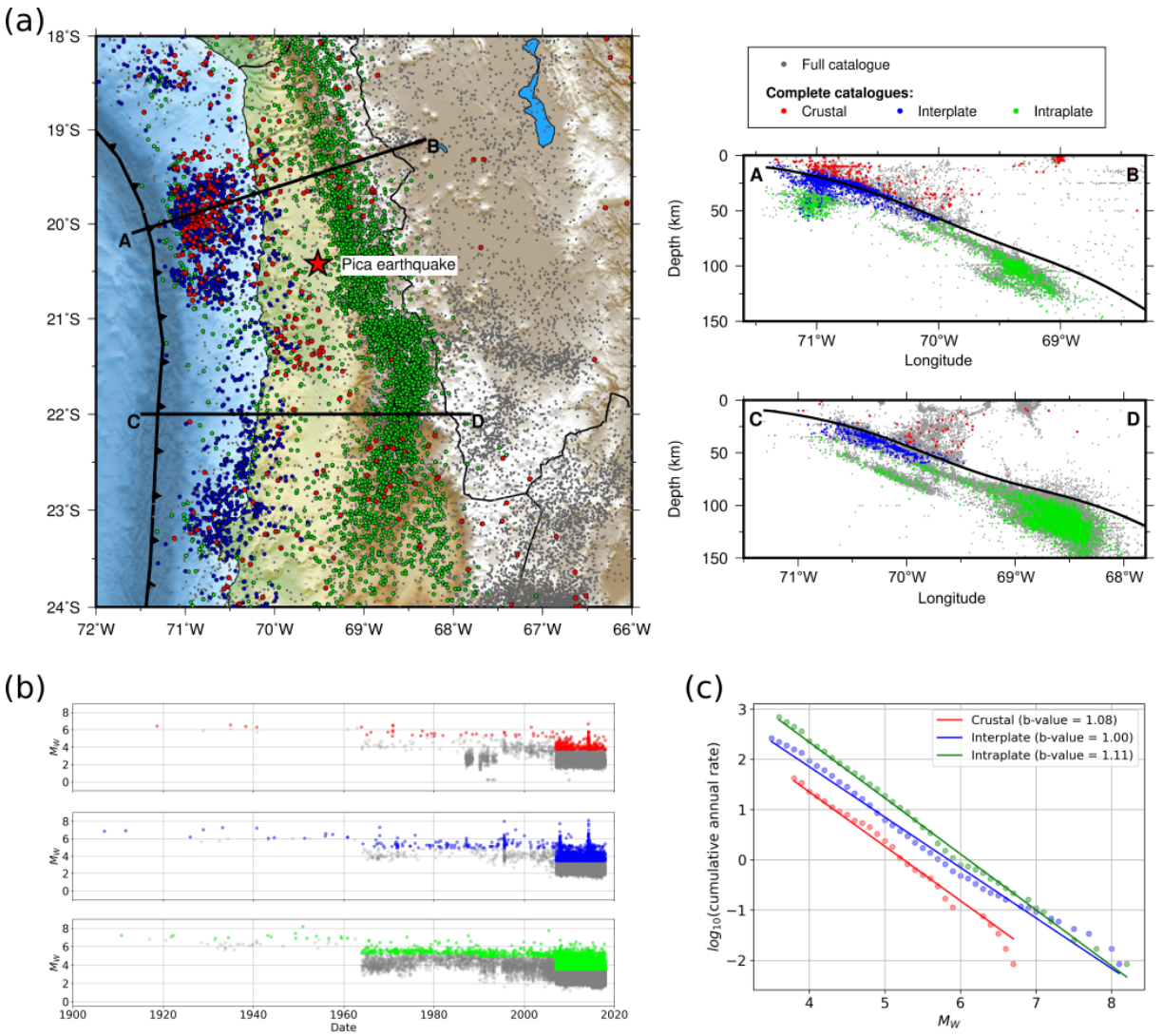

Figure 4.5: Earthquake recurrence in northern Chile. Earthquakes in the full catalogue are shown with grey dots. Crustal, interplate, and intraplate earthquakes in the complete catalogues are shown with red, blue, and green dots, respectively. (a) Earthquake distribution within the study region. The Pica earthquake is highlighted with a star. (b) Full and complete catalogues as a function of time for the crustal, interplate, and intraplate subsets. (c) Gutenberg-Richter relations and slopes (b-values) obtained from the complete catalogues of each earthquake type. The intercepts, or $\log_{10}$(a-values), are 5.68, 5.86, and 6.79 for crustal, interplate, and intraplate, respectively.

Earthquakes were separated into crustal, interplate and intraplate subsets. The selection was carried out considering earthquake locations with respect to the 3-D plate

interface geometry (Hayes et al., 2018), available CMT solutions from the GCMT catalogue, and current knowledge of the overall style of faulting. The continental Moho has significant lateral variations in depth and is not well defined near the plate interface (e.g., Yuan et al., 2000). Therefore, earthquakes within the continental crust were selected above the plate interface down to a conservative depth of 50 km. Interplate events occur mostly offshore, where depth determination with onshore networks has larger uncertainties. Considering this, interplate earthquakes were selected in two steps: first, events with thrust CMT solutions whose fault plane is closely aligned with the geometry of the plate interface; second, all other events without CMT solutions whose hypocentres are located along the plate interface. The depth limit was defined considering that the deepest thrust earthquakes have been observed down to ∼60 km depth (Bloch et al., 2018; Piña-Valdés et al., 2018b; Herrera et al., 2020). Intraplate earthquakes occur within the subducted Nazca plate, with mostly (normal) extensional faulting. In northern Chile, this regime is dominant in the second seismicity layer below interplate earthquakes and across the plate thickness at greater depths (Bloch et al., 2018). For this recurrence analysis, these intraplate earthquakes were considered within intermediate depths (not deeper than 150 km).

A completeness analysis was carried out to create complete catalogues for each earthquake type. An earthquake catalogue is defined as complete when all the earthquakes within a specified magnitude range during a specific period are reported reliably. The lower bound of this magnitude range is determined by the magnitude of completeness. Considering the variability of earthquake detection with time, time intervals were defined for various periods and the magnitude of completeness was selected as the corner magnitude from the cumulative earthquake occurrence plot for each time interval (Figure C.14). Earthquakes included in the resulting complete catalogues are colored according to their type in Figure 4.5a and 4.5b. These complete catalogues were used to calculate the Gutenberg-Richter relations for crustal, interplate, and intraplate events in northern

Chile (Figure 4.5c). The linear fits to the cumulative annual rates of earthquakes in the Gutenberg-Richter plots were calculated using the maximum likelihood algorithm proposed by Weichert (1980).

Earthquake recurrence between 1900 and 2017 shows that the three earthquake types have b-values of ∼1.0 (Figure 4.5c), which is typical in seismically active regions. However, crustal earthquakes occur less frequently than interplate and intraplate earthquakes in northern Chile, based on their lower cumulative annual rates. Intraplate events show the highest recurrence for smaller magnitudes in the region. In terms of magnitudes, the largest confirmed crustal earthquake within the observation period is the offshore M_W 6.7 precursor of the Iquique earthquake (e.g., González et al., 2015). Conversely, interplate and intraplate earthquakes reach much larger magnitudes, with the 2014 M_W 8.1 Iquique (e.g., Ruiz et al., 2014) and the 1950 M_W 8.2 Calama (Kausel and Campos, 1992) earthquakes being the largest of each type, respectively. The estimated Gutenberg-Richter relation of the crustal subset shows that $M_W \geq 5.7$ earthquakes have a cumulative annual rate of ∼0.33 events per year. This means that, statistically, approximately every three years a crustal event of similar or larger magnitude than the Pica earthquake has occurred in northern Chile. Towards larger magnitudes, the observed cumulative annual rates exhibit a sharp drop from the linear trend, particularly for $M_W > 6.4$ events. This deviation from Weichert's maximum likelihood linear fit indicates that even though those events occurred during the observation period of 118 years, their return period (estimated time between similar events) seems to be longer than predicted.

4.6 Discussion and conclusions

The Pica earthquake is an onshore event that occurred in the lower continental crust (Figure 4.6b), located at 33.3 km depth. Its M_W 5.7 magnitude was constrained by waveform modelling (using independent CMT and rectangular source models) and by S-wave spectra modelling. The fault kinematics of the mainshock and its largest aftershocks are consistent with the dominant style of faulting of crustal earthquakes under the neighbouring Coastal Cordillera, where most of the earthquakes have reverse, reverse-oblique, and strike-slip mechanisms with nearly margin-parallel (or N-S) pressure axes (Herrera et al., 2021). Additionally, the estimated rectangular model and located aftershocks indicate that the rupture occurred on a ∼9 km long and ∼8 km wide fault plane, which is striking to the NW and dipping to the NE. Similar fault kinematics and orientation were found for the sequence of the more recent 2020 M_W 6.3 Río Loa earthquake (González et al., 2021), which occurred ∼110 km to the SW of the Pica earthquake under the Coastal Cordillera (Figure 4.6a). The CMT solution of this large crustal event is similar to the Pica earthquake. It also occurred on a deep NE dipping crustal fault at ∼47 km depth, which was interpreted to be linked to the Cerro Aguirre fault in the Coastal Cordillera. Considering the system of multiple EW striking reverse scarps and active faults mapped along the Coastal Cordillera (e.g., Allmendinger et al., 2005a; González et al., 2015; Maldonado et al., 2021) (see Figure 4.6a), we propose that the Pica earthquake likely occurred on a buried branch of this fault system that extends to the Central Valley between the cordilleras, which would be under the discussed margin-parallel compressional stress regime.

Despite its moderate magnitude, the Pica earthquake generated large peak ground accelerations of up to 0.67 g, which is a damaging level of ground shaking. In general, the subset of stations near the epicentre that exhibit horizontal-to-vertical seismic amplification at their sites recorded the largest PGAs. However, the selected crustal GMMs significantly underpredict the accelerations observed at most of the stations (regardless of their site conditions), particularly at short periods (PGA and SA(0.2)). This indicates

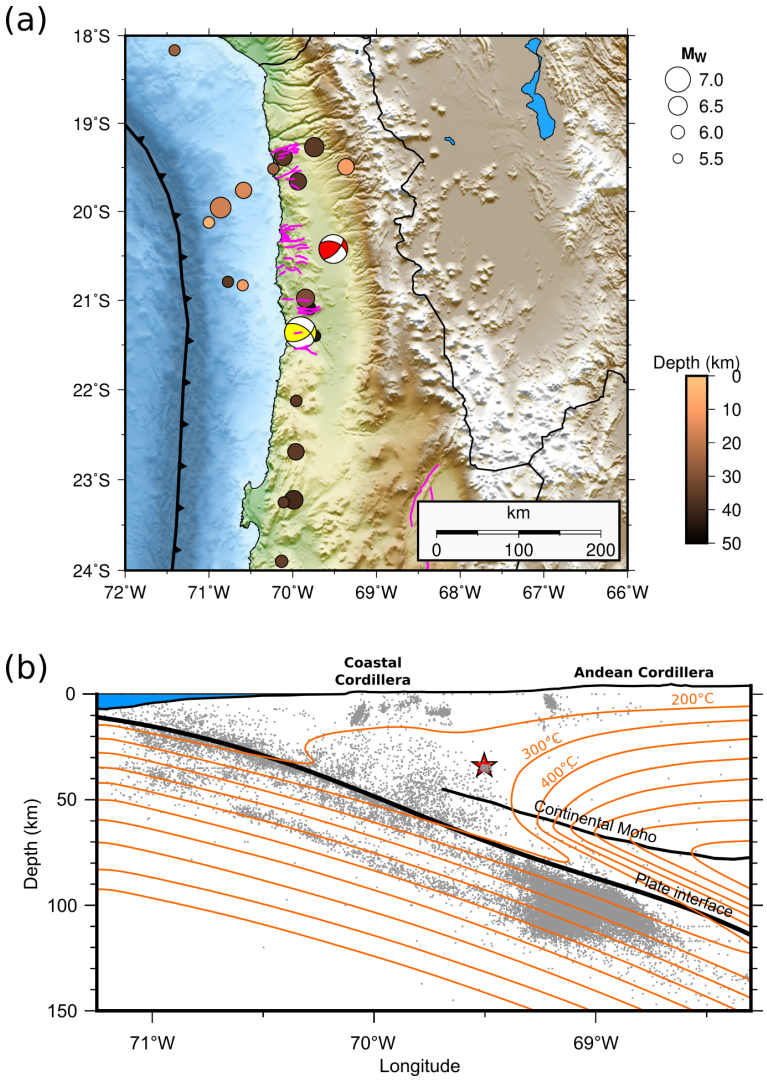

Figure 4.6: Seismotectonic context of the Pica earthquake. (a) Circles show the $M_W \geq 5.7$ earthquakes in the complete catalogue of the crustal subset. The 2008 Pica and the more recent 2020 Río Loa earthquakes are highlighted with the red and yellow focal mechanisms, respectively. Magenta lines show mapped scarps and active reverse faults. (b) Cross section perpendicular to the trench running across the Pica earthquake hypocentre. The location of the mainshock is shown with a red star. The orange isotherm contours every 100°C correspond to the thermal model from Cabrera et al. (2021). Background seismicity from the full catalogue is shown with grey dots, as well as the lines for the plate interface (Hayes et al., 2018) and continental Moho (Yuan et al., 2000).

the need for developing crustal GMMs calibrated with local data. This could be achieved once there is enough data from crustal events considered significant ($M_W \geq 5.0$) for seismic hazard and engineering applications.

The Pica mainshock has a higher stress drop than the aftershocks, consistent with the pattern observed from large earthquake databases in other active and stable regions (e.g.,

Boyd et al., 2017; Trugman and Shearer, 2018). Also, the events of the Pica sequence follow the $M_0 \propto f^{-3}$ relation with overall large stress drop values, reaching ~250 MPa for the mainshock and between 10 and 100 MPa for most of the largest aftershocks. Other active regions, such as California, feature crustal earthquakes with stress drop values within these ranges (e.g., Abercrombie, 1995; Allmann and Shearer, 2007). However, they are less common compared with the rest of the database, which is usually dominated by $\Delta\tau \leq 10$ MPa events, indicating the wide range of $\Delta\tau$ values that can be obtained with the spectrum method. In addition to local site amplifications, the high stress drop at the Pica mainshock source could also contribute to the large ground accelerations that resulted in large PGA residuals (e.g., Hanks, 1979; Oth et al., 2017; Trugman and Shearer, 2018). As observed by Trugman and Shearer (2018), there is a strong correlation between stress drop and the residual PGA, particularly for earthquakes with higher-than-expected PGA observations. Our results suggest that the Pica earthquake is another example consistent with this observed trend.

Finally, our Gutenberg-Richter results show that crustal earthquakes in northern Chile reach smaller maximum magnitudes than interplate and intraplate events, and they occurred less frequently during the last century of observations. However, crustal events of similar or larger magnitude than the Pica earthquake were determined to occur, statistically, roughly every three years. Figure 4.6 shows that the Pica earthquake occurred within a cold section of the continental crust (Cabrera et al., 2021) at the ~250°C isotherm. This brittle regime, in addition to the proposed fluid migration favoring crustal seismicity in the surroundings (Bloch et al., 2014; Salazar et al., 2017), could favor the occurrence of more earthquakes with similar characteristics to the Pica event that could pose an important hazard if they occur near population centres or critical infrastructure.

4.7 Data and resources

Waveform data from the IPOC and West-Fissure and Atacama-Fault networks were downloaded from the International Federation of Digital Seismograph Networks (FDSN) web services using the ObsPy toolkit (Beyreuther et al., 2010). Strong motion records from the RENADIC network were downloaded from their website (terremotos.ing.uchile.cl). CSN and GCMT catalogues can be accessed from their websites (www.sismologia.cl and www.globalcmt.org, respectively), while the two ISC catalogues are accessible from their DOIs in the references. GMMs were imported to our Python codes from the hazard library of the OpenQuake Engine (Pagani et al., 2014). Source parameters were estimated using BEAT (Vasyura-Bathke et al., 2020) and Pyrocko (Heimann et al., 2017). Maps were created using Generic Mapping Tools (Wessel et al., 2013).

4.8 Acknowledgements

This research was supported by the Natural Sciences and Engineering Research Council of Canada (NSERC) grants. We thank Felipe Leyton from the Centro Sismológico Nacional for providing the full CSN catalogue as a single ASCII text file, Christian Sippl from the Czech Academy of Sciences for providing the extended version of his earthquake catalogue to 2017, and Tuna Onur from Onur Seemann Consulting Inc. for helpful discussions.

Chapter 5

Conclusion

In this dissertation, observations from interplate and crustal earthquakes are used to study ground motion properties, the style of faulting, and stress field within the Chilean subduction zone. The analyses are mainly focused on quantifying the variability of earthquake observations, both in space and time, which can give clues about the degree of heterogeneities of the subduction zone. These observations provide a better understanding of subduction zone dynamics that is required to improve seismic hazard assessments.

Regarding interplate earthquakes, a full nationwide waveform and site database was compiled for Chile and used to analyze strong ground motions of 372 $M_W \geq 4.0$ earthquakes. Results show that a locally-derived GMM provides a better representation of observed ground motions in Chile. Additionally, we found that deeper interplate earthquakes generated stronger short-period radiation in northern and central Chile. The current local GMM for Chilean interplate earthquakes does not consider this observation, but future models should include this. We interpret the increase in short-period radiation as a result of an heterogeneous plate interface, following Lay et al. (2012), where small asperities in the bottom seismogenic section of the plate interface would favor the generation of higher-frequency seismic waves. Also, variations of ground motions were found in the seismic sequences of megathrust earthquakes, where the Iquique earthquake (which exhibited clear precursory activity) featured a decrease in short-period radiation in its

sequence, but the Illapel earthquake sequence did not feature that trend. We propose that these observations could be linked to a degradation of the plate interface roughness by precursory activity, favoring weaker short-period radiations. Even though we interpret our main findings to be related with frictional features on the plate interface, we do not discard the contribution of additional factors, such as energy dissipation and wave propagation through a 3-D medium. Studying such contribution would require wave simulation using 3-D models, which is beyond the scope of this dissertation, but could be developed in future projects.

Earthquakes within the continental crust were studied only in northern Chile, limited by the localized dense earthquake database acquired during the last decade. A regional focal mechanism catalogue of 817 crustal earthquakes was created, and earthquakes with the best solutions were used to infer the stress field. A clear horizontal margin-parallel compression along the coast was found, which changed to a strike-slip regime with SW-NE compression towards the Andes. This pattern is similar to the crustal stress field found in the Cascadia subduction zone. For the Chilean case, the margin-parallel compression is likely a result of the concave shape of the subduction margin, which bends the inner arc of the continent (coastal region), creating compression along the arc. This strongly correlates with the kinematics of the thrust scarp systems mapped on the surface in that region. Conversely, the stress towards the Andes is likely influenced by the thicker local topography, as suggested by previous studies. The next step (as more data become available) is to extend this study to the rest of the country, particularly to check how far this margin-parallel pattern extends to the south along the coast. In summary, this study provides a better characterization of the dominant style of faulting that can be expected for crustal earthquakes in the region. This information is highly relevant for the formulation of crustal seismogenic area sources for Probabilistic Seismic Hazard Assessments (PSHA), or other similar applications.

The largest onshore crustal event (the 2008 M_W 5.7 Pica earthquake) in the previously discussed database featured large ground accelerations of damaging level (up to ∼0.7 g), particularly near the epicentre. Observed short-period radiation intensities are clearly underestimated by current global GMMs for crustal earthquakes. We propose that the large stress drop inferred in this study is related to these large accelerations, as well as the soft site conditions in some locations that amplify the surface ground shaking at specific frequencies. Both waveform inversion and aftershock locations suggest a rupture occurring on a NW striking fault plane dipping towards the NE, consistent with the kinematics of buried crustal faults previously found under the neighbouring Coastal Cordillera, which would be under the inferred margin-parallel compressional regime. A century of catalogue records show that crustal earthquake recurrence is lower than that for interplate and intraplate earthquakes in northern Chile. Nevertheless, since this event occurred on a cold and brittle section of the crust, there is a possibility that more similar or larger earthquakes will occur in the region. The waveform data generated by these type of events should be used in the future to develop local GMMs that better account for ground accelerations of crustal earthquakes.

In summary, the earthquake observations analyzed in this work show that the Chilean subduction zone is noticeably heterogeneous, thus providing a better understanding of the seismic hazard and dynamics in the region. In the ground motion component of seismic hazard, Chapter 2 shows that current local interplate GMMs should account for depth variations of earthquake radiation and regionalization, and Chapter 4 outlines the need of developing local crustal GMMs as more data becomes available. At the same time, Chapter 3 characterizes the seismic source component of hazard in the continental crust, by providing novel information on the dominant style of faulting and how it relates with some of the fault systems in northern Chile. This information is complemented by the regional recurrence parameters for the three earthquake types reported in Chapter 4. This comprehensive evaluation of ground motions and seismicity properties can contribute to

the development of improved methods to study the seismic hazard in Chile.

Appendix A

Supplement to Chapter 2

This chapter contains supplemental results related to Chapter 2: "Ground motion evaluation of moderate and large interplate earthquakes along the Chilean subduction zone".

Table A.1: Stations whose V_{S30} values (m/s) were inferred in this study using proxy-based methods. Stations are sorted by latitude from north to south.

Station	Latitude	Longitude	V_{S30}	Station	Latitude	Longitude	V_{S30}
PB18	-17.590	-69.480	528	**A03F**	-23.453	-70.441	550
A01P	-18.219	-69.321	658	**A19F**	-23.489	-70.412	649
PX02	-18.963	-70.198	500	**A24F**	-23.610	-70.262	469
A16P	-19.160	-70.180	520	**A01F**	-23.640	-70.396	490
PX03	-20.403	-69.631	430	**A04F**	-23.667	-70.401	625
T21A	-20.945	-69.529	418	**A15F**	-23.704	-70.421	560
A21F	-21.226	-68.256	343	**PB19**	-23.905	-69.291	639
A11F	-21.425	-70.057	641	**A27F**	-24.256	-69.133	500
A07F	-21.628	-69.551	489	**A28F**	-25.107	-69.521	438
PX05	-21.940	-70.061	507	**A26F**	-25.109	-70.496	518
A14F	-22.093	-70.200	633	**A10F**	-25.411	-70.484	658
A23F	-22.337	-68.651	348	**A16C**	-26.250	-69.626	608
A06F	-22.344	-69.658	382	**A14C**	-26.342	-70.612	413
A20F	-22.454	-68.910	668	**A15C**	-26.392	-70.048	382
A18F	-22.457	-68.929	304	**A17C**	-26.753	-69.906	530
A17F	-22.460	-68.919	304	**A13C**	-28.463	-71.225	449
LVC	-22.613	-68.911	926	**A09C**	-28.575	-70.783	500
A05F	-22.891	-69.321	551	**A10C**	-28.580	-70.758	466
AF01	-22.952	-68.179	381	**A12C**	-28.594	-70.757	447
A02F	-23.101	-70.445	348	**A11C**	-28.602	-70.763	449

Station	Latitude	Longitude	V_{S30}	Station	Latitude	Longitude	V_{S30}
A22C	-28.755	-70.486	433	**M04L**	-35.282	-71.258	388
A25C	-28.955	-70.896	595	**B05I**	-36.548	-72.936	108
A23C	-28.973	-70.216	360	**B22I**	-36.690	-73.114	542
LCO	-29.011	-70.701	674	**BI05**	-36.748	-73.191	713
A24C	-29.098	-70.461	452	**B02I**	-36.783	-73.102	328
C28O	-29.291	-71.308	478	**B16I**	-36.802	-72.029	626
C15O	-29.373	-71.115	635	**B07I**	-36.816	-73.026	302
C27O	-29.384	-70.745	425	**B01I**	-36.842	-73.113	330
C06O	-29.918	-71.201	298	**B20I**	-36.911	-71.479	549
C03O	-30.037	-70.710	394	**B03I**	-36.940	-73.028	398
C14O	-30.123	-70.491	334	**B17I**	-37.038	-72.405	383
C10O	-30.234	-71.082	674	**B04I**	-37.088	-73.160	407
C18O	-30.278	-70.669	583	**B09I**	-37.329	-71.660	451
CO06	-30.674	-71.635	593	**B15I**	-37.462	-72.350	642
C05O	-30.833	-71.258	456	**B18I**	-37.470	-72.367	631
C12O	-31.398	-71.458	677	**B11I**	-38.345	-73.493	276
VICH	-31.880	-71.498	413	**L01C**	-38.773	-72.597	345
C25O	-31.944	-70.610	581	**LC02**	-38.792	-73.395	331
V05A	-32.970	-71.542	481	**GO06**	-39.584	-71.472	725
MT07	-32.976	-71.016	873	**LR03**	-39.632	-72.346	361
V23A	-33.031	-71.583	618	**LR02**	-39.806	-73.250	217
V06L	-33.037	-71.633	635	**LR05**	-40.230	-72.004	460
MT10	-33.273	-70.537	361	**L12L**	-40.581	-73.733	726
MT14	-33.396	-70.536	760	**LL04**	-40.910	-72.408	817
R08M	-33.401	-71.120	488	**LL03**	-41.138	-72.403	233
MT04	-33.405	-70.137	876	**LL06**	-42.215	-73.628	257
MT08	-33.446	-70.017	1246	**LL01**	-42.379	-72.412	884
R04M	-33.463	-70.530	329	**LL07**	-42.832	-73.478	435
R03M	-33.520	-70.612	416	**LL02**	-43.191	-71.848	998
R23M	-33.585	-70.701	382	**A08Y**	-43.896	-73.741	868
MT15	-33.599	-70.506	473	**AY01**	-44.421	-72.648	599
V24A	-33.622	-71.613	726	**A09Y**	-44.747	-72.214	1205
MT12	-33.733	-70.549	406	**A10Y**	-45.164	-73.523	297
MT13	-33.744	-70.286	765	**A02Y**	-45.396	-72.681	385
M02L	-35.000	-70.812	399	**AY02**	-46.484	-73.195	377

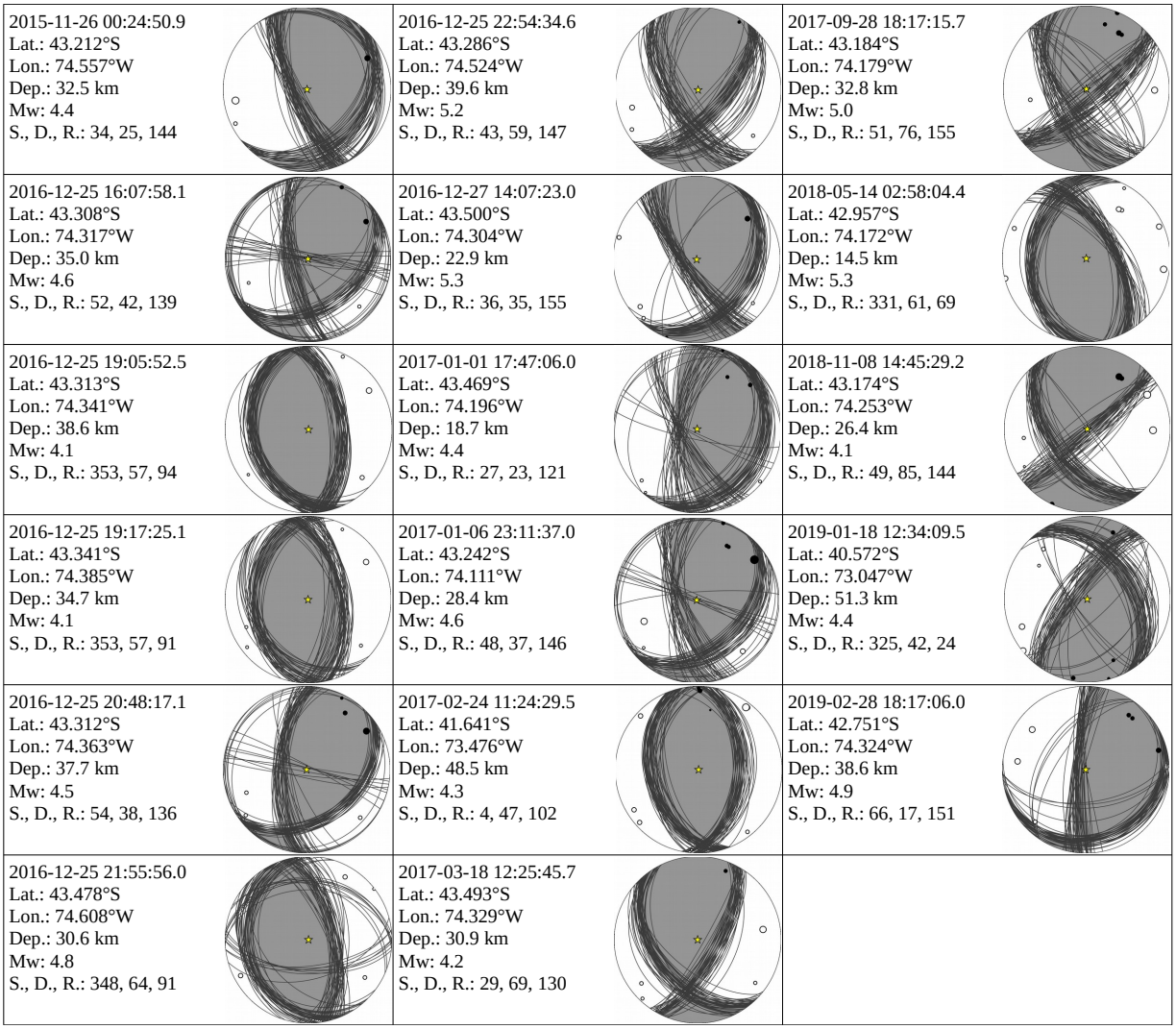

Figure A.1: Lower-hemisphere projection of the estimated focal mechanisms using HASH in southern Chile. These earthquakes were defined as interplate. The best solution is shown along with the set of solutions obtained from the angle perturbations. Station polarities are shown with black circles (positive) and white circles (negative), and their sizes are proportional to the square-root of the P/S ratio. The centre is shown with a star.

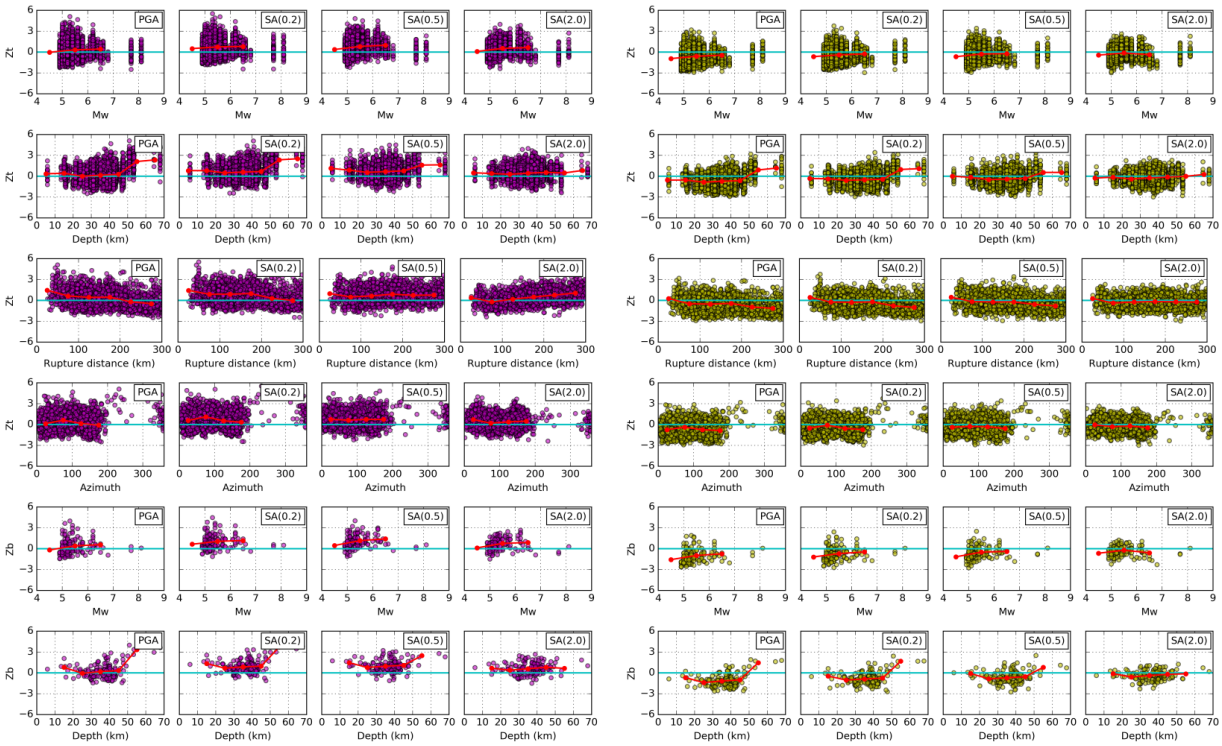

Figure A.2: Total residuals (Z_t) and between-event residuals (Z_b) as a function of different variables in northern Chile. Abrahamson et al. (2016) and Montalva et al. (2017) residuals are shown with magenta and yellow dots, respectively. The red curve shows the average residuals calculated for equal-size bins with enough residual values. Zero-residual line is highlighted in cyan.

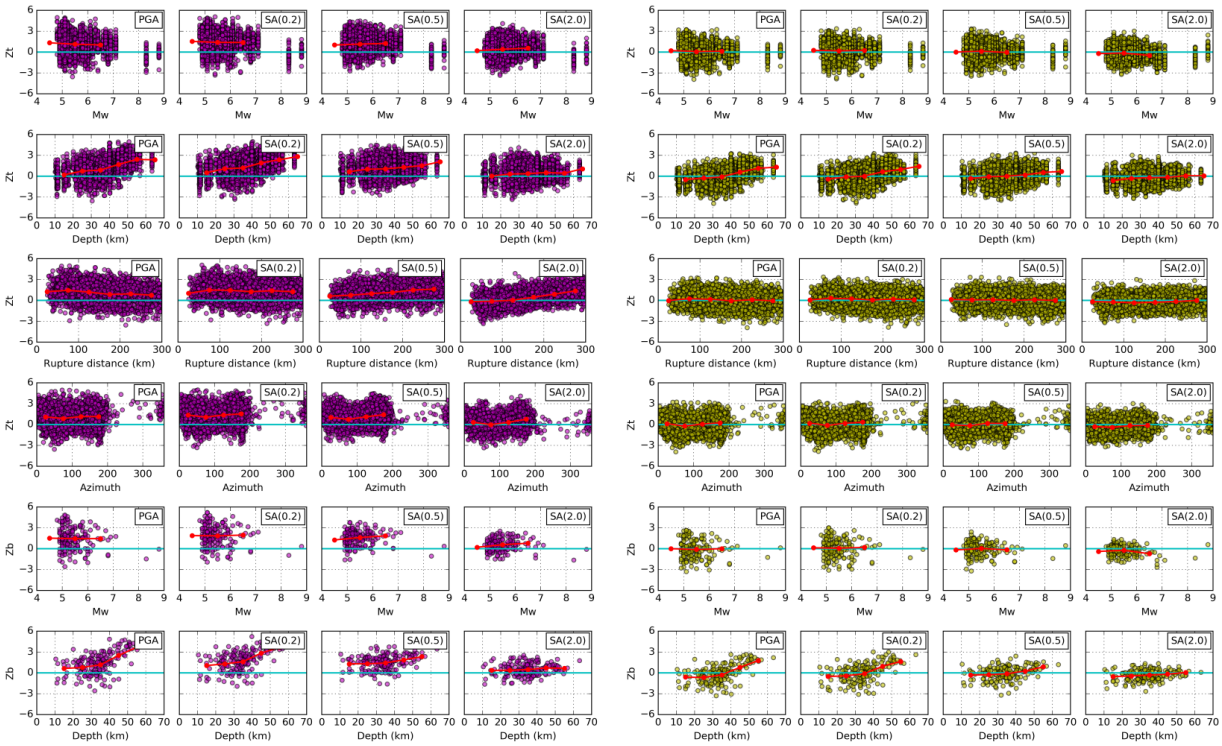

Figure A.3: Total residuals (Z_t) and between-event residuals (Z_b) as a function of different variables in central Chile. Abrahamson et al. (2016) and Montalva et al. (2017) residuals are shown with magenta and yellow dots, respectively. The red curve shows the average residuals calculated for equal-size bins with enough residual values. Zero-residual line is highlighted in cyan.

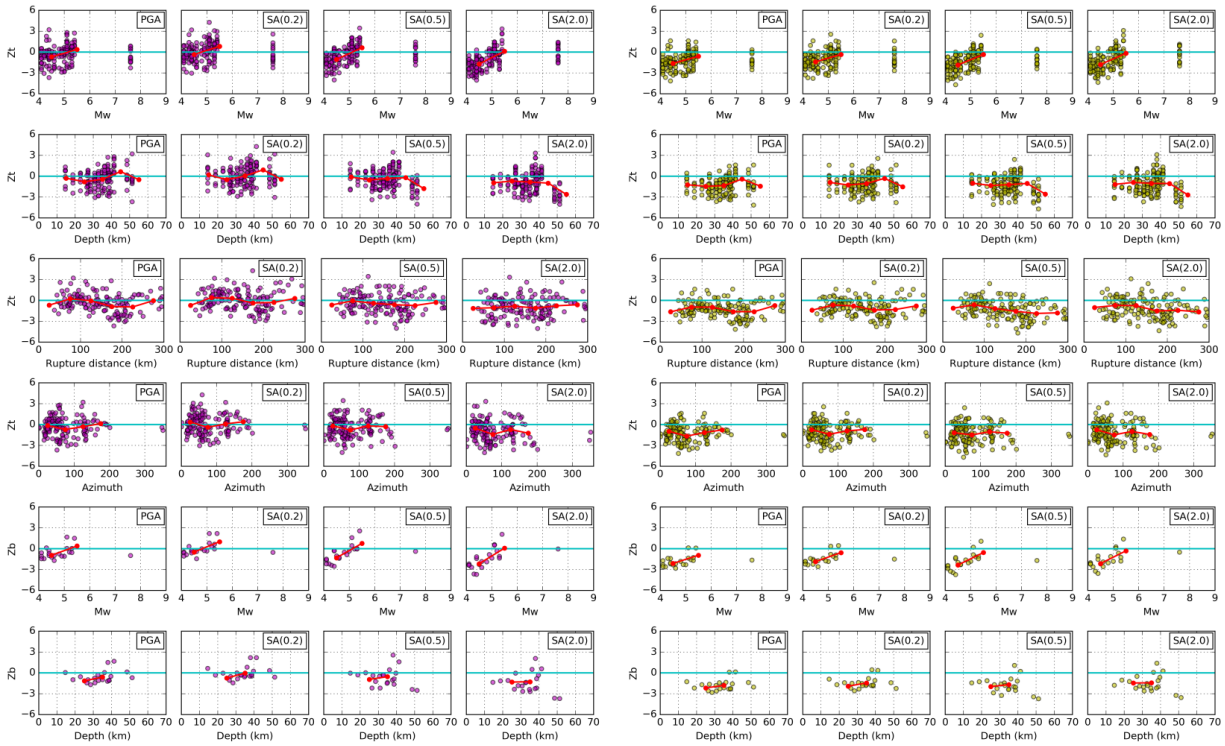

Figure A.4: Total residuals (Z_t) and between-event residuals (Z_b) as a function of different variables in southern Chile. Abrahamson et al. (2016) and Montalva et al. (2017) residuals are shown with magenta and yellow dots, respectively. The red curve shows the average residuals calculated for equal-size bins with enough residual values. Zero-residual line is highlighted in cyan.

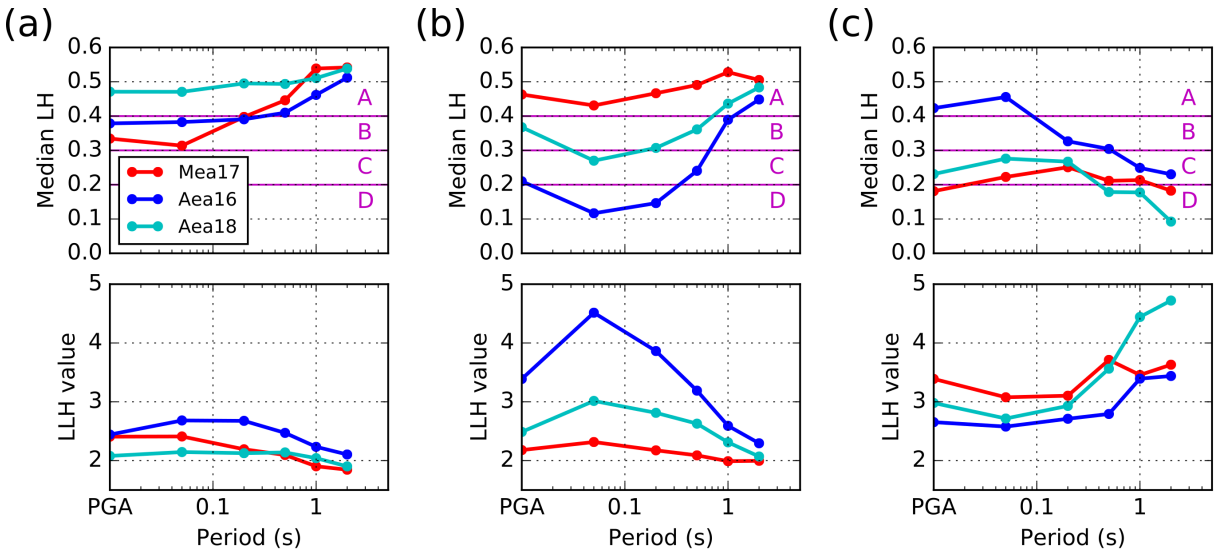

Figure A.5: Goodness of fit calculated from total residuals at different periods. Besides the Mea17 and Aea16 GMMs, the Abrahamson et al. (2018) (Aea18) GMM is also shown. Columns (a), (b) and (c) show the evaluation for northern, central and southern Chile, respectively.

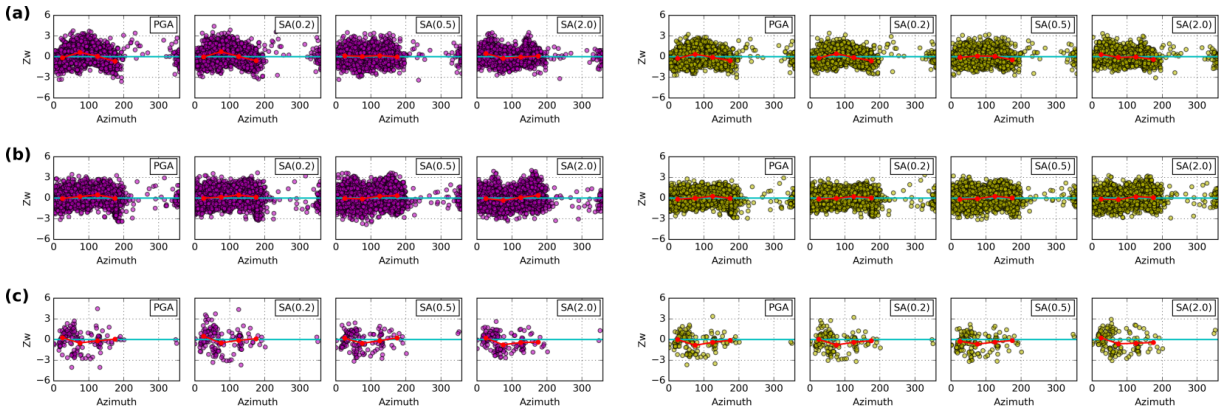

Figure A.6: Within-event residuals as a function of azimuth. Rows (a), (b) and (c) show results for northern, central and southern Chile, respectively. Abrahamson et al. (2016) and Montalva et al. (2017) residuals are shown with magenta and yellow dots, respectively. The red curve shows the average residuals calculated for equal-size bins with enough residuals. Zero-residual line is highlighted in cyan.

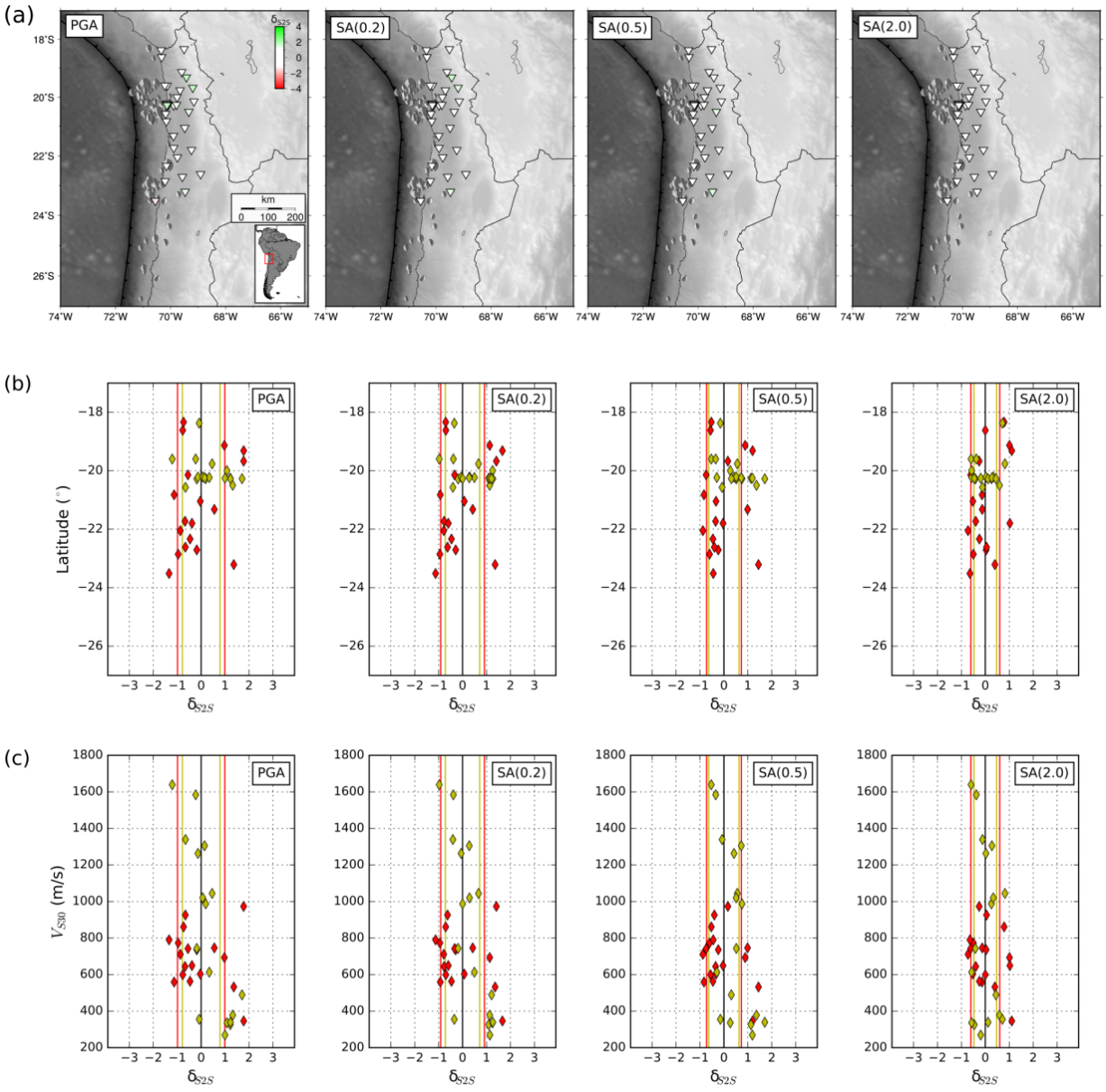

Figure A.7: Site term analysis in northern Chile for PGA, SA(0.2), SA(0.5) and SA(2.0). (a) Maps showing the seismic stations analyzed, colored based on their site term values. Focal mechanisms of interplate earthquakes are shown in grey. (b) Latitudinal variation of the site term. (c) Site term variation with V_{S30}. Red symbols in rows (b) and (c) correspond to stations with inferred VS30, and yellow symbols correspond to stations with measured V_{S30} by Leyton et al. (2018). Red and yellow lines correspond to the site term standard deviations of stations with inferred and measured V_{S30}, respectively.

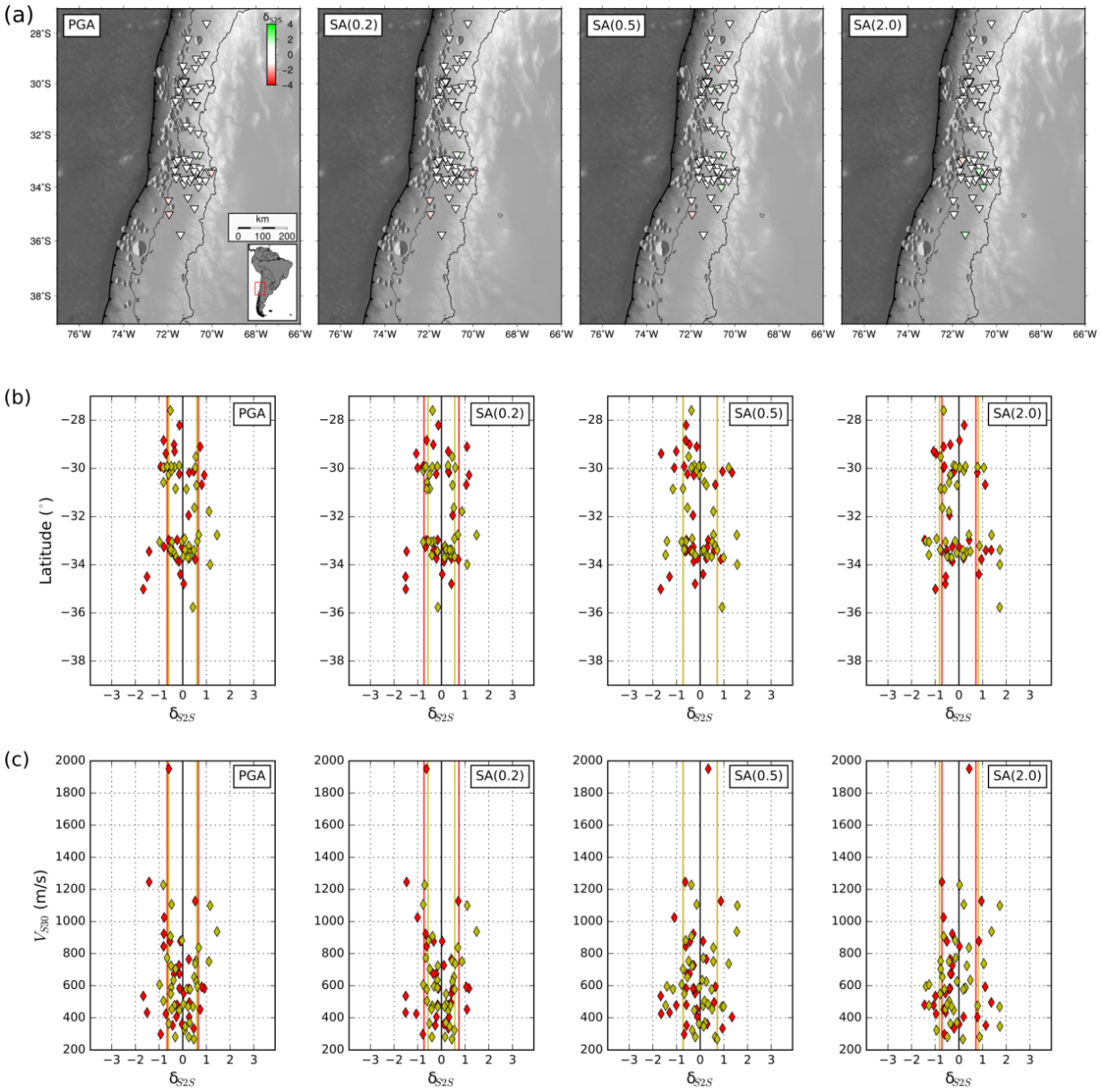

Figure A.8: Site term analysis in central Chile for PGA, SA(0.2), SA(0.5) and SA(2.0). (a) Maps showing the seismic stations analyzed, colored based on their site term values. Focal mechanisms of interplate earthquakes are shown in grey. (b) Latitudinal variation of the site term. (c) Site term variation with V_{S30}. Red symbols in rows (b) and (c) correspond to stations with inferred VS30, and yellow symbols correspond to stations with measured V_{S30} by Leyton et al. (2018). Red and yellow lines correspond to the site term standard deviations of stations with inferred and measured V_{S30}, respectively.

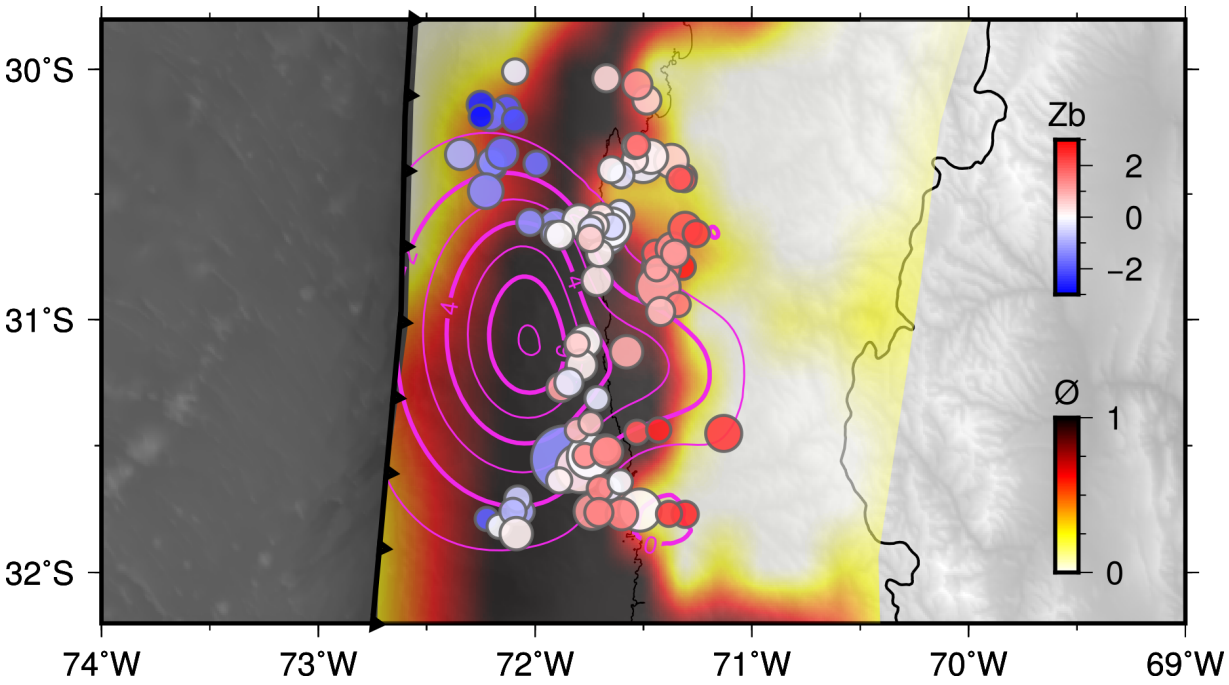

Figure A.9: Coseismic slip contours of the 2015 Mw 8.3 Illapel earthquake (Ruiz et al., 2016). Aftershocks are shown with circles colored by their respective PGA between-event residuals. The interseismic coupling model was calculated by Metois et al. (2016).

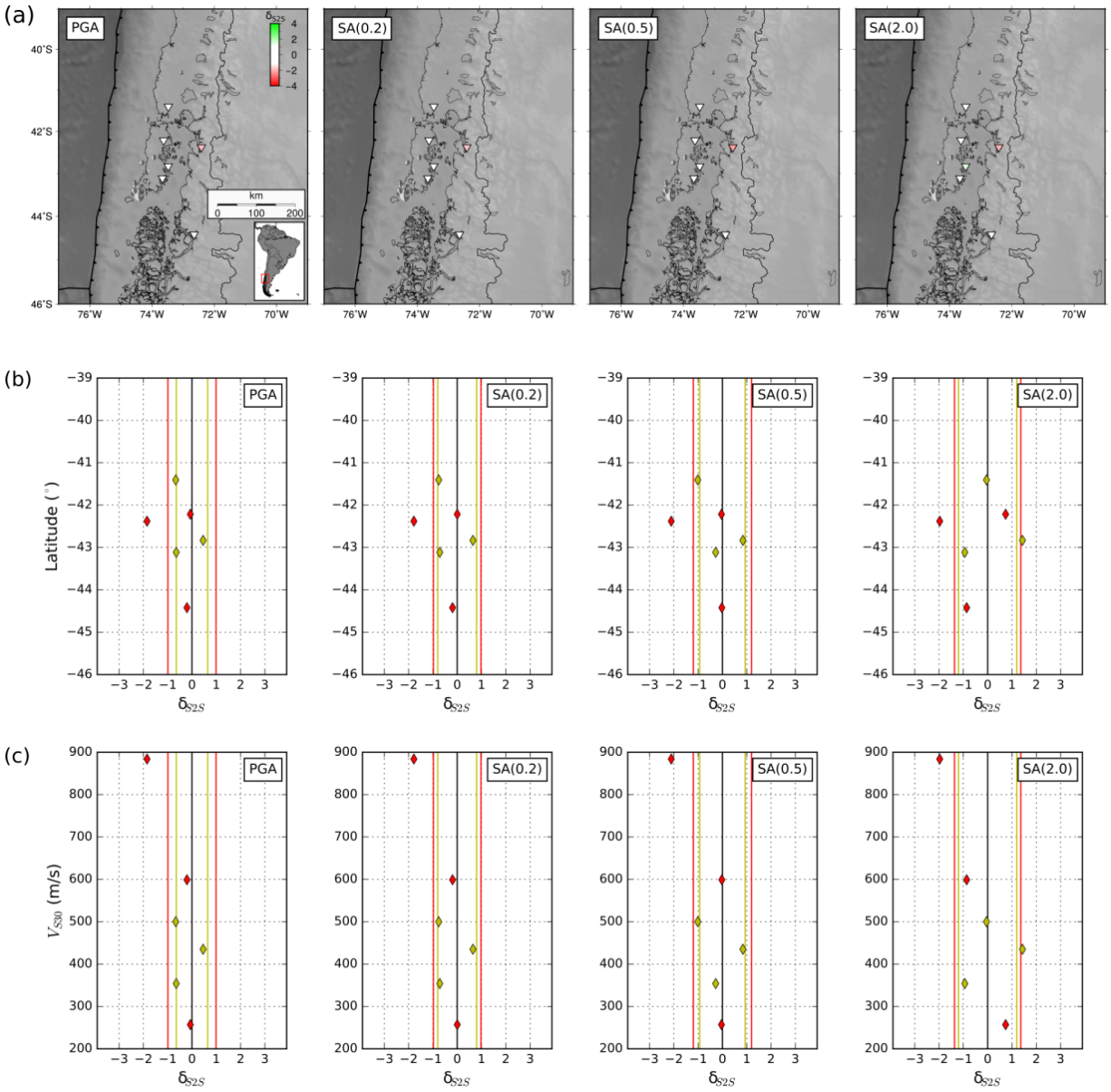

Figure A.10: Site term analysis in southern Chile for PGA, SA(0.2), SA(0.5) and SA(2.0). (a) Maps showing the seismic stations analyzed, colored based on their site term values. Focal mechanisms of interplate earthquakes are shown in grey. (b) Latitudinal variation of the site term. (c) Site term variation with V_{S30}. Red symbols in rows (b) and (c) correspond to stations with inferred VS30, and yellow symbols correspond to stations with measured V_{S30} by Leyton et al. (2018). Red and yellow lines correspond to the site term standard deviations of stations with inferred and measured V_{S30}, respectively.

Appendix B

Supplement to Chapter 3

This chapter contains supplemental results related to Chapter 3: "The crustal stress field inferred from focal mechanisms in northern Chile".

B.1 Completeness of the Bloch et al. (2014) catalogue

Local magnitudes (M_L) were calculated for the full Bloch et al. (2014) catalogue. This catalogue is reported as a separate CSV file in the electronic supplement of the published article associated to Chapter 3, which includes the M_L column. The completeness plot is shown in Figure B.1 for different subsets of this catalogue. The completeness magnitude can be estimated where there is an observable change in the slope of the cumulative curve towards lower magnitudes.

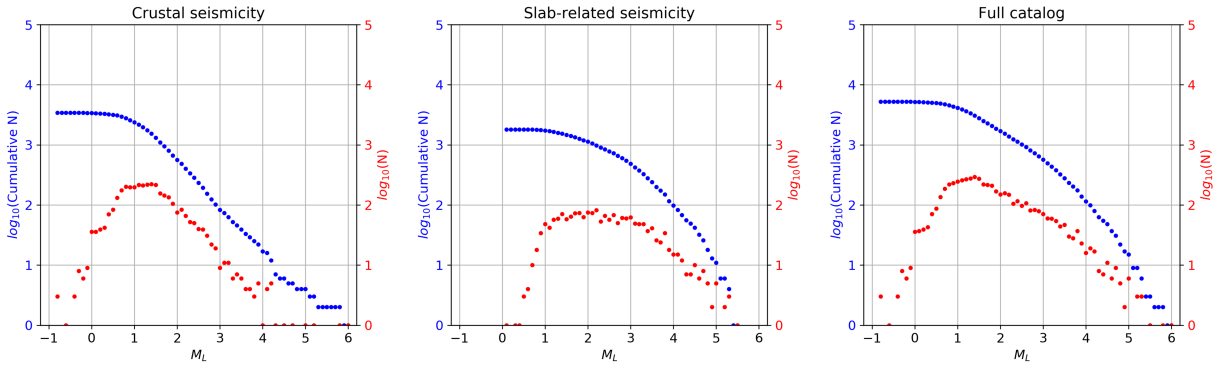

Figure B.1: Completeness plots of the Bloch et al. (2014) catalogue. Number of earthquakes (N) are separated in $\Delta M_L = 0.1$ magnitude bins.

B.2 Focal mechanism stability using HASH

HASH carries out a grid search to find the focal mechanism that best fits the observations. Limitations of the velocity model and location errors can affect the stability the final solution. This was assessed by perturbing the azimuth and takeoff angles within the HASH inversion, which results in a set of focal mechanisms. This is a non-parametric method of representing the uncertainty of the solution. A stable solution is indicated when the set of mechanisms is tightly clustered around the preferred mechanism (calculated by averaging the set of solutions after removing outliers).

The focal mechanism quality is defined by measuring the spread of the set of solutions around the preferred solution. Two parameters were used, which are part of the HASH outputs:

- Percentage of mechanisms within an angular range from the preferred mechanism.
- Root-mean-square (RMS) angular difference of the set of mechanisms to the preferred mechanism.

The quality criterion chosen in this work was the following:

- **Quality A:** At least 80% of mechanisms are within 20° from the preferred mechanism and an RMS angular difference of at most 10°.
- **Quality B:** At least 60% of mechanisms are within 20° from the preferred mechanism and an RMS angular difference of at most 20°.
- **Quality C:** At least 50% of mechanisms are within 20° from the preferred mechanism and an RMS angular difference of at most 30°.
- **Quality D:** All others.

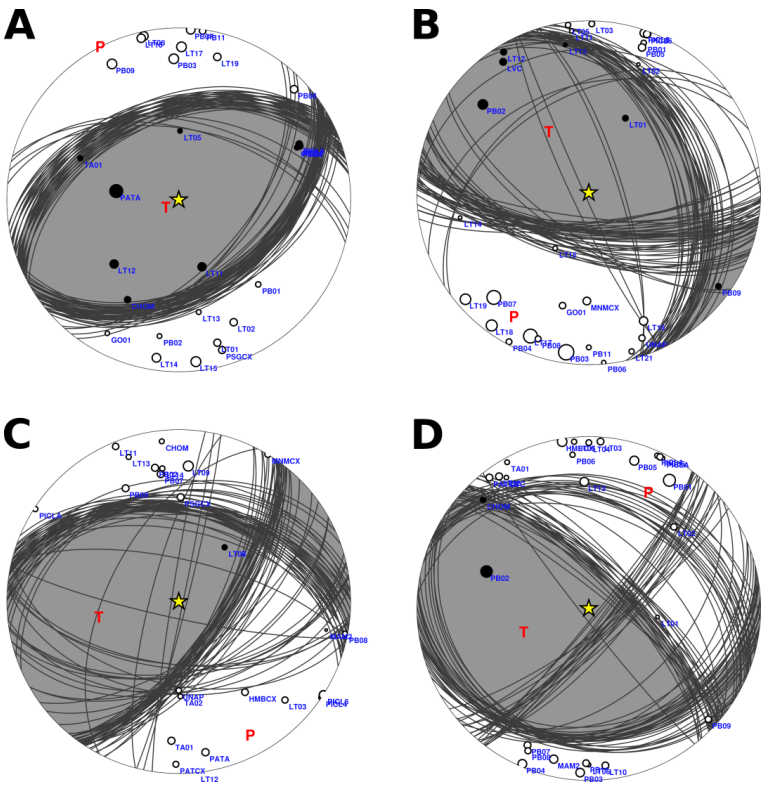

Figure B.2: Four quality classes of focal mechanisms. The mechanism with colored quadrants corresponds to the preferred solution. Positive and negative polarities are shown with black and white circles, respectively. Circle sizes are proportional to the square-root of the P/S ratio.

B.3 Catalogue of Centroid Moment Tensors (CMT)

B.3.1 Earthquake: 2008-09-10 16:12:03.44

M_W	M_{dd}	M_{ed}	M_{ee}	M_{nd}	M_{ne}	M_{nn}
5.77	0.453	-0.403	1.029	0.181	0.105	-0.57

Table B.1: M_W and CMT components of the maximum a-posteriori (MAP) solution estimated with BEAT. The six CMT components are in Nm, normalized by the seismic moment.

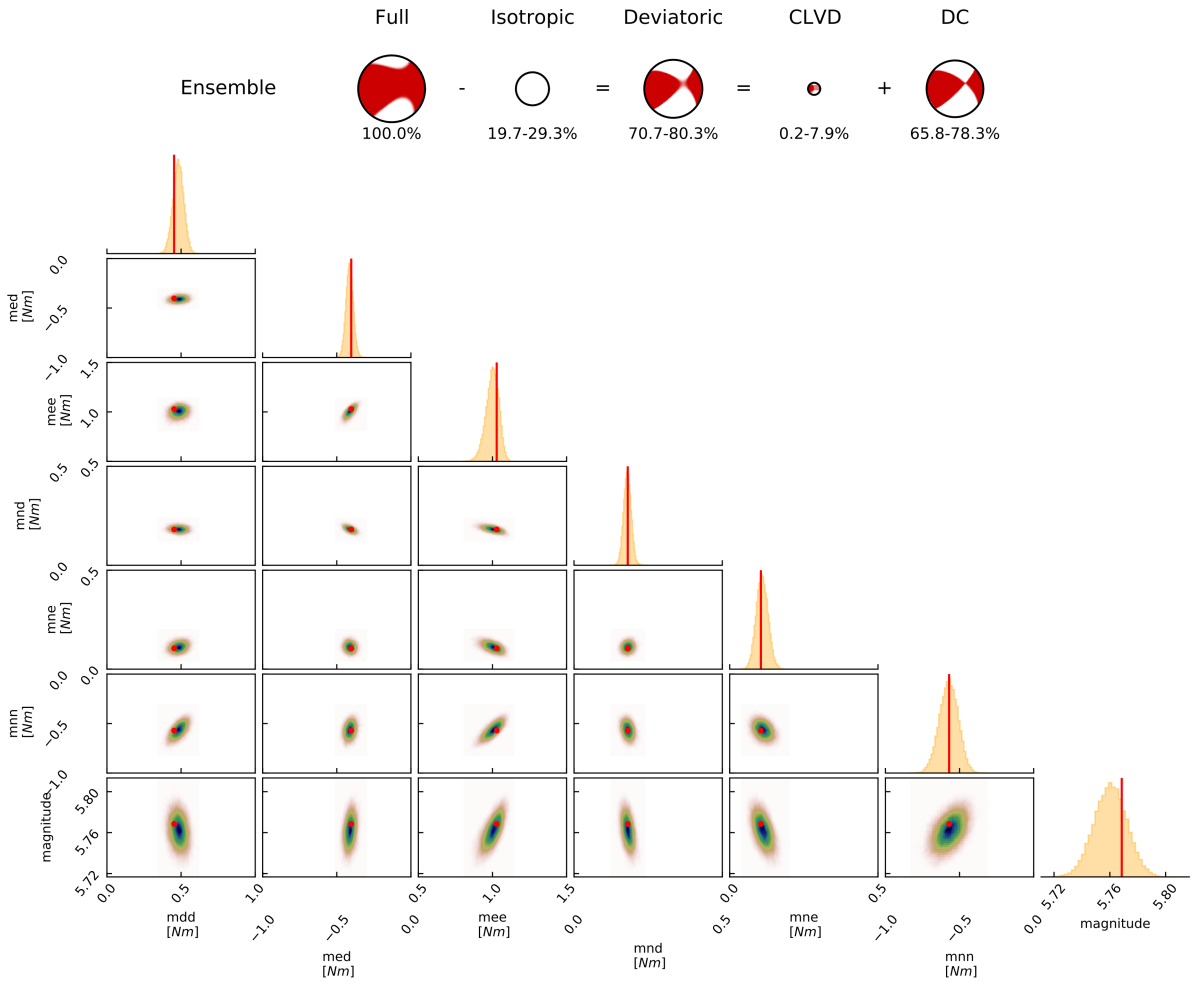

Figure B.3: Full CMT decomposition and 1-D and 2-D marginal posteriors of the six moment tensor components and magnitude. The red dot in the 2-D plots and the vertical line in the 1-D plots correspond to the MAP estimates. Blue colors in the 2-D plots show the regions of high probability.

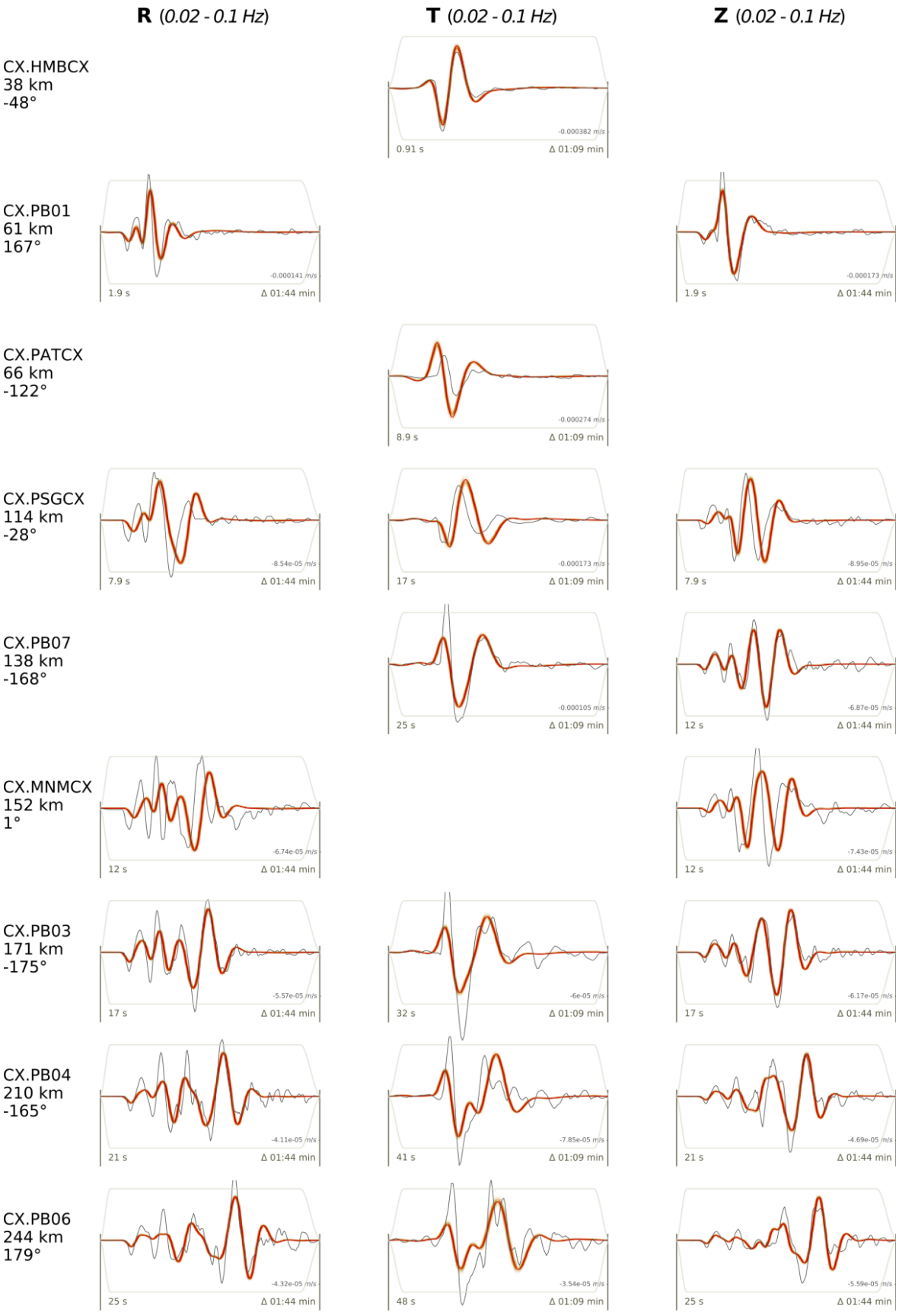
R (0.02 - 0.1 Hz)
T (0.02 - 0.1 Hz)
Z (0.02 - 0.1 Hz)
CX.HMBCX
38 km
-48°
-0.000382 m/s
0.91 s
Δ 01:09 min
CX.PB01
61 km
167°
-0.000141 m/s
1.9 s
Δ 01:44 min
-0.000173 m/s
1.9 s
Δ 01:44 min
CX.PATCX
66 km
-122°
-0.000274 m/s
8.9 s
Δ 01:09 min
CX.PSGCX
114 km
-28°
-8.54e-05 m/s
7.9 s
Δ 01:44 min
-0.000173 m/s
17 s
Δ 01:09 min
-8.95e-05 m/s
7.9 s
Δ 01:44 min
CX.PB07
138 km
-168°
-0.000105 m/s
25 s
Δ 01:09 min
-6.87e-05 m/s
12 s
Δ 01:44 min
CX.MNMCX
152 km
1°
-6.74e-05 m/s
12 s
Δ 01:44 min
-7.43e-05 m/s
12 s
Δ 01:44 min
CX.PB03
171 km
-175°
-5.57e-05 m/s
17 s
Δ 01:44 min
-6e-05 m/s
32 s
Δ 01:09 min
-6.17e-05 m/s
17 s
Δ 01:44 min
CX.PB04
210 km
-165°
-4.11e-05 m/s
21 s
Δ 01:44 min
-7.85e-05 m/s
41 s
Δ 01:09 min
-4.69e-05 m/s
21 s
Δ 01:44 min
CX.PB06
244 km
179°
-4.32e-05 m/s
25 s
Δ 01:44 min
-3.54e-05 m/s
48 s
Δ 01:09 min
-5.59e-05 m/s
25 s
Δ 01:44 min

Continued

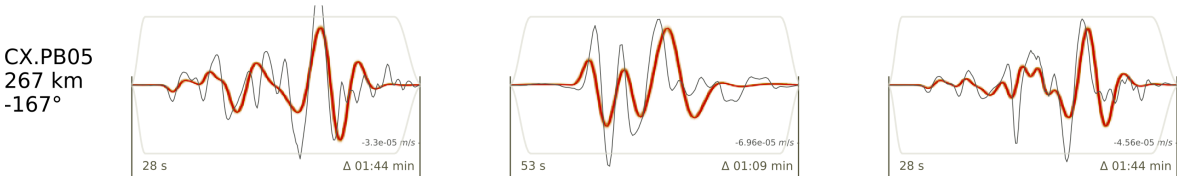

Figure B.4: Observed (grey) and synthetic (red) waveforms of radial, transverse, and vertical components (R, T, and Z, respectively). The shading around the red seismograms is composed of 100 random synthetic seismograms drawn from the posterior probability density. Labels on the left are network code, station code, epicentral distance and azimuth. Labels within the plots are window start time after centroid time (left), window duration (bottom right) and amplitude (top right).

B.3.2 Earthquake: 2010-04-04 13:34:24.79

M_W	M_{dd}	M_{ed}	M_{ee}	M_{nd}	M_{ne}	M_{nn}
4.12	0.986	-0.135	-0.059	-0.02	-0.299	-0.899

Table B.2: M_W and CMT components of the maximum a-posteriori (MAP) solution estimated with BEAT. The six CMT components are in Nm, normalized by the seismic moment.

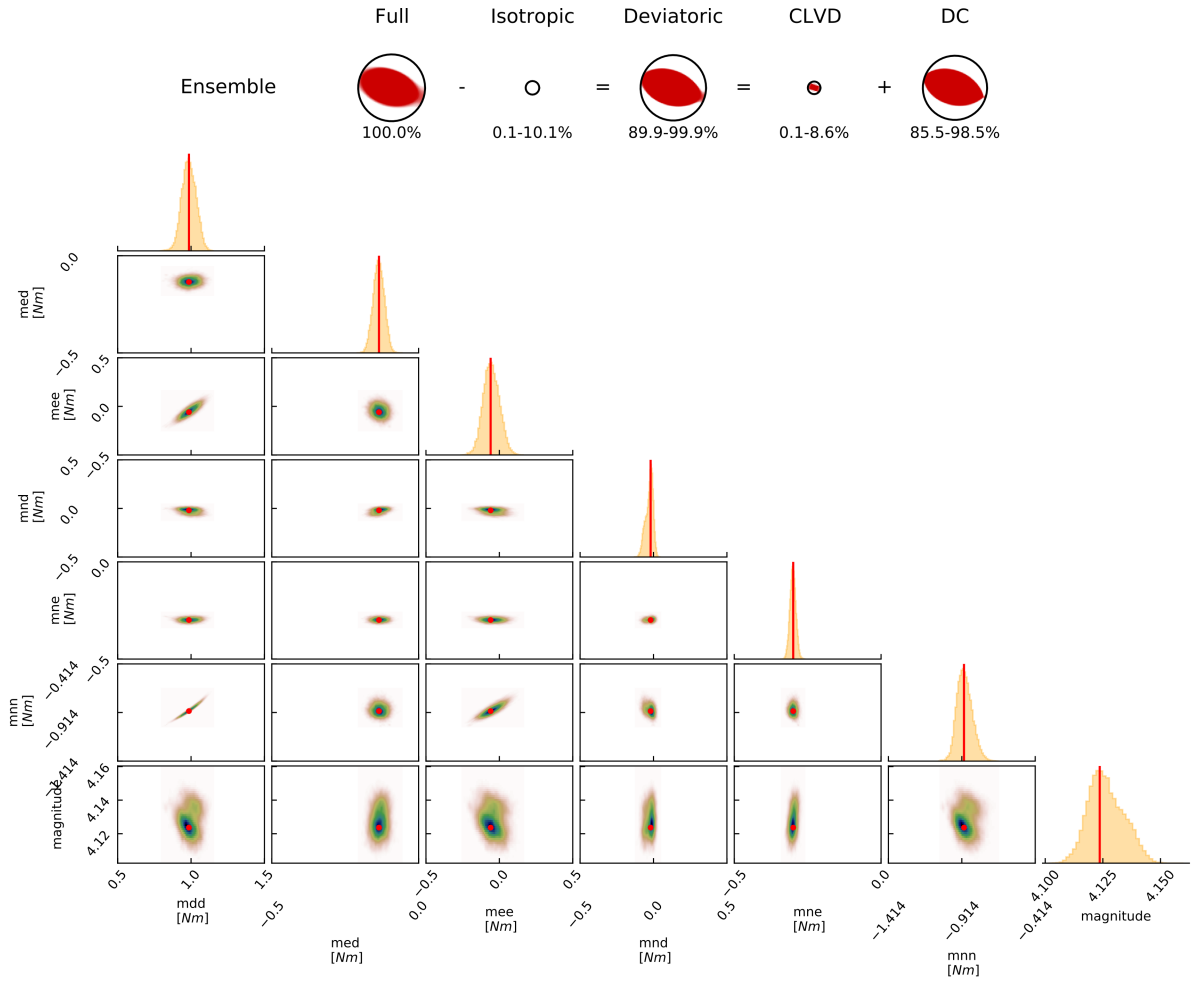

Figure B.5: Full CMT decomposition and 1-D and 2-D marginal posteriors of the six moment tensor components and magnitude. The red dot in the 2-D plots and the vertical line in the 1-D plots correspond to the MAP estimates. Blue colors in the 2-D plots show the regions of high probability.

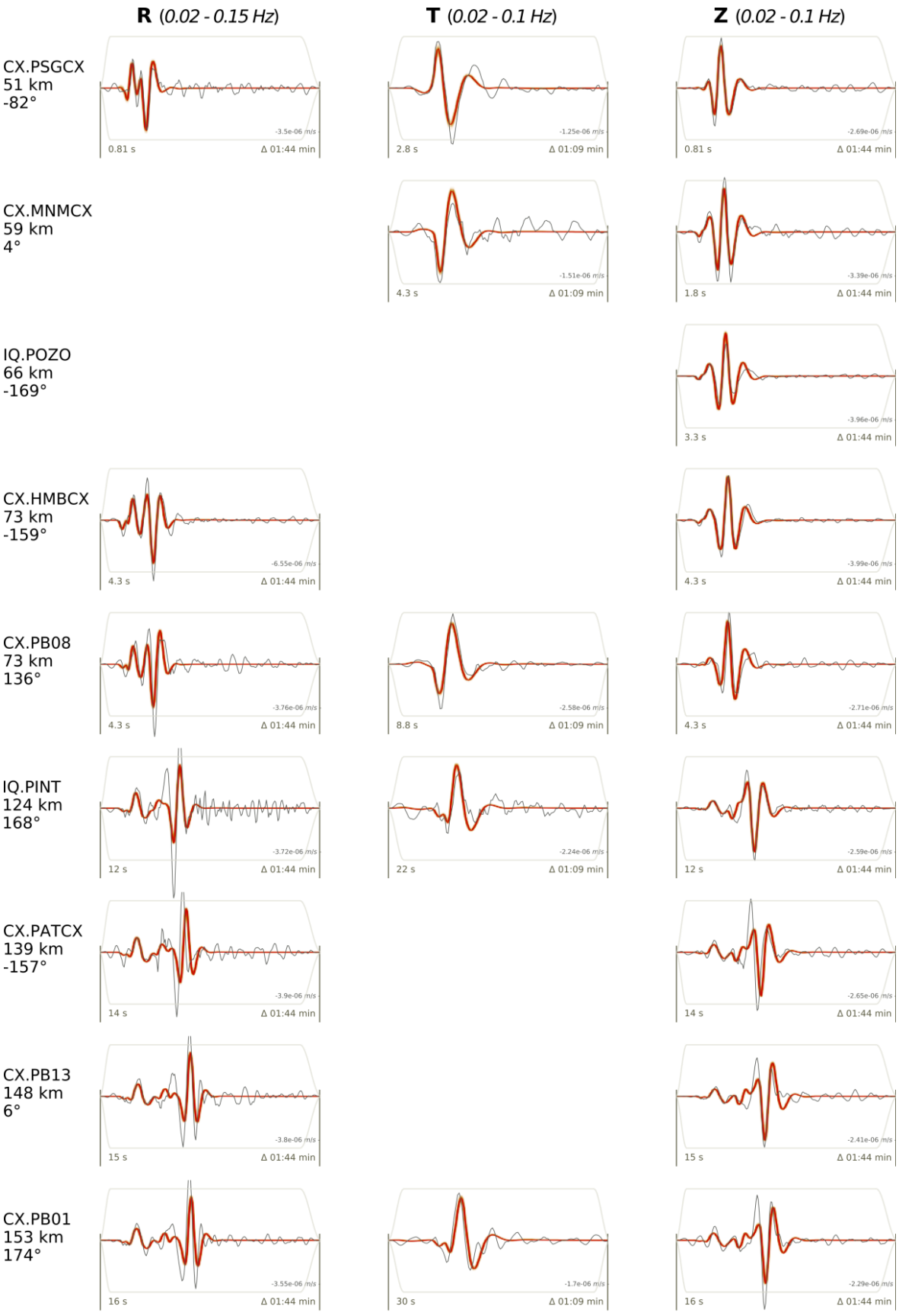
R (0.02 - 0.15 Hz)
T (0.02 - 0.1 Hz)
Z (0.02 - 0.1 Hz)
CX.PSGCX
51 km
-82°
0.81 s
Δ 01:44 min
2.8 s
Δ 01:09 min
CX.MNMCX
59 km
4°
4.3 s
1.8 s
IQ.POZO
66 km
-169°
3.3 s
CX.HMBCX
73 km
-159°
CX.PB08
73 km
136°
8.8 s
IQ.PINT
124 km
168°
12 s
22 s
CX.PATCX
139 km
-157°
14 s
CX.PB13
148 km
6°
15 s
CX.PB01
153 km
174°
16 s
30 s

Continued

CX.PB02
185 km
-172°

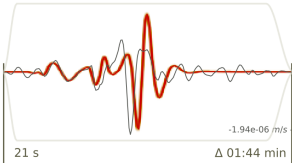

Figure B.6: Observed (grey) and synthetic (red) waveforms of radial, transverse, and vertical components (R, T, and Z, respectively). The shading around the red seismograms is composed of 100 random synthetic seismograms drawn from the posterior probability density. Labels on the left are network code, station code, epicentral distance and azimuth. Labels within the plots are window start time after centroid time (left), window duration (bottom right) and amplitude (top right).

B.3.3 Earthquake: 2010-06-05 15:18:17.00

M_W	M_{dd}	M_{ed}	M_{ee}	M_{nd}	M_{ne}	M_{nn}
4.49	0.207	0.4	0.368	0.363	0.037	-1.112

Table B.3: M_W and CMT components of the maximum a-posteriori (MAP) solution estimated with BEAT. The six CMT components are in Nm, normalized by the seismic moment.

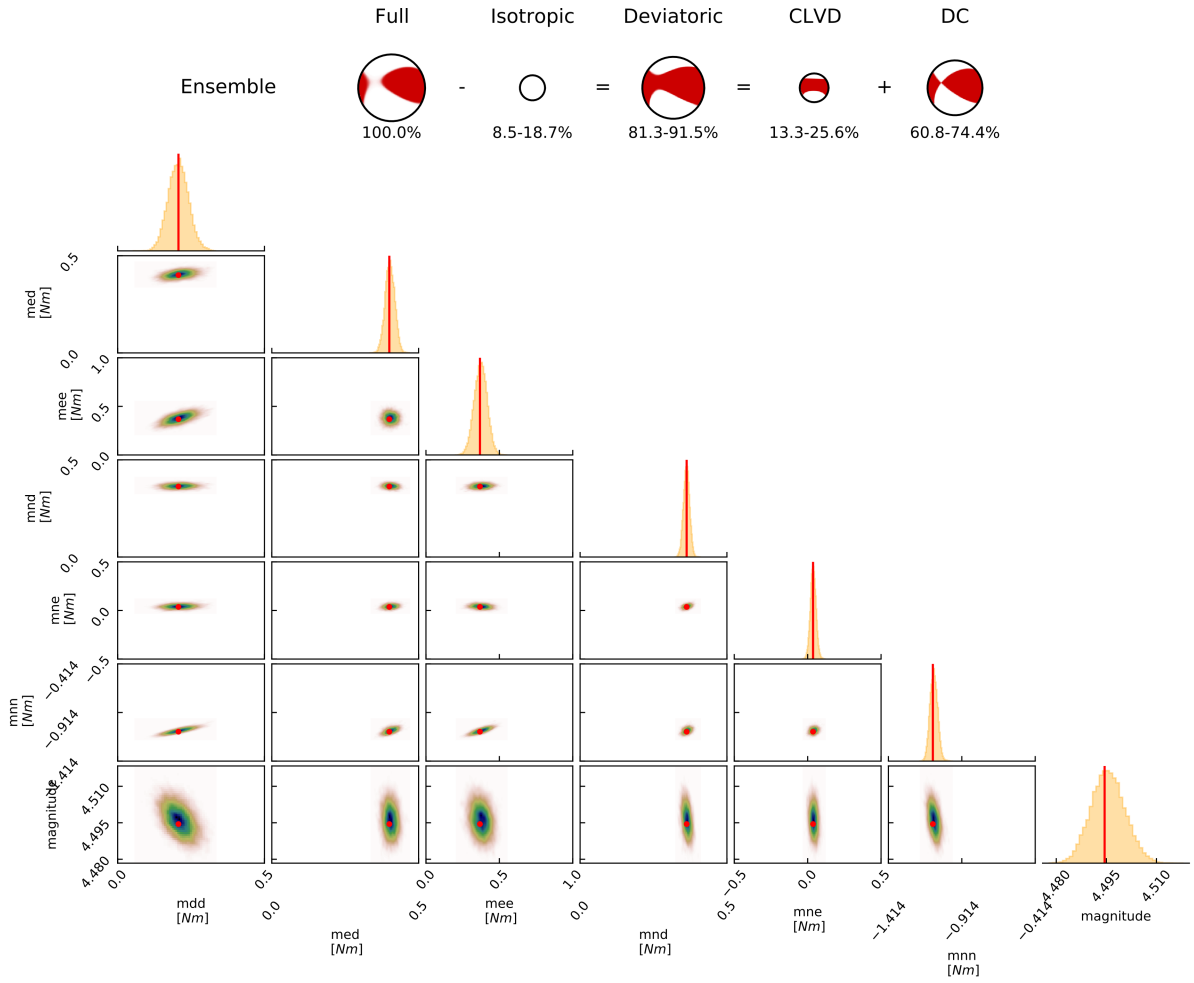

Figure B.7: Full CMT decomposition and 1-D and 2-D marginal posteriors of the six moment tensor components and magnitude. The red dot in the 2-D plots and the vertical line in the 1-D plots correspond to the MAP estimates. Blue colors in the 2-D plots show the regions of high probability.


R (0.02 - 0.1 Hz)
T (0.02 - 0.1 Hz)
Z (0.02 - 0.1 Hz)
CX.PB07
22 km
154°
-7.13e-06 m/s
-3.9 s
Δ 01:44 min
-6.29e-06 m/s
-3.9 s
Δ 01:44 min
CX.PB01
76 km
43°
-2.42e-06 m/s
3.1 s
Δ 01:44 min
-6.77e-06 m/s
8.1 s
Δ 01:09 min
-2.98e-06 m/s
3.1 s
Δ 01:44 min
CX.PATCX
82 km
-12°
-3.38e-06 m/s
4.1 s
Δ 01:44 min
-2.74e-06 m/s
10 s
Δ 01:09 min
-1.97e-06 m/s
4.1 s
Δ 01:44 min
CX.PB09
82 km
110°
-3.95e-06 m/s
8.6 s
Δ 01:09 min
CX.PB04
89 km
-169°
-2.43e-06 m/s
4.6 s
Δ 01:44 min
-2.47e-06 m/s
11 s
Δ 01:09 min
IQ.PINT
106 km
35°
-4.09e-06 m/s
16 s
Δ 01:09 min
-2.69e-06 m/s
7.6 s
Δ 01:44 min
IU.LVC
162 km
137°
-2.61e-06 m/s
28 s
Δ 01:09 min
CX.PB08
178 km
29°
-1.28e-06 m/s
17 s
Δ 01:44 min
-1.86e-06 m/s
33 s
Δ 01:09 min
-1.81e-06 m/s
17 s
Δ 01:44 min
CX.PB11
200 km
10°
-1.59e-06 m/s
20 s
Δ 01:44 min

Figure B.8: Observed (grey) and synthetic (red) waveforms of radial, transverse, and vertical components (R, T, and Z, respectively). The shading around the red seismograms is composed of 100 random synthetic seismograms drawn from the posterior probability density. Labels on the left are network code, station code, epicentral distance and azimuth. Labels within the plots are window start time after centroid time (left), window duration (bottom right) and amplitude (top right).

B.3.4 Earthquake: 2014-02-05 11:51:05.37

M_W	M_{dd}	M_{ed}	M_{ee}	M_{nd}	M_{ne}	M_{nn}
4.77	0.538	0.347	0.627	0.097	-0.167	-1.001

Table B.4: M_W and CMT components of the maximum a-posteriori (MAP) solution estimated with BEAT. The six CMT components are in Nm, normalized by the seismic moment.

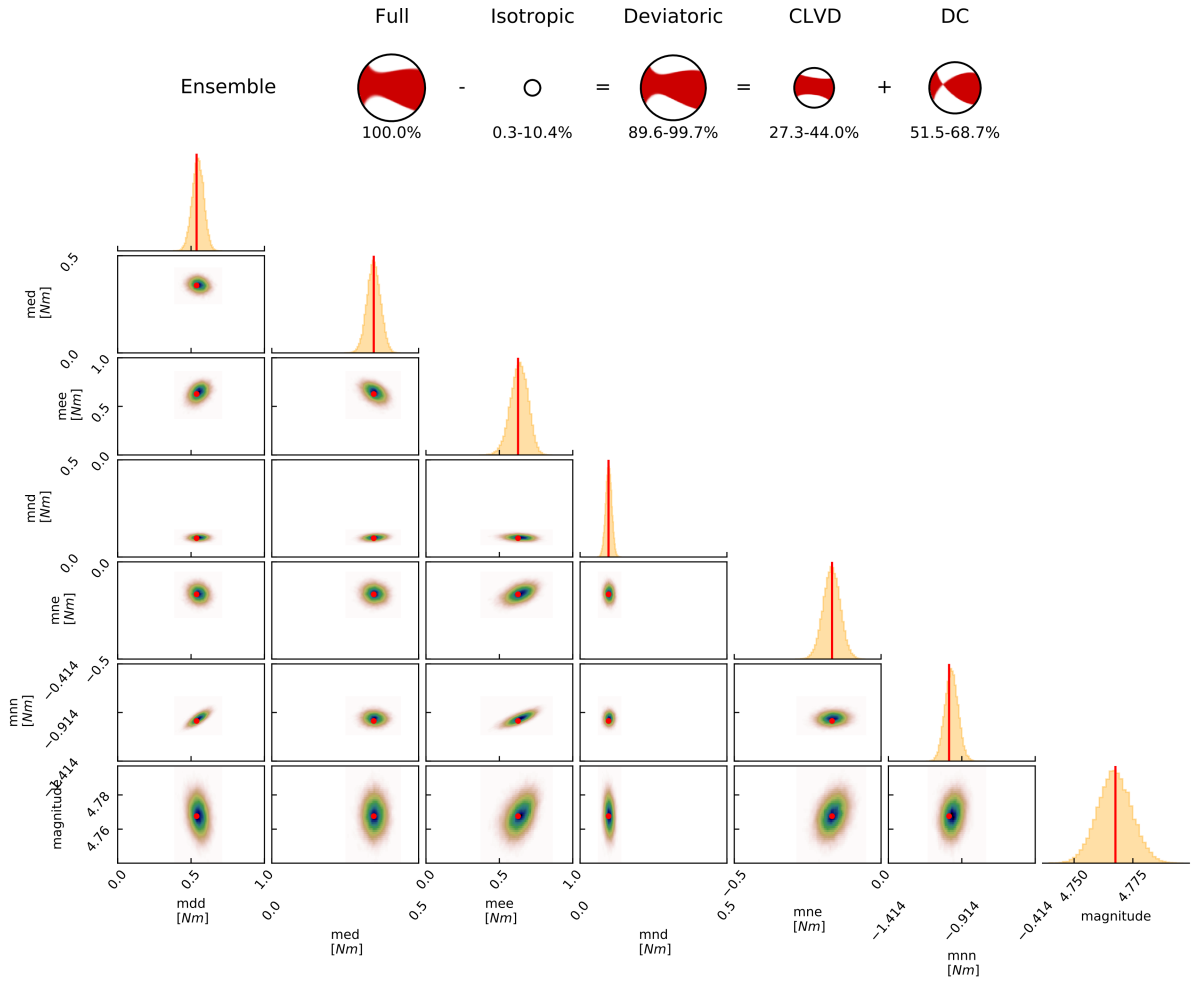

Figure B.9: Full CMT decomposition and 1-D and 2-D marginal posteriors of the six moment tensor components and magnitude. The red dot in the 2-D plots and the vertical line in the 1-D plots correspond to the MAP estimates. Blue colors in the 2-D plots show the regions of high probability.


R (0.02 - 0.1 Hz)
T (0.02 - 0.1 Hz)
Z (0.02 - 0.1 Hz)
CX.PB03
76 km
-168°
-9.01e-06 m/s
4.4 s
Δ 01:44 min
IQ.PATA
87 km
-28°
-1.17e-05 m/s
13 s
Δ 01:09 min
-3.49e-06 m/s
6.4 s
Δ 01:44 min
IQ.PICL
103 km
20°
-5.73e-06 m/s
7.4 s
Δ 01:44 min
CX.PB04
120 km
-152°
-5.86e-06 m/s
20 s
Δ 01:09 min
-3.07e-06 m/s
10 s
Δ 01:44 min
IQ.UNAP
137 km
-24°
-2.4e-06 m/s
13 s
Δ 01:44 min
-5.81e-06 m/s
24 s
Δ 01:09 min
-2.68e-06 m/s
13 s
Δ 01:44 min
CX.PB08
145 km
19°
-2.89e-06 m/s
13 s
Δ 01:44 min
-4.12e-06 m/s
13 s
Δ 01:44 min
CX.PB06
147 km
179°
-2.7e-06 m/s
13 s
Δ 01:44 min
-3.26e-06 m/s
13 s
Δ 01:44 min
IU.LVC
154 km
153°
-6.02e-06 m/s
26 s
Δ 01:09 min
-2.68e-06 m/s
13 s
Δ 01:44 min
CX.PB05
174 km
-160°
-2.7e-06 m/s
17 s
Δ 01:44 min

CX.PB11
179 km
-2°

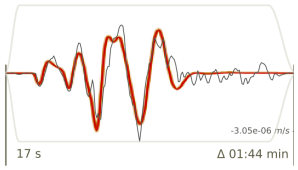

CX.PSGCX
204 km
-15°

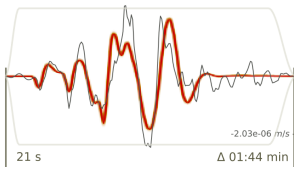

Figure B.10: Observed (grey) and synthetic (red) waveforms of radial, transverse, and vertical components (R, T, and Z, respectively). The shading around the red seismograms is composed of 100 random synthetic seismograms drawn from the posterior probability density. Labels on the left are network code, station code, epicentral distance and azimuth. Labels within the plots are window start time after centroid time (left), window duration (bottom right) and amplitude (top right).

B.3.5 Earthquake: 2014-03-17 08:32:37.52

M_W	M_{dd}	M_{ed}	M_{ee}	M_{nd}	M_{ne}	M_{nn}
5.2	0.084	-0.652	0.224	0.724	-0.149	0.038

Table B.5: M_W and CMT components of the maximum a-posteriori (MAP) solution estimated with BEAT. The six CMT components are in Nm, normalized by the seismic moment.

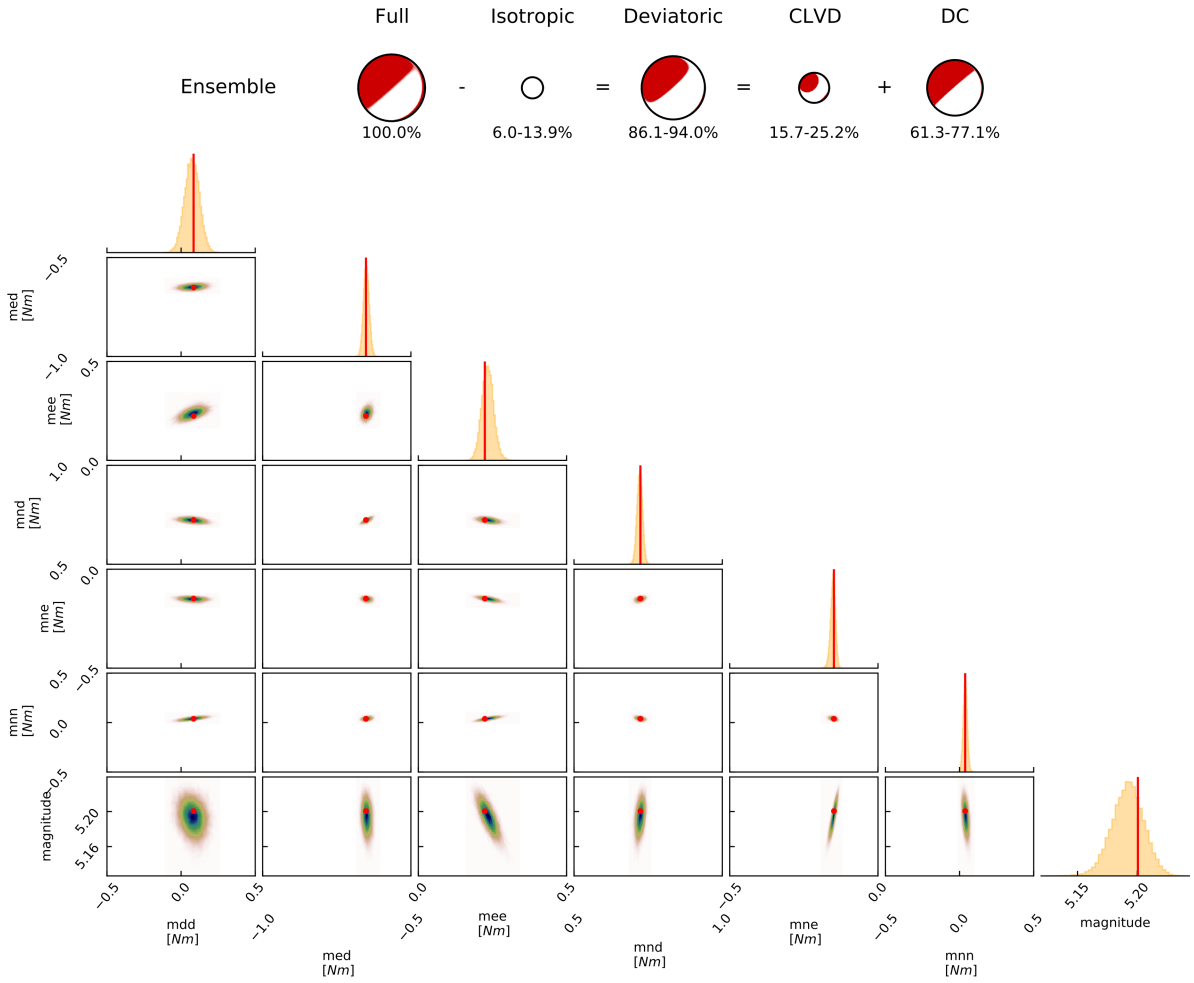

Figure B.11: Full CMT decomposition and 1-D and 2-D marginal posteriors of the six moment tensor components and magnitude. The red dot in the 2-D plots and the vertical line in the 1-D plots correspond to the MAP estimates. Blue colors in the 2-D plots show the regions of high probability.

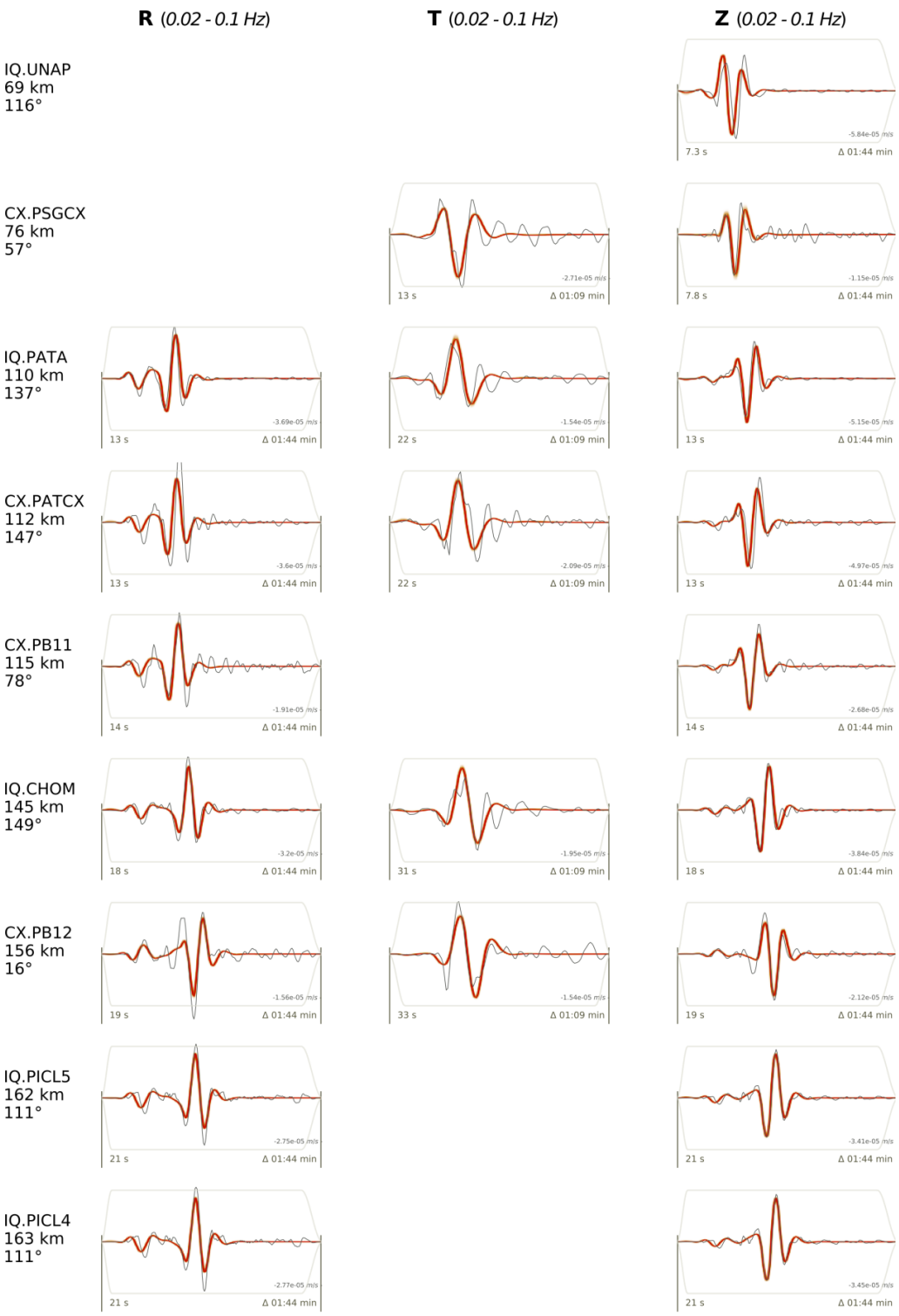
R (0.02 - 0.1 Hz)
T (0.02 - 0.1 Hz)
Z (0.02 - 0.1 Hz)
IQ.UNAP
69 km
116°
CX.PSGCX
76 km
57°
IQ.PATA
110 km
137°
CX.PATCX
112 km
147°
CX.PB11
115 km
78°
IQ.CHOM
145 km
149°
CX.PB12
156 km
16°
IQ.PICL5
162 km
111°
IQ.PICL4
163 km
111°
Δ 01:44 min
Δ 01:09 min

Figure B.12: Observed (grey) and synthetic (red) waveforms of radial, transverse, and vertical components (R, T, and Z, respectively). The shading around the red seismograms is composed of 100 random synthetic seismograms drawn from the posterior probability density. Labels on the left are network code, station code, epicentral distance and azimuth. Labels within the plots are window start time after centroid time (left), window duration (bottom right) and amplitude (top right).

B.3.6 Earthquake: 2014-04-05 19:21:44.32

M_W	M_{dd}	M_{ed}	M_{ee}	M_{nd}	M_{ne}	M_{nn}
4.22	-0.237	0.576	-0.72	0.574	-0.226	-0.033

Table B.6: M_W and CMT components of the maximum a-posteriori (MAP) solution estimated with BEAT. The six CMT components are in Nm, normalized by the seismic moment.

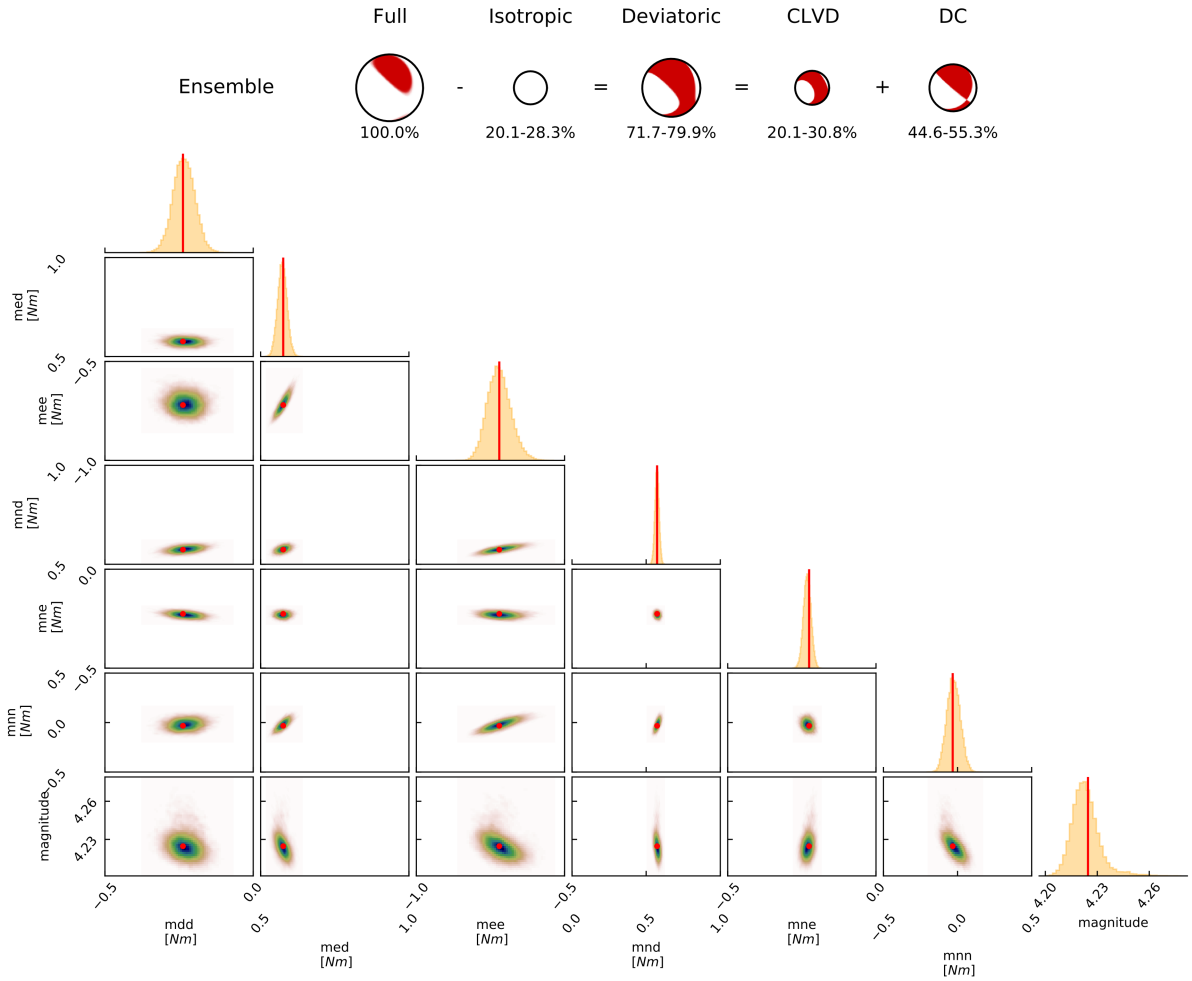

Figure B.13: Full CMT decomposition and 1-D and 2-D marginal posteriors of the six moment tensor components and magnitude. The red dot in the 2-D plots and the vertical line in the 1-D plots correspond to the MAP estimates. Blue colors in the 2-D plots show the regions of high probability.

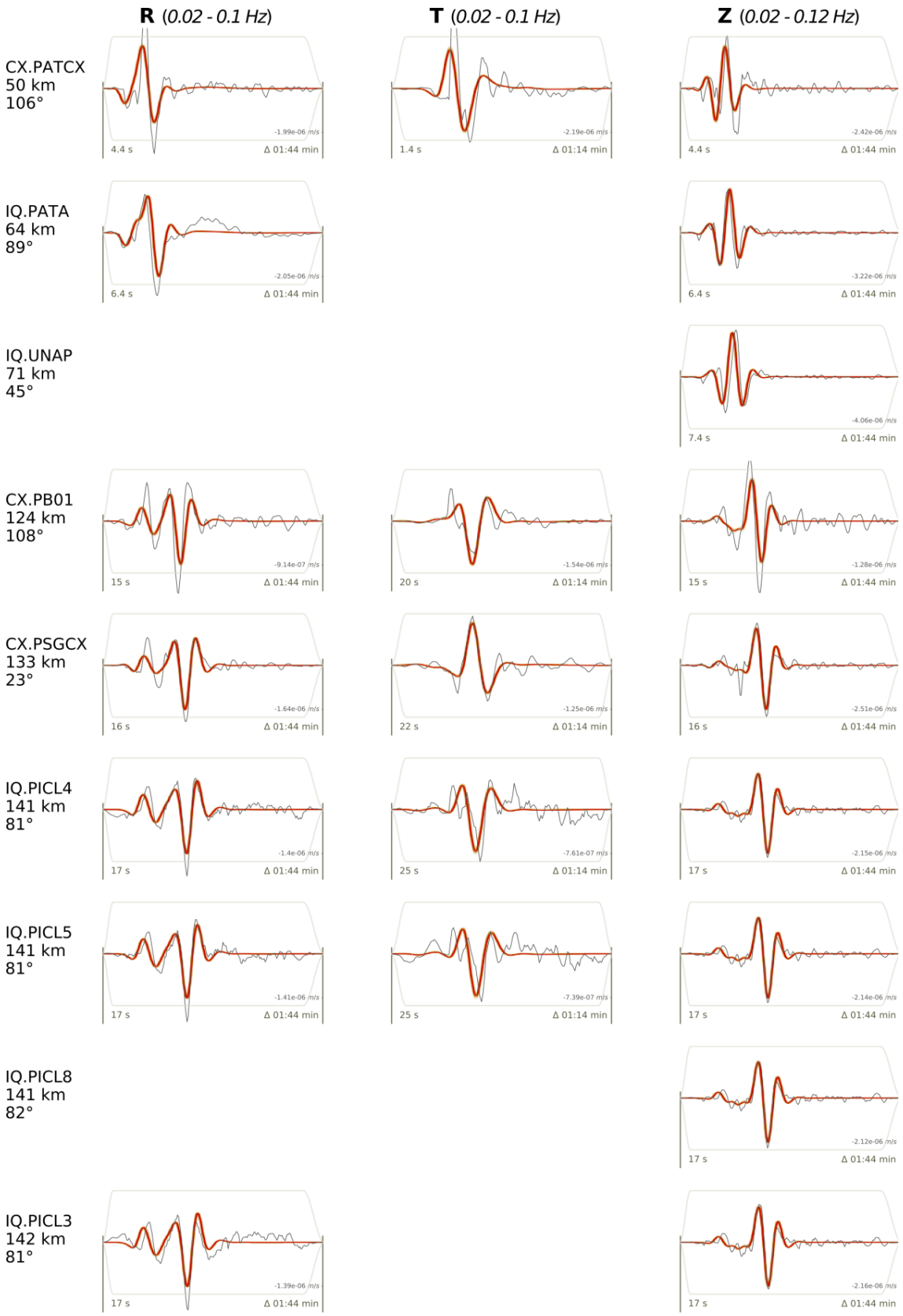
R (0.02 - 0.1 Hz)
T (0.02 - 0.1 Hz)
Z (0.02 - 0.12 Hz)
CX.PATCX
50 km
106°
IQ.PATA
64 km
89°
IQ.UNAP
71 km
45°
CX.PB01
124 km
108°
CX.PSGCX
133 km
23°
IQ.PICL4
141 km
81°
IQ.PICL5
141 km
81°
IQ.PICL8
141 km
82°
IQ.PICL3
142 km
81°
Δ 01:44 min
Δ 01:14 min

Continued

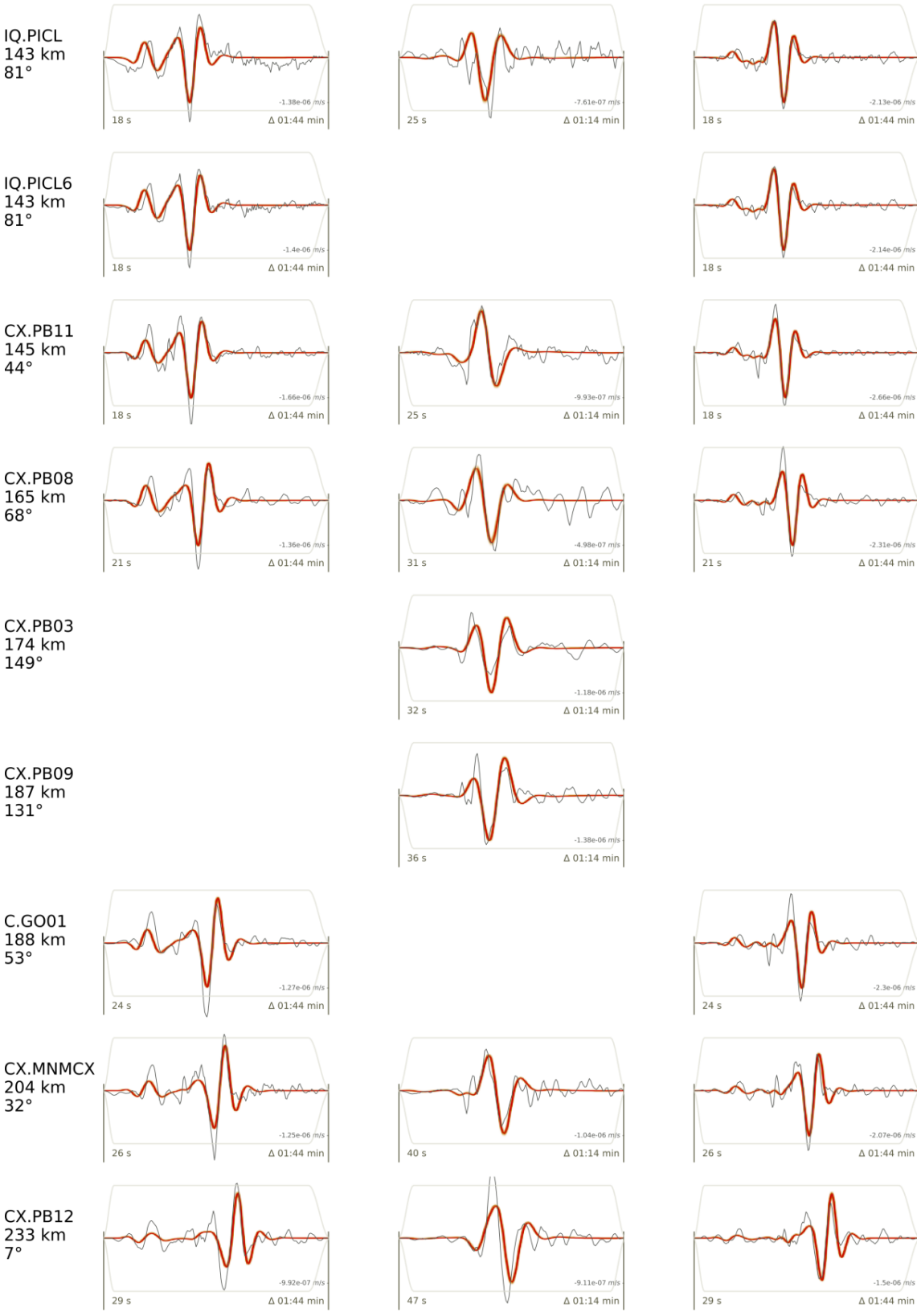
IQ.PICL
143 km
81°
-1.38e-06 m/s
18 s
Δ 01:44 min
-7.61e-07 m/s
25 s
Δ 01:14 min
-2.13e-06 m/s
18 s
Δ 01:44 min
IQ.PICL6
143 km
81°
-1.4e-06 m/s
18 s
Δ 01:44 min
-2.14e-06 m/s
18 s
Δ 01:44 min
CX.PB11
145 km
44°
-1.66e-06 m/s
18 s
Δ 01:44 min
-9.93e-07 m/s
25 s
Δ 01:14 min
-2.66e-06 m/s
18 s
Δ 01:44 min
CX.PB08
165 km
68°
-1.36e-06 m/s
21 s
Δ 01:44 min
-4.98e-07 m/s
31 s
Δ 01:14 min
-2.31e-06 m/s
21 s
Δ 01:44 min
CX.PB03
174 km
149°
-1.18e-06 m/s
32 s
Δ 01:14 min
CX.PB09
187 km
131°
-1.38e-06 m/s
36 s
Δ 01:14 min
C.GO01
188 km
53°
-1.27e-06 m/s
24 s
Δ 01:44 min
-2.3e-06 m/s
24 s
Δ 01:44 min
CX.MNMCX
204 km
32°
-1.25e-06 m/s
26 s
Δ 01:44 min
-1.04e-06 m/s
40 s
Δ 01:14 min
-2.07e-06 m/s
26 s
Δ 01:44 min
CX.PB12
233 km
7°
-9.92e-07 m/s
29 s
Δ 01:44 min
-9.11e-07 m/s
47 s
Δ 01:14 min
-1.5e-06 m/s
29 s
Δ 01:44 min

Continued

Figure B.14: Observed (grey) and synthetic (red) waveforms of radial, transverse, and vertical components (R, T, and Z, respectively). The shading around the red seismograms is composed of 100 random synthetic seismograms drawn from the posterior probability density. Labels on the left are network code, station code, epicentral distance and azimuth. Labels within the plots are window start time after centroid time (left), window duration (bottom right) and amplitude (top right).

B.3.7 Earthquake: 2014-04-09 12:20:10.43

M_W	M_{dd}	M_{ed}	M_{ee}	M_{nd}	M_{ne}	M_{nn}
4.09	-0.667	0.484	0.494	-0.253	0.492	-0.481

Table B.7: M_W and CMT components of the maximum a-posteriori (MAP) solution estimated with BEAT. The six CMT components are in Nm, normalized by the seismic moment.

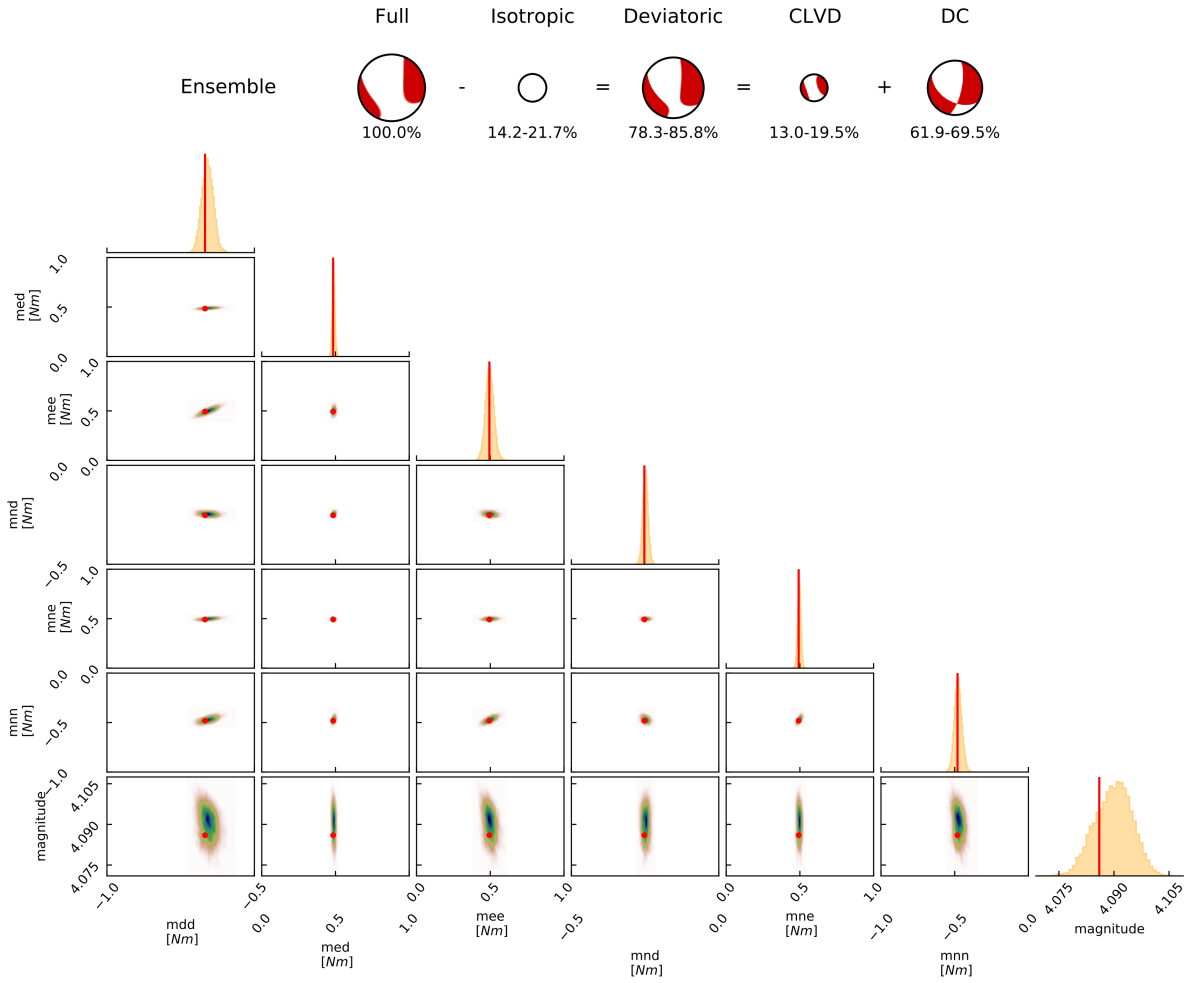

Figure B.15: Full CMT decomposition and 1-D and 2-D marginal posteriors of the six moment tensor components and magnitude. The red dot in the 2-D plots and the vertical line in the 1-D plots correspond to the MAP estimates. Blue colors in the 2-D plots show the regions of high probability.

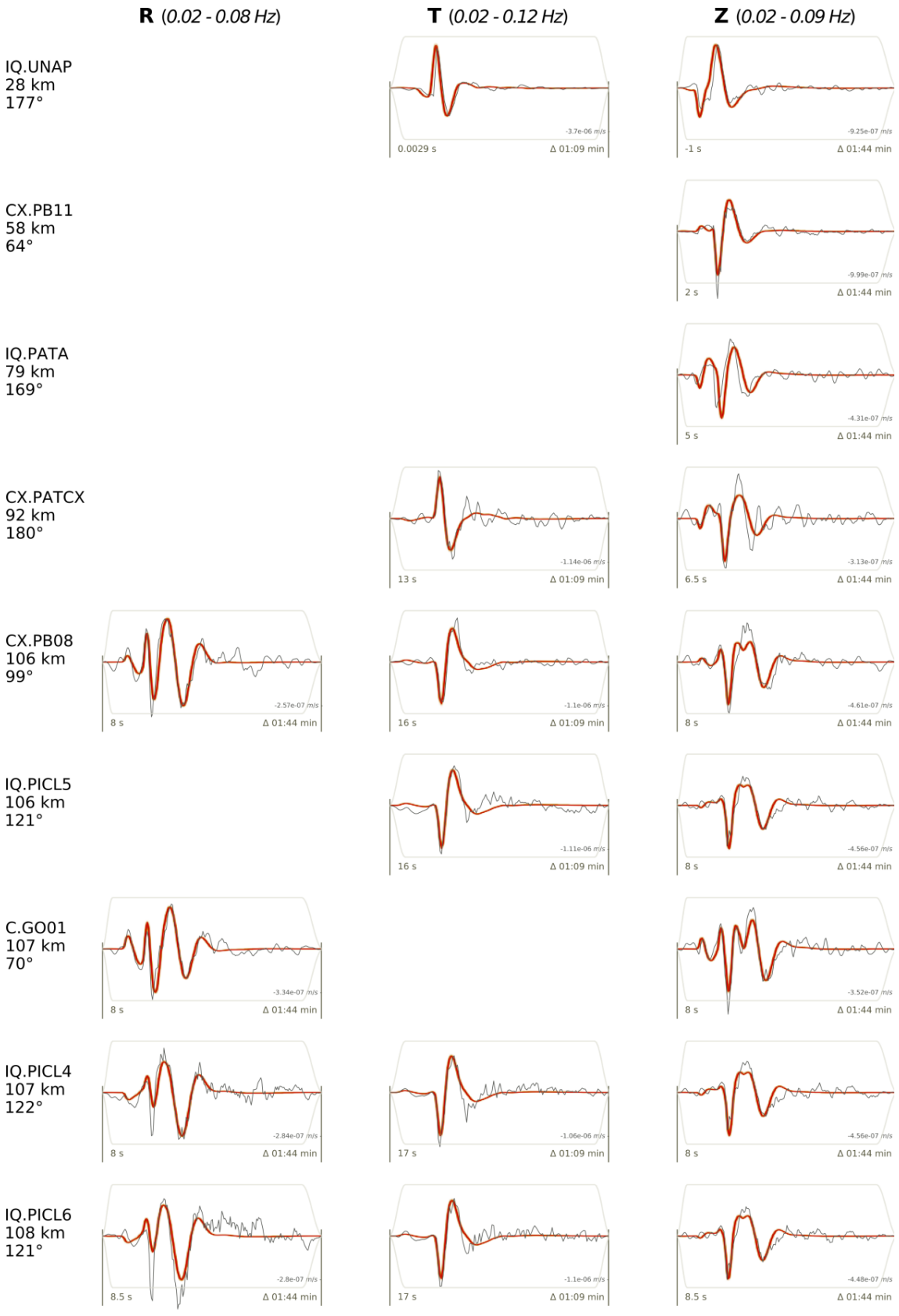
R (0.02 - 0.08 Hz)
T (0.02 - 0.12 Hz)
Z (0.02 - 0.09 Hz)
IQ.UNAP
28 km
177°
-3.7e-06 m/s
0.0029 s
Δ 01:09 min
-9.25e-07 m/s
-1 s
Δ 01:44 min
CX.PB11
58 km
64°
-9.99e-07 m/s
2 s
Δ 01:44 min
IQ.PATA
79 km
169°
-4.31e-07 m/s
5 s
Δ 01:44 min
CX.PATCX
92 km
180°
-1.14e-06 m/s
13 s
Δ 01:09 min
-3.13e-07 m/s
6.5 s
Δ 01:44 min
CX.PB08
106 km
99°
-2.57e-07 m/s
8 s
Δ 01:44 min
-1.1e-06 m/s
16 s
Δ 01:09 min
-4.61e-07 m/s
8 s
Δ 01:44 min
IQ.PICL5
106 km
121°
-1.11e-06 m/s
16 s
Δ 01:09 min
-4.56e-07 m/s
8 s
Δ 01:44 min
C.GO01
107 km
70°
-3.34e-07 m/s
8 s
Δ 01:44 min
-3.52e-07 m/s
8 s
Δ 01:44 min
IQ.PICL4
107 km
122°
-2.84e-07 m/s
8 s
Δ 01:44 min
-1.06e-06 m/s
17 s
Δ 01:09 min
-4.56e-07 m/s
8 s
Δ 01:44 min
IQ.PICL6
108 km
121°
-2.8e-07 m/s
8.5 s
Δ 01:44 min
-1.1e-06 m/s
17 s
Δ 01:09 min
-4.48e-07 m/s
8.5 s
Δ 01:44 min

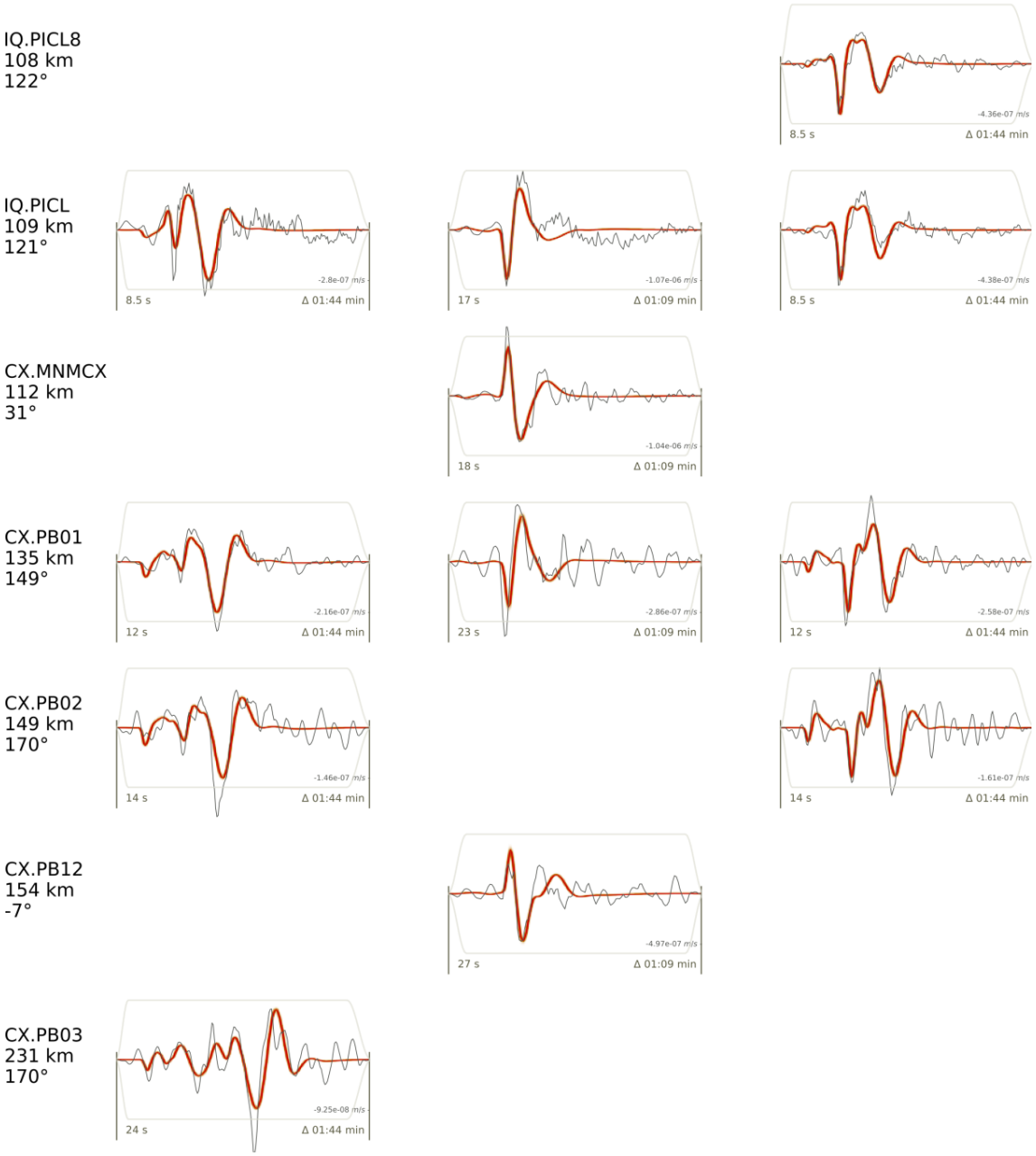

Figure B.16: Observed (grey) and synthetic (red) waveforms of radial, transverse, and vertical components (R, T, and Z, respectively). The shading around the red seismograms is composed of 100 random synthetic seismograms drawn from the posterior probability density. Labels on the left are network code, station code, epicentral distance and azimuth. Labels within the plots are window start time after centroid time (left), window duration (bottom right) and amplitude (top right).

B.4 Comparison between HASH and BEAT solutions

Earthquake	HASH	BEAT
Origin time: 2008-09-10 16:12:03.44 Location: Onshore. Central Valley. Magnitudes: M_L = 6.3; M_W = 5.8 Kagan angle = 76.2º	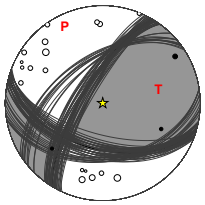	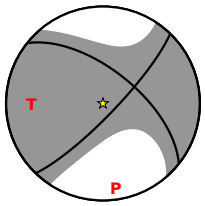
Origin time: 2010-04-04 13:34:24.79 Region: Onshore. East flank of Coastal Cordillera. Magnitudes: M_L = 5.0; M_W = 4.1 Kagan angle = 24.5º	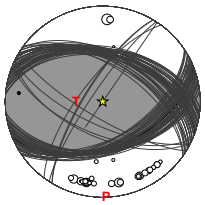	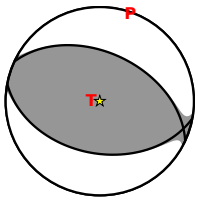
Origin time: 2010-06-05 15:18:17.00 Region: Onshore. Coastal Cordillera. Magnitudes: M_L = 5.2; M_W = 4.5 Kagan angle = 47.9º	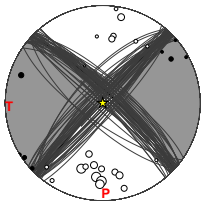	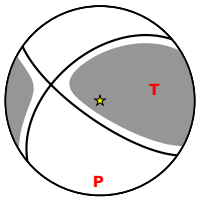
Origin time: 2014-02-05 11:51:05.37 Region: Onshore. East flank of Coastal Cordillera. Magnitudes: M_L = 5.5; M_W = 4.8 Kagan angle = 15.7º	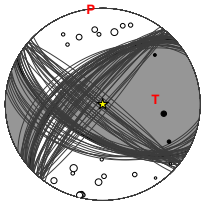	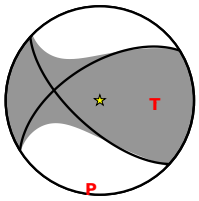
Origin time: 2014-03-17 08:32:37.52 Region: Offshore. Magnitudes: M_L = 5.4; M_W = 5.2 Kagan angle = 23.6º	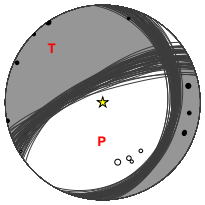	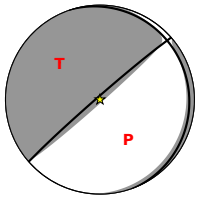
Origin time: 2014-04-05 19:21:44.32 Region: Offshore. Magnitudes: M_L = 4.7; M_W = 4.2 Kagan angle = 21.8º	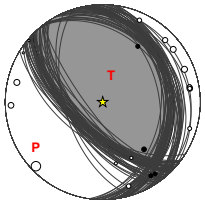	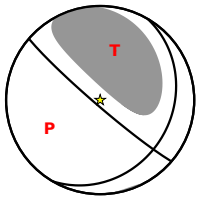
Origin time: 2014-04-09 12:20:10.43 Region: Onshore. Coastal Cordillera. Magnitudes: M_L = 4.5; M_W = 4.1 Kagan angle = 19.3º	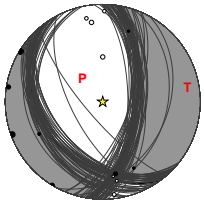	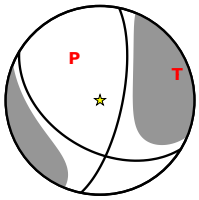

Figure B.17: Comparison between HASH focal mechanisms and BEAT MAP CMTs for seven crustal earthquakes. The HASH solutions show the observed positive (black) and negative (white) P-wave polarities.

B.5 Additional stress inversion data and results

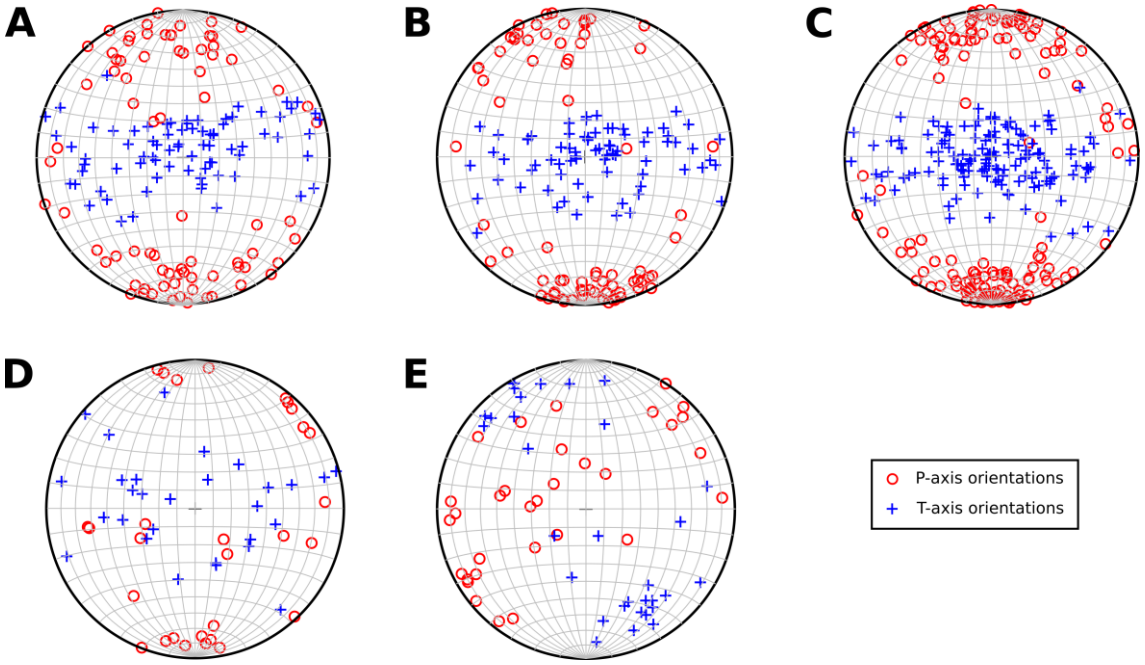

Figure B.18: The stereographic projections show the distribution of P and T axes of the focal mechanisms used as input data for the stress inversion. These data are shown for each of the five inferred stress tensors.

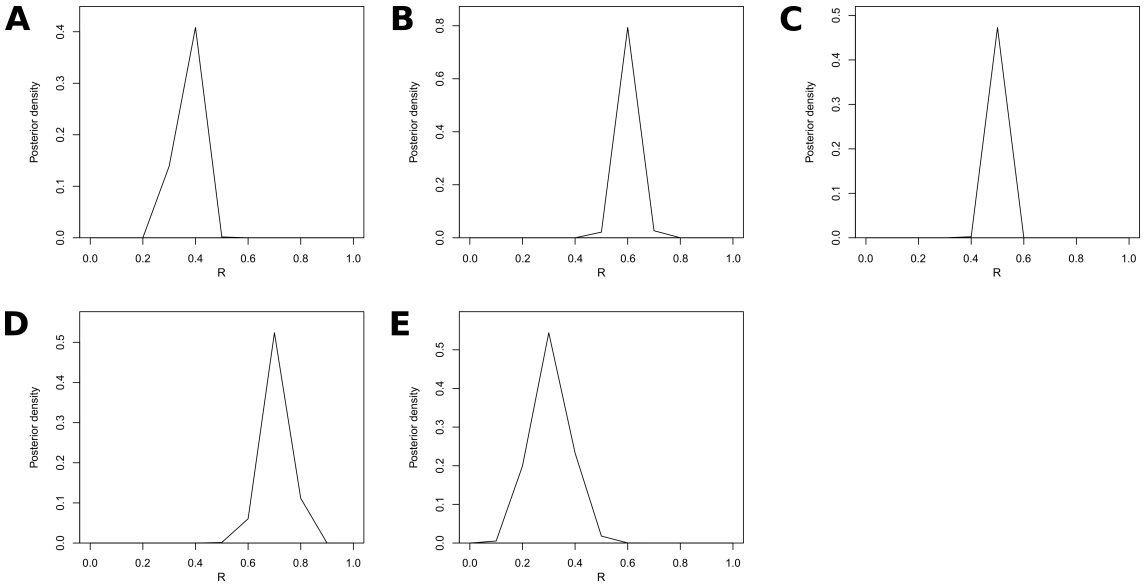

Figure B.19: Stress ratio (R) results of the five stress tensors estimated in the inversion.

Appendix C

Supplement to Chapter 4

This chapter contains supplemental results related to Chapter 4: "Source parameters of the M_W 5.7 Pica crustal earthquake in northern Chile".

Table C.1: Between-event residuals of the Pica mainshock, calculated for each of the three GMMs used in this work.

GMM	PGA res.	SA(0.2) res.	SA(0.5) res.	SA(1.0) res.
BooreEtAl2014	3.14	3.05	1.94	0.64
AkkarEtAlRjb2014	4.36	4.15	2.25	0.88
BindiEtAl2014Rjb	3.37	3.24	1.28	0.64

Table C.2: Subset of parameters associated to the six moment tensor components and the centroid of the Pica mainshock. Bounds of prior distributions, MAP values, and their 95% confidence intervals from the PPDs are given. Values of the GCMT solution are also given. The six CMT components are normalized by and are in the north-east-down (NED) coordinate system. Centroid time and geographic shifts are measured with respect to the NonLinLoc hypocentre. These shifts are not shown for GCMT, since its defined hypocentre is different: 20.26°S, 69.22°W, at 37.7 km depth.

Parameter	Prior bounds	MAP value	95% confidence interval	GCMT solution
M_0 (Nm)	$(3.55 \times 10^{16}, 3.55 \times 10^{19})$	3.92×10^{17}	$(3.85 \times 10^{17}, 4.12 \times 10^{17})$	5.25×10^{17}
M_W	(5.0, 7.0)	5.7	(5.69, 5.71)	5.78
$M_{dd} = M_{rr}$	(-1.41, 1.41)	0.75	(0.72, 0.79)	0.62
$M_{nn} = M_{tt}$	(-1.41, 1.41)	-0.7	(-0.76, -0.61)	-1.08
$M_{ee} = M_{pp}$	(-1.41, 1.41)	0.64	(0.58, 0.68)	0.45
$M_{nd} = M_{rt}$	(-1.0, 1.0)	0.19	(0.18, 0.21)	0.29
$M_{ed} = -M_{rp}$	(-1.0, 1.0)	-0.33	(-0.37, -0.3)	-0.23
$M_{ne} = -M_{tp}$	(-1.0, 1.0)	0.35	(0.33, 0.37)	0.35
Duration (s)	(1, 7)	4.47	(4.13, 4.56)	3.6
Depth (km)	(20, 40)	32.89	(32.71, 33.31)	36.1
North shift (km)	(-15, 15)	-5.97	(-6.22, -5.8)	-
Eart shift (km)	(-15, 15)	-3.26	(-3.94, -2.83)	-
Centroid time (s)	(-5, 5)	-2.56	(-2.67, -2.33)	-

Table C.3: Subset of parameters associated to the geometry and kinematics of the rectangular source model. Bounds of prior distributions, MAP values, and their 95% confidence intervals from the posterior distributions are given.

Parameter	Prior bounds	MAP value	95% confidence interval
Length (km)	(5, 15)	9.16	(5.41, 11.54)
Width (km)	(5, 15)	8.06	(5.63, 10.44)
Average slip (m)	(0.05, 2.0)	0.12	(0.09, 0.21)
Duration (s)	(0.1, 8.0)	1.95	(0.79, 3.08)
Strike (°)	(275, 305)	292.7	(291.1, 293.9)
Dip (°)	(35, 65)	47.8	(46.7, 49.8)
Rake (°)	(135, 165)	153.2	(150.3, 155.2)

Table C.4: Estimated values of Q for the stations considered in the S-wave spectrum analysis.

Station	Q
HMBCX	1613
MNMCX	2001
PATCX	1570
PB01	2453
PB02	1992
PB07	2021
PB08	2034
PSGCX	1536

Table C.5: Estimated values of seismic moment (M_0), magnitude (M_W), corner frequency (f_0), and stress drop ($\Delta\tau$) for the analyzed events in the Pica seismic sequence. Events are labeled based on their origin time.

Earthquake	$\boldsymbol{M_0}$ **(Nm)**	$\boldsymbol{M_W}$	$\boldsymbol{f_0}$ **(Hz)**	$\boldsymbol{\Delta\tau}$ **(MPa)**
20080910161203	3.85×10^{17}	5.65	1.5	255.0
20080910162818	1.76×10^{15}	4.09	5.7	58.2
20080910165400	7.12×10^{13}	3.17	10.2	13.0
20080910180915	2.94×10^{14}	3.58	8.8	34.8
20080910203414	2.62×10^{14}	3.54	7.2	16.7
20080911213651	2.24×10^{14}	3.50	7.5	16.7
20080912065208	3.35×10^{13}	2.95	9.3	46.8
20081003153432	5.33×10^{13}	3.08	13.4	22.4
20090317084311	5.17×10^{14}	3.74	9.7	81.3
20101017232607	1.05×10^{14}	3.28	11.3	25.1

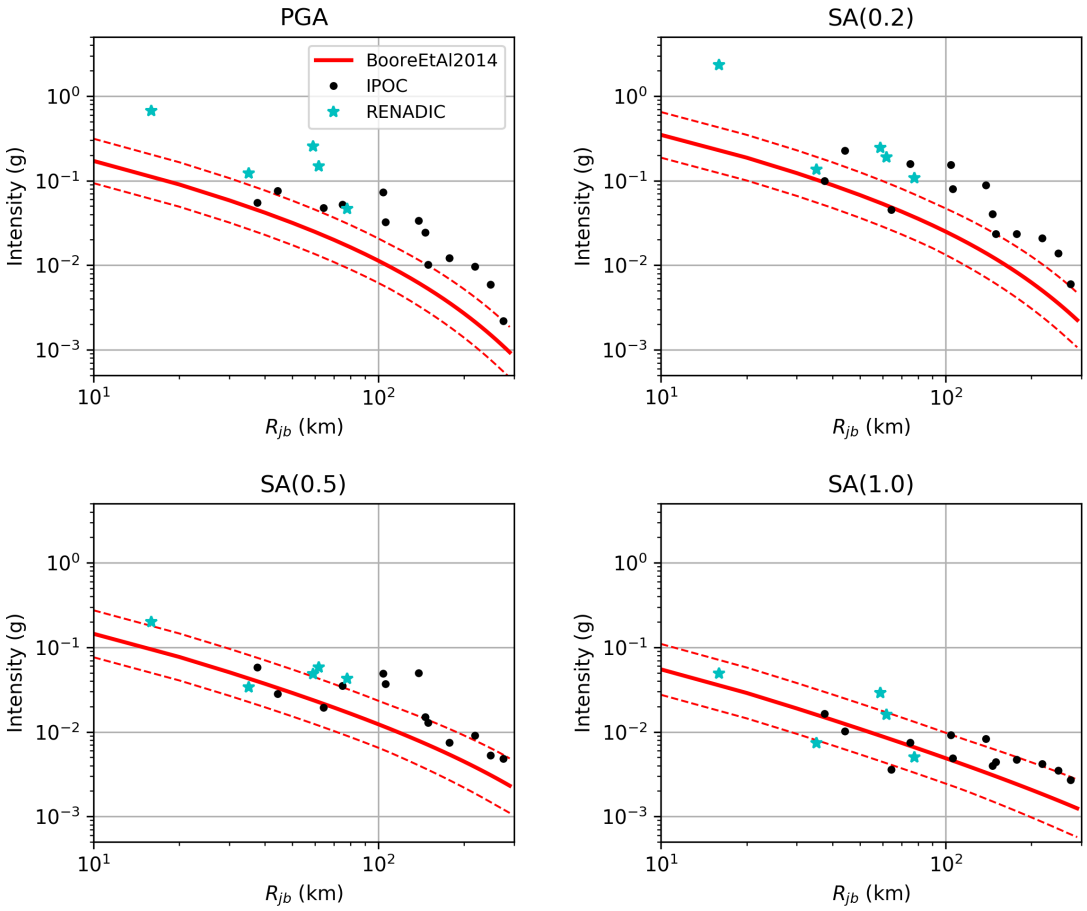

Figure C.1: Comparison between observed and predicted ground motion intensities of the Pica earthquake as a function of distance. Observations are shown with different symbols depending on the seismic network that recorded them. Predictions of the Boore et al. (2014) GMM are shown by the red continuous lines, computed using the average V_{S30} of all stations. Red dashed lines show the GMM standard deviation.

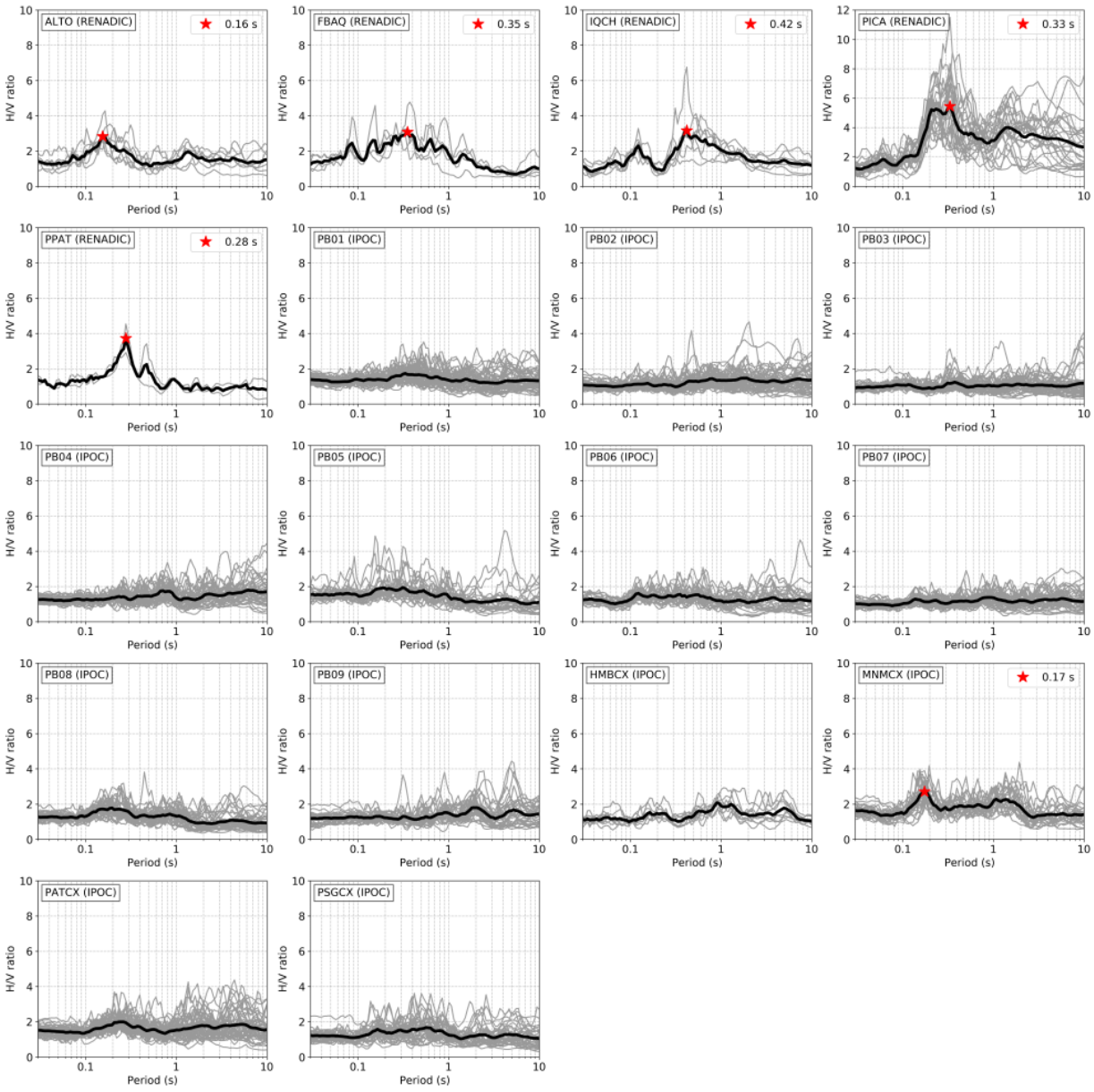

Figure C.2: Earthquake H/V ratios for each station. Each earthquake H/V ratio is shown by grey curves and the average is shown by the thicker black curve. Peaks equal or higher than 2.5 are highlighted with a red star and their period is shown in the legend. Station codes and seismic network (in parenthesis) are given in each plot.

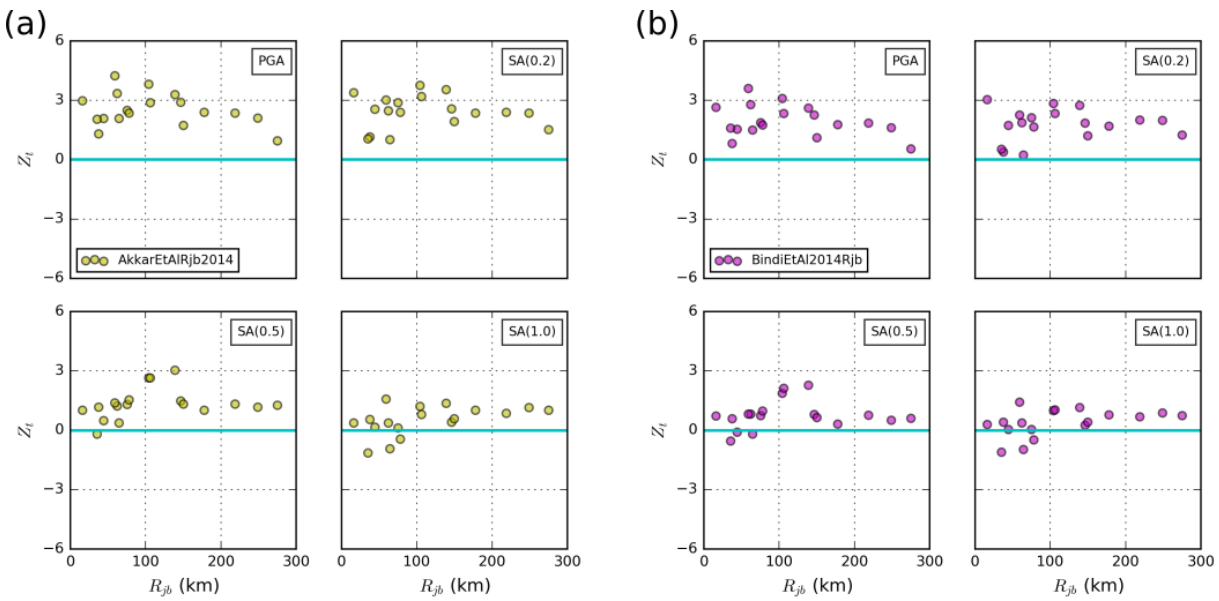

Figure C.3: Total residuals of the Pica mainshock. (a) Residuals calculated with respect to the Akkar et al. (2014) GMM. (b) Residuals calculated with respect to the Bindi et al. (2014) GMM. Legends show the GMM label used in the OpenQuake hazard library (Pagani et al., 2014).

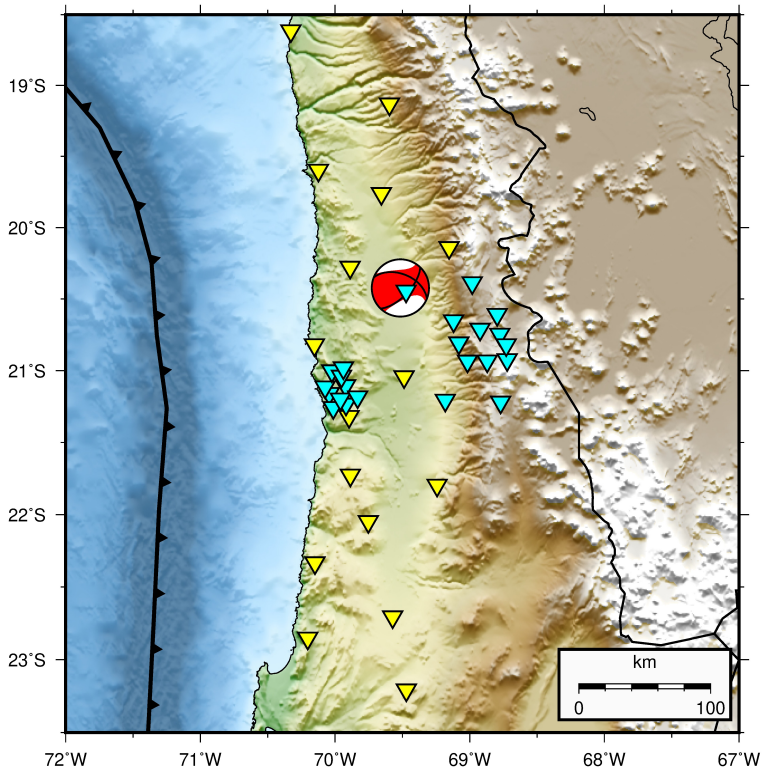

Figure C.4: Stations used to locate the mainshock and aftershocks. Yellow triangles show multiparametric IPOC stations (GFZ and CNRS-INSU, 2006) that include broadband channels. Cyan triangles show short-period stations (Wigger et al., 2016). The mainshock is shown with the MAP CMT estimated in this study.

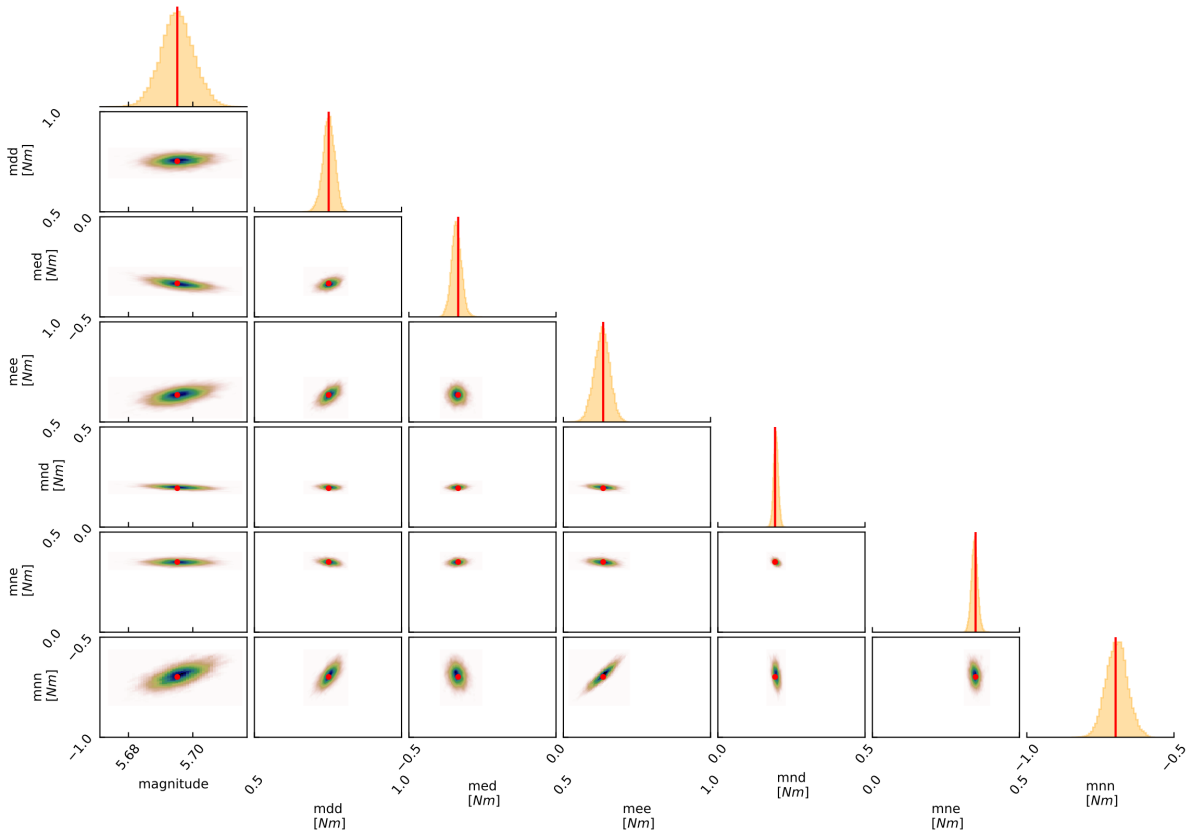

Figure C.5: 1-D and 2-D marginal posteriors of the six moment tensor components and magnitude. The red dot in the 2-D plots and the vertical line in the 1-D plots correspond to the MAP estimates. Blue colors in the 2-D plots show the regions of high probability.

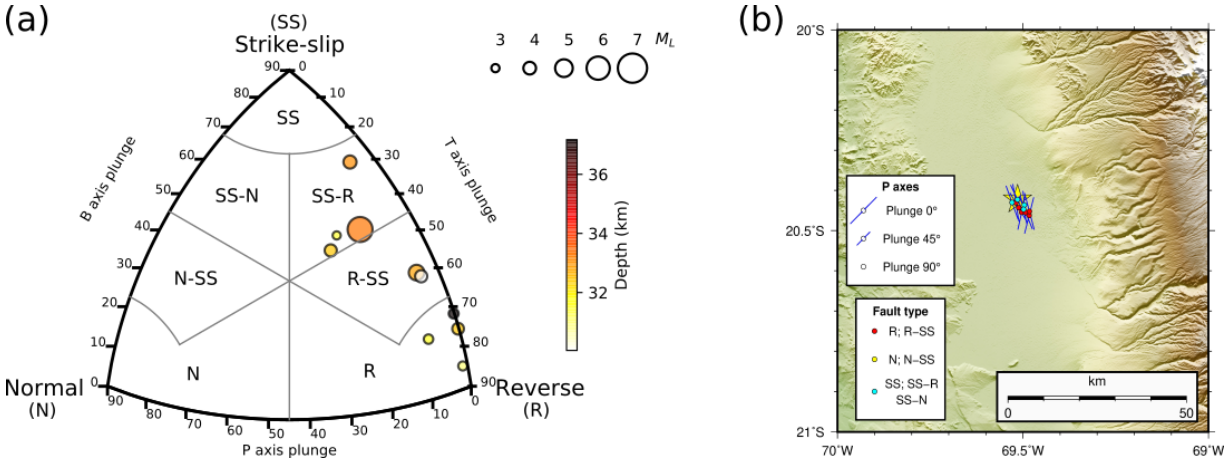

Figure C.6: Style of faulting of the Pica mainshock and its largest aftershocks from focal mechanisms calculated by Herrera et al. (2021). (a) Ternary plot classifying the style of faulting of the events. (b) Map showing pressure (P) axes orientations and the type of faulting. The mainshock is highlighted with a yellow star.

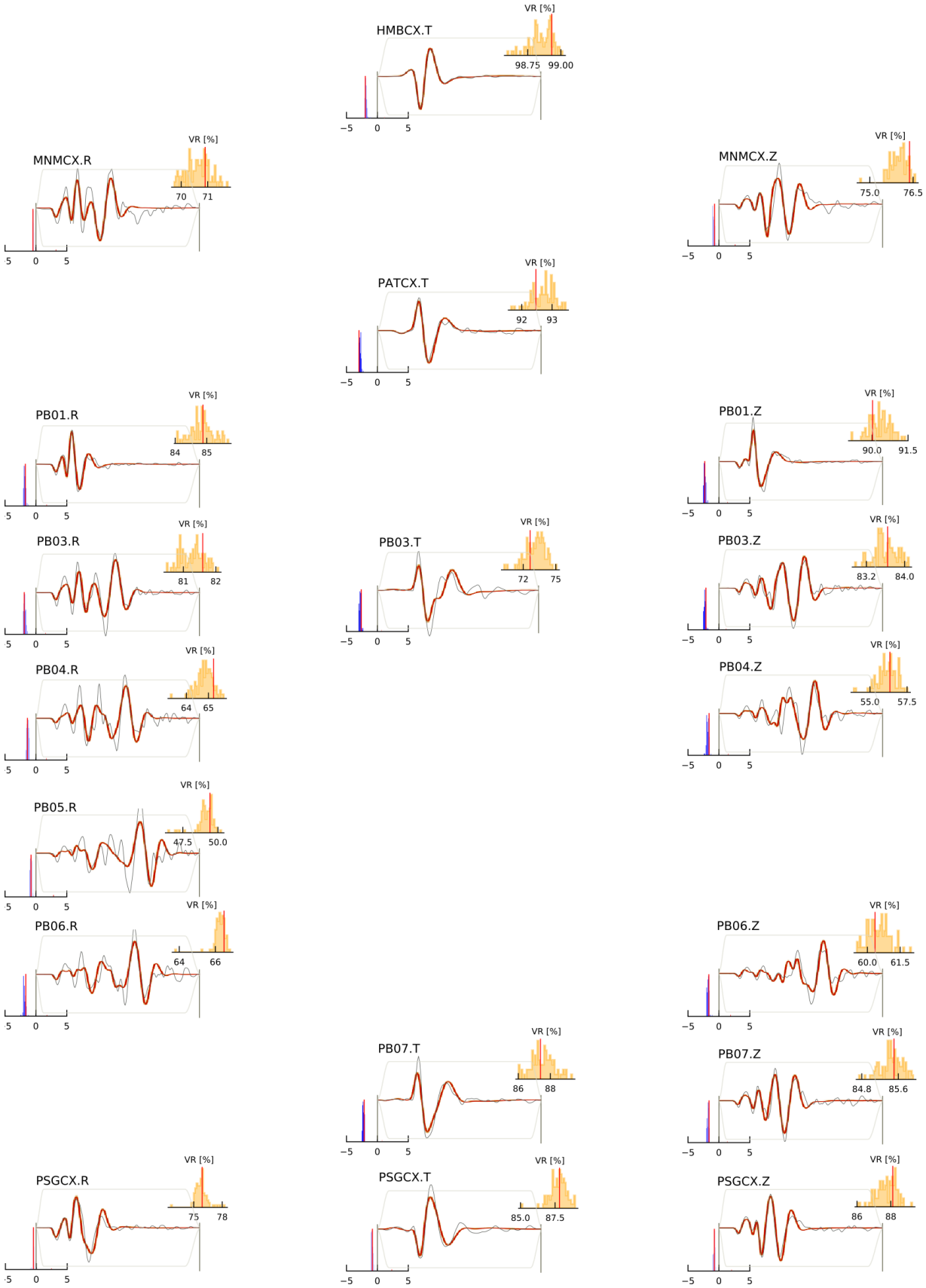

Figure C.7: Observed (grey) and synthetic (red) seismograms of all the stations considered for the CMT source modelling. Elements of each plot are as described in Figure 4.2.

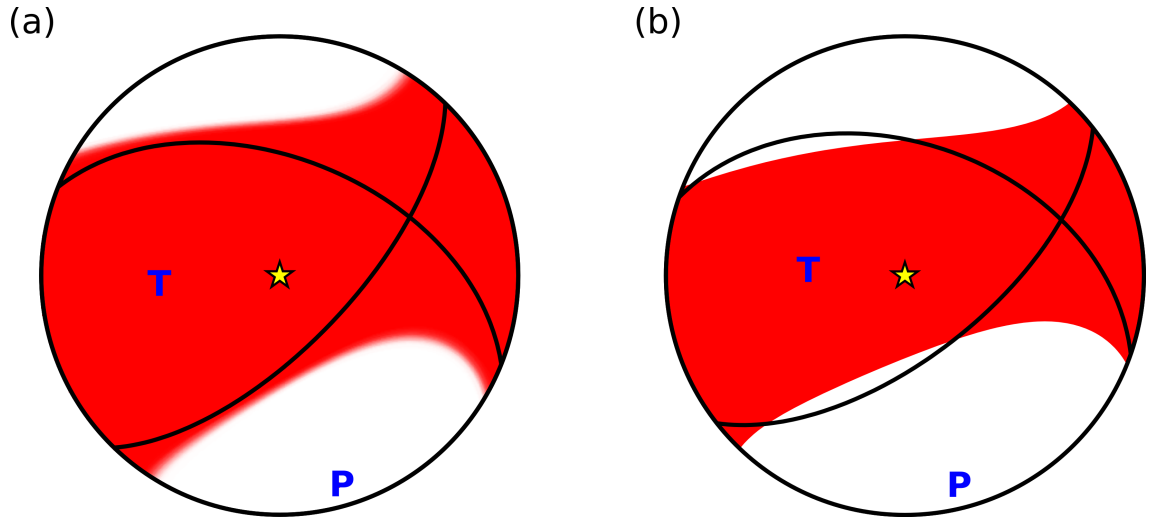

Figure C.8: Comparison of CMT models for the Pica mainshock. Both cases include the associated fault planes of the best solutions and their pressure (P) and tension (T) axes. The centre is shown by the yellow star. (a) Fuzzy CMT estimated in this study, obtained from 100 CMT solutions drawn from the PPD. (b) Best CMT solution reported by the GCMT catalogue.

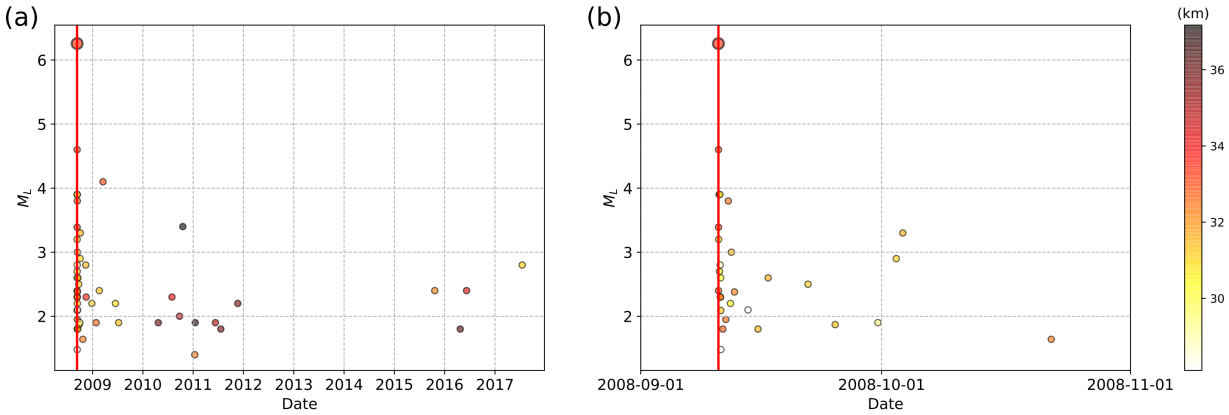

Figure C.9: Temporal distribution of the Pica seismic sequence relocated in this work. The mainshock is shown with a larger circle and a red line. Local magnitudes are reported by Sippl et al. (2018). (a) Earthquakes near the rupture area until 2017. (b) Earthquake sequence during its first two months.

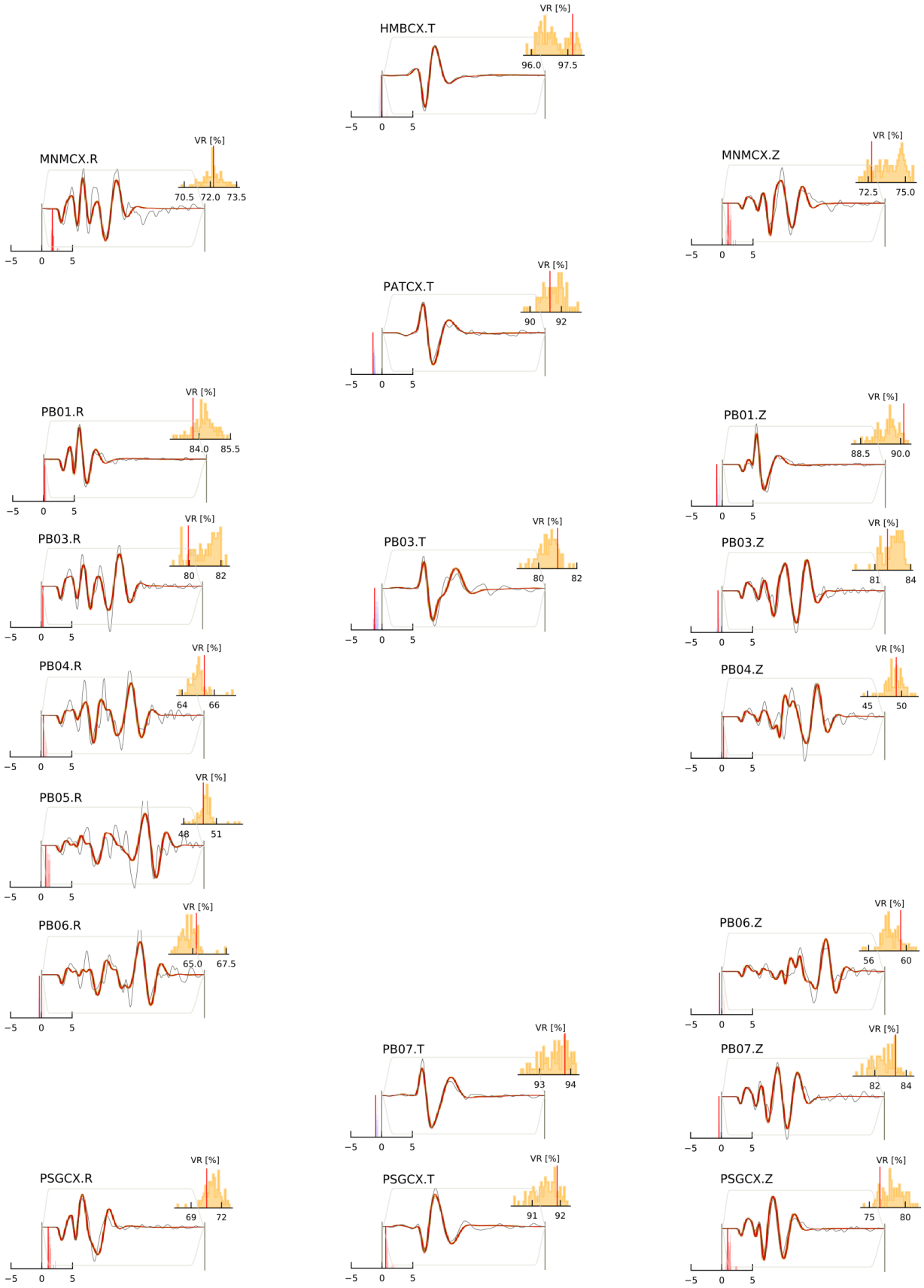

Figure C.10: Observed (grey) and synthetic (red) seismograms of the stations considered for the rectangular source modelling. The shading around the red seismograms is composed of 100 random synthetic seismograms drawn from the PPD. VR and station time shifts (s) histograms from these ensembles are also shown in each plot.

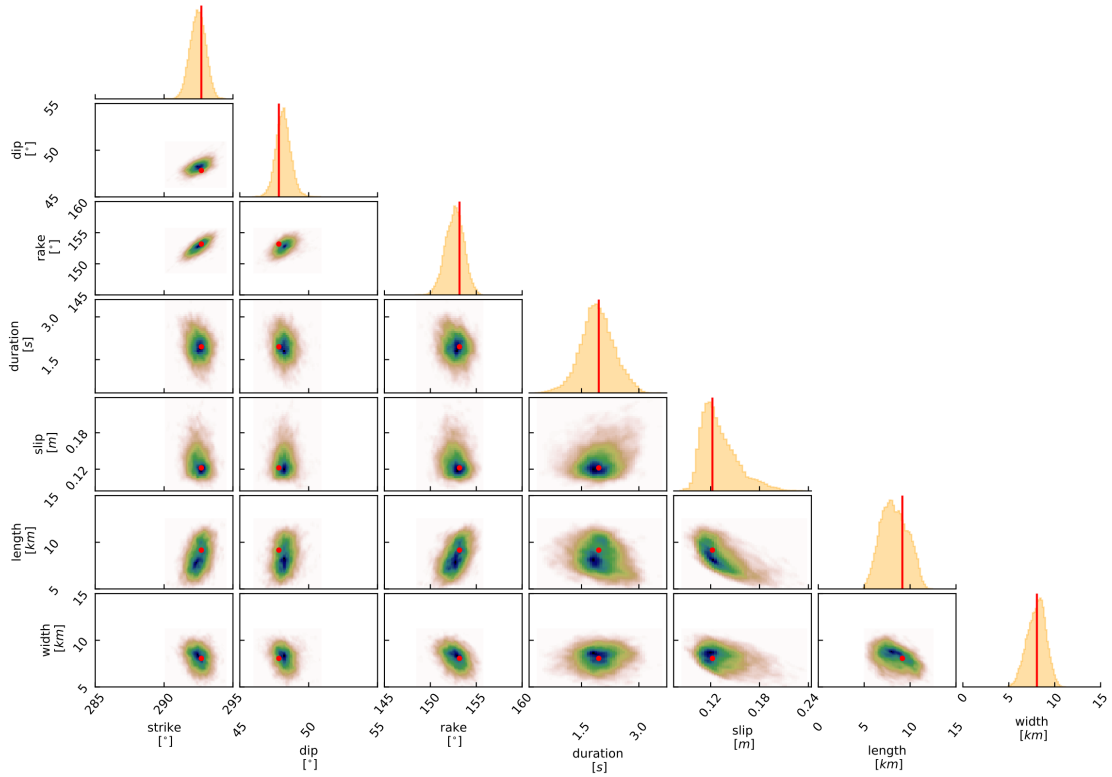

Figure C.11: 1-D and 2-D marginal posteriors of a subset of the parameters that describe the geometry and kinematics of the rectangular source model. The red dot in the 2-D plots and the vertical line in the 1-D plots correspond to the MAP estimates. Blue colors in the 2-D plots show the regions of high probability.

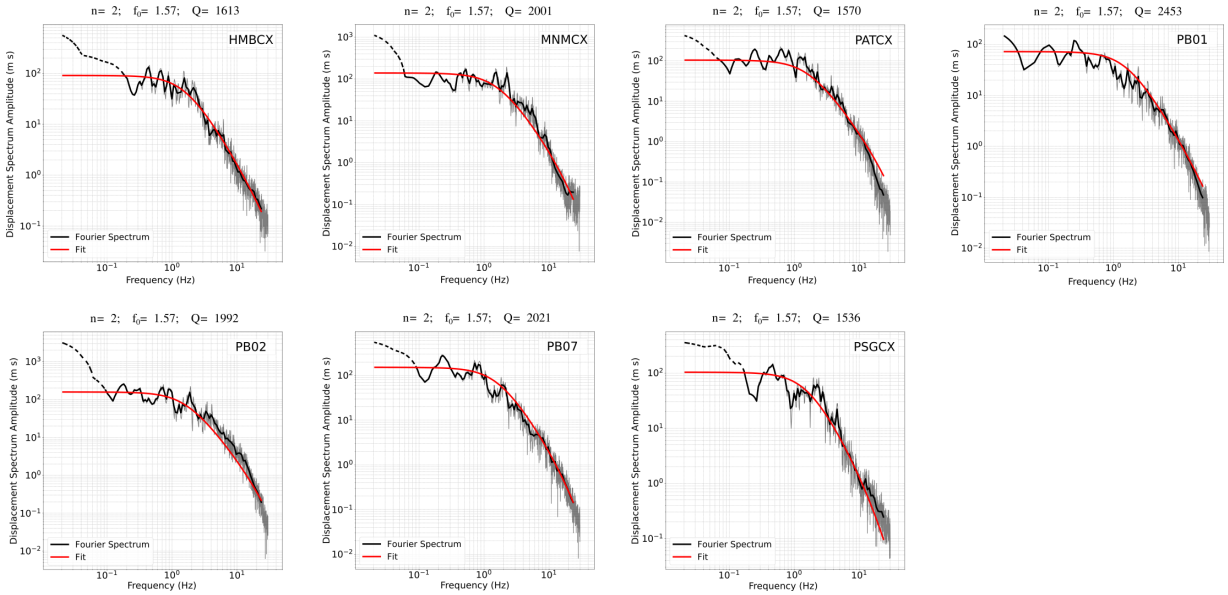

Figure C.12: Displacement spectrum modelling of the Pica mainshock. The observed spectrum with Konno-Ohmachi smoothing is shown in black, the non-smoothed spectrum is shown in grey, and the modelled spectrum is shown in red. The estimated values of f_0 and Q are also given for each station.

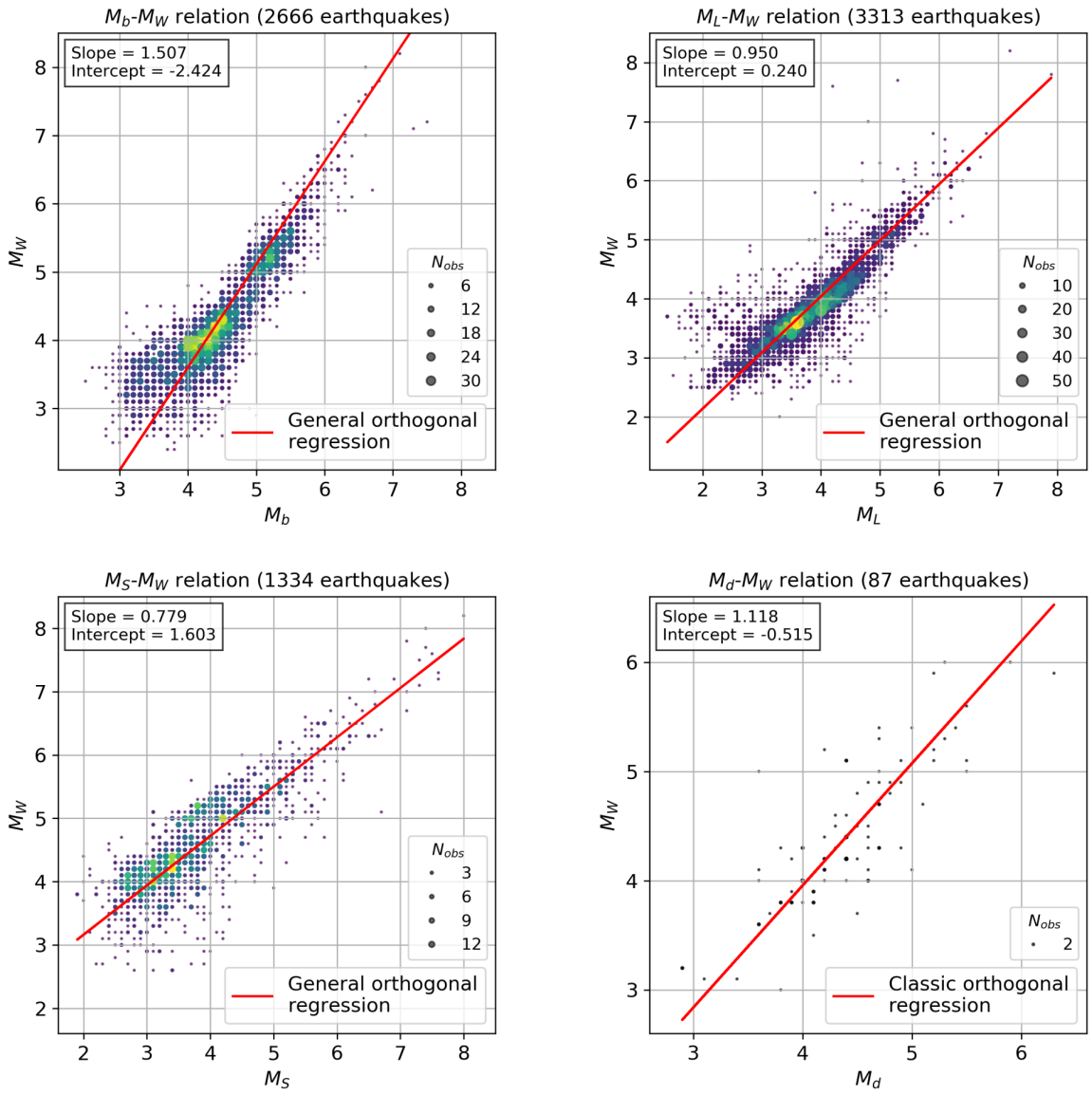

Figure C.13: Conversion relations between four magnitude types and M_W for northern Chile. Each dot represents a magnitude pair, and the dot size is proportional to the number of observations (N_{obs}) of a pair. Larger dots are also colored with warmer colors for easy identification. The magnitude data were obtained from the event catalogue of the reviewed ISC bulletin (International Seismological Centre, 2021b) within the study region.

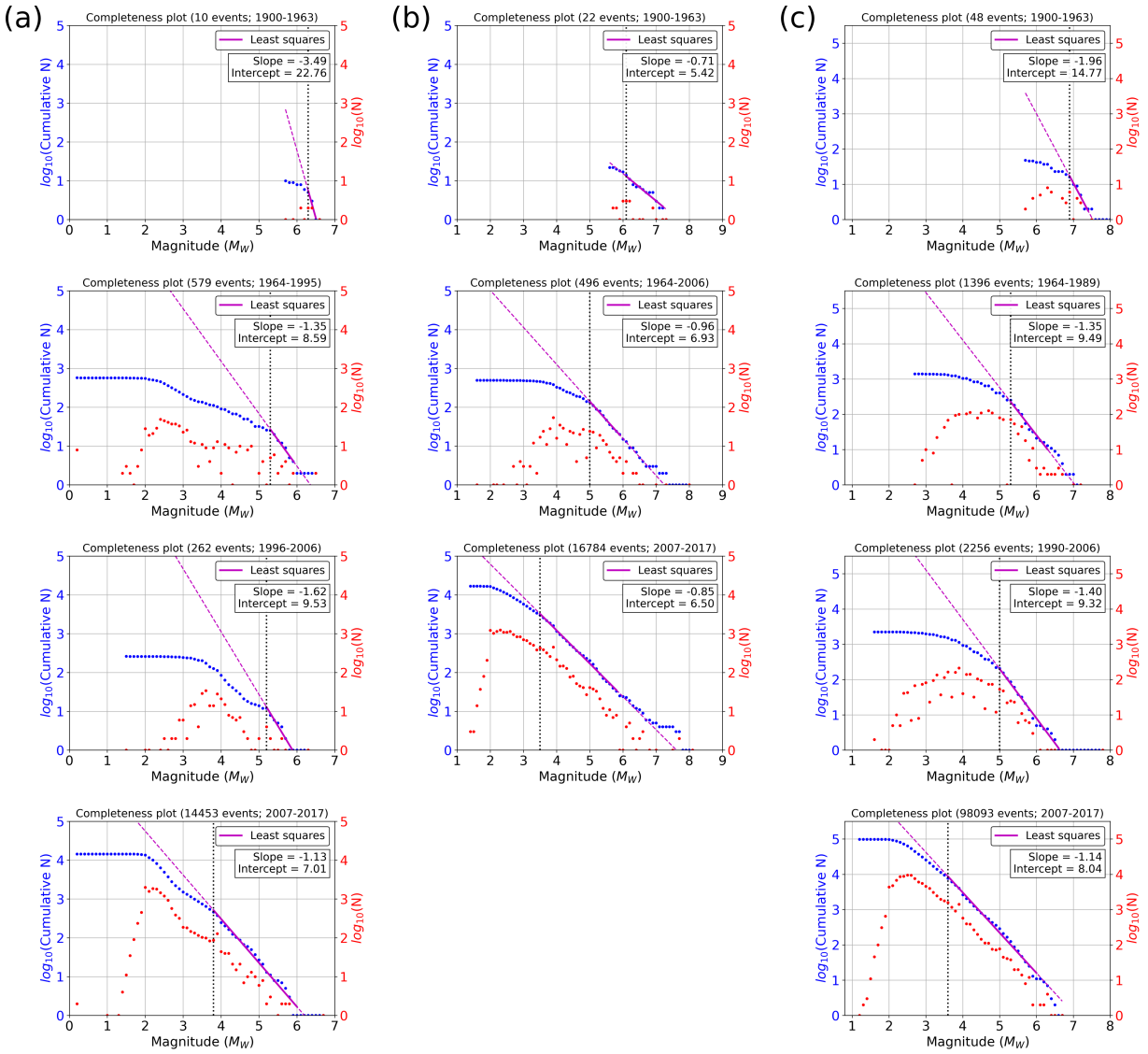

Figure C.14: Completeness analysis. Temporal intervals were defined between 1900 and 2017 for (a) crustal earthquakes, (b) interplate earthquakes, and (c) intraplate earthquakes. The magnitude of completeness chosen for each interval is shown by the black dotted line. Linear fits (solid purple lines) were performed to the cumulative number of earthquakes per $\Delta M_W = 0.1$ (blue samples), and dashed purple lines are extrapolated extensions outside the fit range. The number of earthquakes per $\Delta M_W = 0.1$ are also shown by the red samples for visual reference.

Bibliography

Abercrombie, R. E. (1995). Earthquake source scaling relationships from- 1 to 5 Ml using seismograms recorded at 2.5-km depth. *Journal of Geophysical Research: Solid Earth*, 100(B12):24015–24036. DOI: https://doi.org/10.1029/95JB02397.

Abrahamson, N., Gregor, N., and Addo, K. (2016). BC Hydro ground motion prediction equations for subduction earthquakes. *Earthquake Spectra*, 32(1):23–44. DOI: https://doi.org/10.1193/051712EQS188MR.

Abrahamson, N., Kuehn, N., Gulerce, Z., Gregor, N., Bozognia, Y., Parker, G., Stewart, J., Chiou, B., Idriss, I. M., Campbell, K., and Youngs, R. (2018). Update of the BC Hydro subduction ground-motion model using the NGA-subduction dataset. *Pacific Earthquake Engineering Research Center*, Technical Report PEER 2018/02.

Abrahamson, N. A. and Youngs, R. R. (1992). A stable algorithm for regression analyses using the random effects model. *Bulletin of the Seismological Society of America*, 82(1):505–510.

Akkar, S., Sandıkkaya, M. A., and Bommer, J. J. (2014). Empirical ground-motion models for point-and extended-source crustal earthquake scenarios in Europe and the Middle East. *Bulletin of earthquake engineering*, 12(1):359–387. DOI: https://doi.org/10.1007/s10518-013-9461-4.

Allmann, B. P. and Shearer, P. M. (2007). Spatial and temporal stress drop variations in small earthquakes near Parkfield, California. *Journal of Geophysical Research: Solid Earth*, 112(B4). DOI: https://doi.org/10.1029/2006JB004395.

Allmendinger, R. W. and González, G. (2010). Invited review paper: Neogene to Quaternary tectonics of the coastal Cordillera, northern Chile. *Tectonophysics*, 495(1-2):93–110. DOI: https://doi.org/10.1016/j.tecto.2009.04.019.

Allmendinger, R. W., González, G., Yu, J., Hoke, G., and Isacks, B. (2005a). Trench-parallel shortening in the Northern Chilean Forearc: Tectonic and climatic implications. *Geological Society of America Bulletin*, 117(1-2):89–104. DOI: https://doi.org/10.1130/B25505.1.

Allmendinger, R. W., Reilinger, R., and Loveless, J. (2007). Strain and rotation rate from GPS in Tibet, Anatolia, and the Altiplano. *Tectonics*, 26(3). DOI: https://doi.org/10.1029/2006TC002030.

Allmendinger, R. W., Smalley Jr, R., Bevis, M., Caprio, H., and Brooks, B. (2005b). Bending the bolivian orocline in real time. *Geology*, 33(11):905–908. DOI: https://doi.org/10.1130/G21779.1.

Alvarado, P., Barrientos, S., Saez, M., Astroza, M., and Beck, S. (2009). Source study and tectonic implications of the historic 1958 Las Melosas crustal earthquake, Chile, compared to earthquake damage. *Physics of the Earth and Planetary Interiors*, 175(1-2):26–36. DOI: https://doi.org/10.1016/j.pepi.2008.03.015.

Álvarez-Gómez, J. A. (2014). FMC: a one-liner Python program to manage, classify and plot focal mechanisms. In *EGU General Assembly Conference Abstracts*, page 10887.

Arnold, R. and Townend, J. (2007). A Bayesian approach to estimating tectonic stress from seismological data. *Geophysical Journal International*, 170(3):1336–1356. DOI: https://doi.org/10.1111/j.1365-246X.2007.03485.x.

Asch, G., Tilmann, F., Heit, B., and Schurr, B. (2014). HART-PISAGUA Project Chile. *GFZ Data Services. Other/Seismic Network*. DOI: https://doi.org/10.14470/8Q7569558037.

ASL/USGS (1988). Global Seismograph Network - IRIS/USGS [Data set]. *International Federation of Digital Seismograph Networks*. DOI: https://doi.org/10.7914/SN/IU.

Atik, L. A., Abrahamson, N., Bommer, J. J., Scherbaum, F., Cotton, F., and Kuehn, N. (2010). The variability of ground-motion prediction models and its components. *Seismological Research Letters*, 81(5):794–801. DOI: https://doi.org/10.1785/gssrl.81.5.794.

Atkinson, G. M. and Boore, D. M. (2003). Empirical ground-motion relations for subduction-zone earthquakes and their application to Cascadia and other regions. *Bulletin of the Seismological Society of America*, 93(4):1703–1729. DOI: https://doi.org/10.1785/0120020156.

Atkinson, G. M. and Boore, D. M. (2008). Erratum to empirical ground-motion relations for subduction zone earthquakes and their application to Cascadia and other regions. *Bulletin of the Seismological Society of America*, 98(5):2567–2569. DOI: https://doi.org/10.1785/0120080108.

Balfour, N., Cassidy, J., Dosso, S., and Mazzotti, S. (2011). Mapping crustal stress and strain in southwest British Columbia. *Journal of Geophysical Research: Solid Earth*, 116(B3). DOI: https://doi.org/10.1029/2010JB008003.

Bastías, N. and Montalva, G. A. (2016). Chile strong ground motion flatfile. *Earthquake Spectra*, 32(4):2549–2566. DOI: https://doi.org/10.1193/102715EQS158DP.

Bastías, N., Montalva, G. A., Leyton, F., Saez, E., Ruz, F., and Troncoso, P. (2015). Evaluation of ground motion prediction equations (GMPEs) for Chile subduction zone. *15th Pan-American Conference on Soil Mechanics and Geotechnical Engineering*, Buenos Aires, Argentina, 15-18 November.

Béjar-Pizarro, M., Carrizo, D., Socquet, A., Armijo, R., Barrientos, S., Bondoux, F., Bonvalot, S., Campos, J., Comte, D., De Chabalier, J., et al. (2010). Asperities and barriers on the seismogenic zone in North Chile: state-of-the-art after the 2007 Mw 7.7 Tocopilla earthquake inferred by GPS and InSAR data. *Geophysical Journal International*, 183(1):390–406. DOI: https://doi.org/10.1111/j.1365-246X.2010.04748.x.

Bevis, M., Kendrick, E., Smalley Jr, R., Brooks, B., Allmendinger, R., and Isacks, B. (2001). On the strength of interplate coupling and the rate of back arc convergence in the central Andes: An analysis of the interseismic velocity field. *Geochemistry, Geophysics, Geosystems*, 2(11). DOI: https://doi.org/10.1029/2001GC000198.

Beyreuther, M., Barsch, R., Krischer, L., Megies, T., Behr, Y., and Wassermann, J. (2010). ObsPy: A Python toolbox for seismology. *Seismological Research Letters*, 81(3):530–533. DOI: https://doi.org/10.1785/gssrl.81.3.530.

Bindi, D., Massa, M., Luzi, L., Ameri, G., Pacor, F., Puglia, R., and Augliera, P. (2014). Pan-European ground-motion prediction equations for the average horizontal component of PGA, PGV, and 5%-damped PSA at spectral periods up to 3.0 s using the RESORCE dataset. *Bulletin of Earthquake Engineering*, 12(1):391–430. DOI: https://doi.org/10.1007/s10518-013-9525-5.

Bird, P. (2003). An updated digital model of plate boundaries. *Geochemistry, Geophysics, Geosystems*, 4(3). DOI: https://doi.org/10.1029/2001GC000252.

Bloch, W., Kummerow, J., Salazar, P., Wigger, P., and Shapiro, S. (2014). High-resolution image of the North Chilean subduction zone: seismicity, reflectivity and fluids. *Geophysical Journal International*, 197(3):1744–1749. DOI: https://doi.org/10.1093/gji/ggu084.

Bloch, W., Schurr, B., Kummerow, J., Salazar, P., and Shapiro, S. A. (2018). From slab coupling to slab pull: Stress segmentation in the subducting Nazca plate. *Geophysical Research Letters*, 45(11):5407–5416. DOI: https://doi.org/10.1029/2018GL078793.

Boore, D. M., Stewart, J. P., Seyhan, E., and Atkinson, G. M. (2014). NGA-West2 equations for predicting PGA, PGV, and 5% damped PSA for shallow crustal earthquakes. *Earthquake Spectra*, 30(3):1057–1085. DOI: https://doi.org/10.1193/070113EQS184M.

Boutelier, D., Oncken, O., and Cruden, A. (2014). Trench-parallel shortening in the forearc caused by subduction along a seaward-concave plate boundary: Insights from analogue modelling experiments. *Tectonophysics*, 611:192–203. DOI: https://doi.org/10.1016/j.tecto.2013.11.028.

Boyd, O. S., McNamara, D. E., Hartzell, S., and Choy, G. (2017). Influence of lithostatic stress on earthquake stress drops in North America. *Bulletin of the Seismological Society of America*, 107(2):856–868. DOI: https://doi.org/10.1785/0120160219.

Brune, J. N. (1970). Tectonic stress and the spectra of seismic shear waves from earthquakes. *Journal of geophysical research*, 75(26):4997–5009. DOI: https://doi.org/10.1029/JB075i026p04997.

Cabrera, L., Ruiz, S., Poli, P., Contreras-Reyes, E., Osses, A., and Mancini, R. (2021). Northern Chile intermediate-depth earthquakes controlled by plate hydration. *Geophysical Journal International*, 226(1):78–90. DOI: https://doi.org/10.1093/gji/ggaa565.

Cembrano, J., Lavenu, A., Yañez, G., Riquelme, R., García, M., González, G., and Hérail, G. (2007). Neotectonics. *In T. Moreno, and W. Gibbons (Eds.), The geology of Chile*, pages 231–261. DOI: https://doi.org/10.1144/GOCH.

Cesca, S., Sobiesiak, M., Tassara, A., Olcay, M., Günther, E., Mikulla, S., and Dahm, T. (2009). The Iquique Local Network and PicArray. *GFZ Data Services*. DOI: https://doi.org/10.14470/VD070092.

Chlieh, M., De Chabalier, J., Ruegg, J., Armijo, R., Dmowska, R., Campos, J., and Feigl, K. (2004). Crustal deformation and fault slip during the seismic cycle in the North Chile subduction zone, from GPS and InSAR observations. *Geophysical Journal International*, 158(2):695–711. DOI: https://doi.org/10.1111/j.1365-246X.2004.02326.x.

Contreras, V. and Boroschek, R. (2012). Strong ground motion attenuation relations for Chilean subduction zone interface earthquakes. *15th World Conference on Earthquake Engineering*, Lisbon, Portugal, 24-28 September.

Del Moral, P., Doucet, A., and Jasra, A. (2006). Sequential monte carlo samplers. *Journal of the Royal Statistical Society: Series B (Statistical Methodology)*, 68(3):411–436. DOI: https://doi.org/10.1111/j.1467-9868.2006.00553.x.

Delouis, B., Cisternas, A., Dorbath, L., Rivera, L., and Kausel, E. (1996). The Andean subduction zone between 22 and 25°S (northern Chile): Precise geometry and state of stress. *Tectonophysics*, 259(1-3):81–100. DOI: https://doi.org/10.1016/0040-1951(95)00065-8.

Delouis, B., Nocquet, J.-M., and Vallée, M. (2010). Slip distribution of the February 27, 2010 Mw=8.8 Maule earthquake, central Chile, from static and high-rate GPS, InSAR, and broadband teleseismic data. *Geophysical Research Letters*, 37(17). DOI: https://doi.org/10.1029/2010GL043899.

Dziewonski, A. M., Chou, T.-A., and Woodhouse, J. H. (1981). Determination of earthquake source parameters from waveform data for studies of global and regional seismicity. *Journal of Geophysical Research: Solid Earth*, 86(B4):2825–2852. DOI: https://doi.org/10.1029/JB086iB04p02825.

Ekström, G., Nettles, M., and Dziewoński, A. (2012). The global CMT project 2004–2010: Centroid-moment tensors for 13,017 earthquakes. *Physics of the Earth and Planetary Interiors*, 200:1–9. DOI: https://doi.org/10.1016/j.pepi.2012.04.002.

Eshelby, J. D. (1957). The determination of the elastic field of an ellipsoidal inclusion, and related problems. *Proceedings of the royal society of London. Series A. Mathematical and physical sciences*, 241(1226):376–396. DOI: https://doi.org/10.1098/rspa.1957.0133.

Farías, M., Charrier, R., Comte, D., Martinod, J., and Hérail, G. (2005). Late cenozoic deformation and uplift of the western flank of the Altiplano: Evidence from the depositional, tectonic, and geomorphologic evolution and shallow seismic activity (northern Chile at 19°30'S). *Tectonics*, 24(4). DOI: https://doi.org/10.1029/2004TC001667.

Farías, M., Comte, D., Roecker, S., Carrizo, D., and Pardo, M. (2011). Crustal extensional faulting triggered by the 2010 Chilean earthquake: The Pichilemu seismic sequence. *Tectonics*, 30(6). DOI: https://doi.org/10.1029/2011TC002888.

Folesky, J., Kummerow, J., and Shapiro, S. A. (2021). Stress drop variations in the region of the 2014 Mw 8.1 Iquique earthquake, northern Chile. *Journal of Geophysical Research: Solid Earth*, 126(4):e2020JB020112. DOI: https://doi.org/10.1029/2020JB020112.

GEOFON Data Centre (1993). GEOFON Seismic Network. *Deutsches GeoForschungsZentrum GFZ*. DOI: https://doi.org/10.14470/TR560404.

Gephart, J. W. (1994). Topography and subduction geometry in the central andes: Clues to the mechanics of a noncollisional orogen. *Journal of Geophysical Research: Solid Earth*, 99(B6):12279–12288. DOI: https://doi.org/10.1029/94JB00129.

GFZ and CNRS-INSU (2006). IPOC Seismic Network. *Integrated Plate Boundary Observatory Chile - IPOC*. DOI: https://doi.org/10.14470/PK615318.

González, G., Cembrano, J., Carrizo, D., Macci, A., and Schneider, H. (2003). The link between forearc tectonics and Pliocene–Quaternary deformation of the Coastal Cordillera, northern Chile. *Journal of South American Earth Sciences*, 16(5):321–342. DOI: https://doi.org/10.1016/S0895-9811(03)00100-7.

González, G., Pasten-Araya, F., Victor, P., González, Y., Valenzuela, J., and Shrivastava, M. (2021). The role of interplate locking on the seismic reactivation of upper plate faults on the subduction margin of northern Chile. *Scientific reports*, 11(1):1–12. DOI: https://doi.org/10.1038/s41598-021-00875-6.

González, G., Salazar, P., Loveless, J. P., Allmendinger, R. W., Aron, F., and Shrivastava, M. (2015). Upper plate reverse fault reactivation and the unclamping of the megathrust during the 2014 northern Chile earthquake sequence. *Geology*, 43(8):671–674. DOI: https://doi.org/10.1130/G36703.1.

Graeber, F. M. and Asch, G. (1999). Three-dimensional models of P wave velocity and P-to-S velocity ratio in the southern central Andes by simultaneous inversion of local earthquake data. *Journal of Geophysical Research: Solid Earth*, 104(B9):20237–20256. DOI: https://doi.org/10.1029/1999JB900037.

Gutenberg, B. and Richter, C. F. (1944). Frequency of earthquakes in California. *Bulletin of the Seismological society of America*, 34(4):185–188.

Hanks, T. C. (1979). b values and $\omega^{-\gamma}$ seismic source models: Implications for tectonic stress variations along active crustal fault zones and the estimation of high-frequency strong ground motion. *Journal of Geophysical Research: Solid Earth*, 84(B5):2235–2242. DOI: https://doi.org/10.1029/JB084iB05p02235.

Hardebeck, J. L. and Shearer, P. M. (2002). A new method for determining first-motion focal mechanisms. *Bulletin of the Seismological Society of America*, 92(6):2264–2276. DOI: https://doi.org/10.1785/0120010200.

Hardebeck, J. L. and Shearer, P. M. (2003). Using S/P amplitude ratios to constrain the focal mechanisms of small earthquakes. *Bulletin of the Seismological Society of America*, 93(6):2434–2444. DOI: https://doi.org/10.1785/0120020236.

Hayes, G. P., Moore, G. L., Portner, D. E., Hearne, M., Flamme, H., Furtney, M., and Smoczyk, G. M. (2018). Slab2, a comprehensive subduction zone geometry model. *Science*, 362(6410):58–61. DOI: https://doi.org/10.1126/science.aat4723.

Heimann, S., Kriegerowski, M., Isken, M., Cesca, S., Daout, S., Grigoli, F., Juretzek, C., Megies, T., Nooshiri, N., Steinberg, A., et al. (2017). Pyrocko-An open-source seismology toolbox and library. *Potsdam: GFZ Data Services*. DOI: https://doi.org/10.5880/GFZ.2.1.2017.001.

Heimann, S., Vasyura-Bathke, H., Sudhaus, H., Isken, M. P., Kriegerowski, M., Steinberg, A., and Dahm, T. (2019). A Python framework for efficient use of pre-computed Green's functions in seismological and other physical forward and inverse source problems. *Solid Earth*, 10(6):1921–1935. DOI: https://doi.org/10.5194/se-10-1921-2019.

Herrera, C., Cassidy, J. F., Dosso, S. E., Bastías, N., and Onur, T. (2020). Ground-motion evaluation of moderate and large interface earthquakes along the Chilean subduction zone. *Bulletin of the Seismological Society of America*, 110(6):2693–2710. DOI: https://doi.org/10.1785/0120190265.

Herrera, C., Cassidy, J. F., Dosso, S. E., Dettmer, J., Bloch, W., Sippl, C., and Salazar, P. (2021). The crustal stress field inferred from focal mechanisms in northern Chile. *Geophysical Research Letters*, 48(8):e2021GL092889. DOI: https://doi.org/10.1029/2021GL092889.

Herrera, C., Ruiz, S., Madariaga, R., and Poli, P. (2017). Dynamic inversion of the 2015 Jujuy earthquake and similarity with other intraslab events. *Geophysical Journal International*, 209(2):866–875. DOI: https://doi.org/10.1093/gji/ggx056.

Hetland, E. and Simons, M. (2010). Post-seismic and interseismic fault creep II: Transient creep and interseismic stress shadows on megathrusts. *Geophysical Journal International*, 181(1):99–112. DOI: https://doi.org/10.1111/j.1365-246X.2009.04482.x.

Husen, S., Kissling, E., Flueh, E., and Asch, G. (1999). Accurate hypocentre determination in the seismogenic zone of the subducting Nazca Plate in northern Chile using a combined on-/offshore network. *Geophysical Journal International*, 138(3):687–701. DOI: https://doi.org/10.1046/j.1365-246x.1999.00893.x.

Hutton, L. and Boore, D. M. (1987). The M_L scale in southern California. *Bulletin of the Seismological Society of America*, 77(6):2074–2094. DOI: https://doi.org/10.1785/BSSA0770062074.

Idini, B., Rojas, F., Ruiz, S., and Pastén, C. (2017). Ground motion prediction equations for the Chilean subduction zone. *Bulletin of Earthquake Engineering*, 15(5):1853–1880. DOI: https://doi.org/10.1007/s10518-016-0050-1.

International Seismological Centre (2021a). ISC-GEM Earthquake Catalogue. *ISC products*. DOI: https://doi.org/10.31905/d808b825.

International Seismological Centre (2021b). On-line Bulletin. *ISC products*. DOI: https://doi.org/10.31905/D808B830.

Johnson, S. Y., Blakely, R. J., Stephenson, W. J., Dadisman, S. V., and Fisher, M. A. (2004). Active shortening of the Cascadia forearc and implications for seismic hazards of the Puget Lowland. *Tectonics*, 23(1). DOI: https://doi.org/10.1029/2003TC001507.

Kagan, Y. (1991). 3-D rotation of double-couple earthquake sources. *Geophysical Journal International*, 106(3):709–716. DOI: https://doi.org/10.1111/j.1365-246X.1991.tb06343.x.

Kaplan, H., Bilgin, H., Yilmaz, S., Binici, H., and Öztas, A. (2010). Structural damages of L'Aquila (Italy) earthquake. *Natural Hazards and Earth System Sciences*, 10(3):499–507. DOI: https://doi.org/10.5194/nhess-10-499-2010.

Kausel, E. and Campos, J. (1992). The Ms=8 tensional earthquake of 9 December 1950 of northern Chile and its relation to the seismic potential of the region. *Physics of the earth and planetary interiors*, 72(3-4):220–235. DOI: https://doi.org/10.1016/0031-9201(92)90203-8.

Kaverina, A., Lander, A., and Prozorov, A. (1996). Global creepex distribution and its relation to earthquake-source geometry and tectonic origin. *Geophysical Journal International*, 125(1):249–265. DOI: https://doi.org/10.1111/j.1365-246X.1996.tb06549.x.

Kayen, R., Carkin, B. D., Corbet, S., Pinilla, C., Ng, A., Gorbis, E., and Truong, C. (2014). Seismic velocity site characterization of thirty-one Chilean seismometer stations by spectral analysis of surface wave dispersion. *Pacific Earthquake Engineering Research Center*, Technical Report PEER 2014/05.

Kendrick, E., Bevis, M., Smalley Jr, R., Brooks, B., Vargas, R. B., Lauria, E., and Fortes, L. P. S. (2003). The Nazca-South America Euler vector and its rate of change. *Journal of South American Earth Sciences*, 16(2):125–131. DOI: https://doi.org/10.1016/S0895-9811(03)00028-2.

Ko, Y.-T., Kuo, B.-Y., and Hung, S.-H. (2012). Robust determination of earthquake source parameters and mantle attenuation. *Journal of Geophysical Research: Solid Earth*, 117(B4). DOI: https://doi.org/10.1029/2011JB008759.

Konno, K. and Ohmachi, T. (1998). Ground-motion characteristics estimated from spectral ratio between horizontal and vertical components of microtremor. *Bulletin of the Seismological Society of America*, 88(1):228–241. DOI: https://doi.org/10.1785/BSSA0880010228.

Krishna Singh, S., Quintanar-Robles, L., Arroyo, D., Cruz-Atienza, V. M., Espíndola, V. H., Bello-Segura, D. I., and Ordaz, M. (2020). Lessons from a small local earthquake (Mw 3.2) that produced the highest acceleration ever recorded in Mexico City. *Seismological Society of America*, 91(6):3391–3406. DOI: https://doi.org/10.1785/0220200123.

Kusunoki, K. and Kimura, G. (1998). Collision and extrusion at the Kuril-Japan arc junction. *Tectonics*, 17(6):843–858. DOI: https://doi.org/10.1029/98TC02699.

Lay, T., Kanamori, H., Ammon, C. J., Koper, K. D., Hutko, A. R., Ye, L., Yue, H., and Rushing, T. M. (2012). Depth-varying rupture properties of subduction zone megathrust faults. *Journal of Geophysical Research: Solid Earth*, 117(B4). DOI: https://doi.org/10.1029/2011JB009133.

Legrand, D., Delouis, B., Dorbath, L., David, C., Campos, J., Marquez, L., Thompson, J., and Comte, D. (2007). Source parameters of the Mw=6.3 Aroma crustal earthquake of July 24, 2001 (northern Chile), and its aftershock sequence. *Journal of south American earth sciences*, 24(1):58–68. DOI: https://doi.org/10.1016/j.jsames.2007.02.004.

Leyton, F., Leopold, A., Hurtado, G., Pastén, C., Ruiz, S., Montalva, G., and Saéz, E. (2018). Geophysical characterization of the Chilean seismological stations: First results. *Seismological Research Letters*, 89(2A):519–525. DOI: https://doi.org/10.1785/0220170156.

Lomax, A., Virieux, J., Volant, P., and Berge-Thierry, C. (2000). Probabilistic earthquake location in 3D and layered models. *In: Thurber C.H., Rabinowitz N. (Eds.), Advances in Seismic Event Location. Modern Approaches in Geophysics*, 18:101–134. DOI: https://doi.org/10.1007/978-94-015-9536-0_5.

Lomnitz, C. (2004). Major earthquakes of Chile: A historical survey, 1535-1960. *Seismological Research Letters*, 75(3):368–378. DOI: https://doi.org/10.1785/gssrl.75.3.368.

Lund, B. and Townend, J. (2007). Calculating horizontal stress orientations with full or partial knowledge of the tectonic stress tensor. *Geophysical Journal International*, 170(3):1328–1335. DOI: https://doi.org/10.1111/j.1365-246X.2007.03468.x.

Madariaga, R. (1976). Dynamics of an expanding circular fault. *Bulletin of the Seismological Society of America*, 66(3):639–666. DOI: https://doi.org/10.1785/BSSA0660030639.

Maldonado, V., Contreras, M., and Melnick, D. (2021). A comprehensive database of active and potentially-active continental faults in Chile at 1:25,000 scale. *Scientific Data*, 8(1):1–13. DOI: https://doi.org/10.1038/s41597-021-00802-4.

McCaffrey, R. (1992). Oblique plate convergence, slip vectors, and forearc deformation. *Journal of Geophysical Research: Solid Earth*, 97(B6):8905–8915. DOI: https://doi.org/10.1029/92JB00483.

McCaffrey, R. (1996). Estimates of modern arc-parallel strain rates in fore arcs. *Geology*, 24(1):27–30. DOI: https://doi.org/10.1130/0091-7613(1996)024<0027:EOMAPS>2.3.CO;2.

Metois, M., Vigny, C., and Socquet, A. (2016). Interseismic coupling, megathrust earthquakes and seismic swarms along the Chilean subduction zone (38–18 s). *Pure and Applied Geophysics*, 173(5):1431–1449. DOI: https://doi.org/10.1007/s00024-016-1280-5.

Montalva, G. A., Bastías, N., and Rodriguez-Marek, A. (2017). Ground-motion prediction equation for the Chilean subduction zone. *Bulletin of the Seismological Society of America*, 107(2):901–911. DOI: https://doi.org/10.1785/0120160221.

Moreno, M. S., Bolte, J., Klotz, J., and Melnick, D. (2009). Impact of megathrust geometry on inversion of coseismic slip from geodetic data: Application to the 1960 Chile earthquake. *Geophysical Research Letters*, 36(16). DOI: https://doi.org/10.1029/2009GL039276.

Mpodozis, C. and Ramos, V. (1990). The andes of Chile and Argentina. *In G. E. Ericksen, M. T. Cañas Pinochet, and J. A. Reinemund (Eds.), Geology of the Andes and its relation to hydrocarbon and mineral resources, earth science series*, 11:59–90.

Nigam, N. C. and Jennings, P. C. (1969). Calculation of response spectra from strong-motion earthquake records. *Bulletin of the Seismological Society of America*, 59(2):909–922. DOI: https://doi.org/10.1785/BSSA0590020909.

Oncken, O., Asch, G., Haberland, C., Metchie, J., Sobolev, S., Stiller, M., Yuan, X., Brasse, H., Buske, S., Giese, P., et al. (2003). Seismic imaging of a convergent continental margin and plateau in the central Andes (Andean Continental Research Project 1996 (ANCORP'96)). *Journal of Geophysical Research: Solid Earth*, 108(B7). DOI: https://doi.org/10.1029/2002JB001771.

Oth, A., Miyake, H., and Bindi, D. (2017). On the relation of earthquake stress drop and ground motion variability. *Journal of Geophysical Research: Solid Earth*, 122(7):5474–5492. DOI: https://doi.org/10.1002/2017JB014026.

Pagani, M., Monelli, D., Weatherill, G., Danciu, L., Crowley, H., Silva, V., Henshaw, P., Butler, L., Nastasi, M., Panzeri, L., et al. (2014). OpenQuake engine: An open hazard (and risk) software for the global earthquake model. *Seismological Research Letters*, 85(3):692–702. DOI: https://doi.org/10.1785/0220130087.

Park, J., Lindberg, C. R., and Vernon III, F. L. (1987). Multitaper spectral analysis of high-frequency seismograms. *Journal of Geophysical Research: Solid Earth*, 92(B12):12675–12684. DOI: https://doi.org/10.1029/JB092iB12p12675.

Peyrat, S., Campos, J., De Chabalier, J.-B., Perez, A., Bonvalot, S., Bouin, M.-P., Legrand, D., Nercessian, A., Charade, O., Patau, G., et al. (2006). Tarapacá intermediate-depth earthquake (Mw 7.7, 2005, northern Chile): A slab-pull event with horizontal fault plane constrained from seismologic and geodetic observations. *Geophysical Research Letters*, 33(22). DOI: https://doi.org/10.1029/2006GL027710.

Peyrat, S., Madariaga, R., Buforn, E., Campos, J., Asch, G., and Vilotte, J. (2010). Kinematic rupture process of the 2007 Tocopilla earthquake and its main aftershocks from teleseismic and strong-motion data. *Geophysical Journal International*, 182(3):1411–1430. DOI: https://doi.org/10.1111/j.1365-246X.2010.04685.x.

Piña-Valdés, J., Socquet, A., and Cotton, F. (2018a). Insights on the Japanese subduction megathrust properties from depth and lateral variability of observed ground motions. *Journal of Geophysical Research: Solid Earth*, 123(10):8937–8956. DOI: https://doi.org/10.1029/2018JB015743.

Piña-Valdés, J., Socquet, A., Cotton, F., and Specht, S. (2018b). Spatiotemporal variations of ground motion in Northern Chile before and after the 2014 Mw 8.1 Iquique megathrust event. *Bulletin of the Seismological Society of America*, 108(2):801–814. DOI: https://doi.org/10.1785/0120170052.

Prieto, G. A., Parker, R., and Vernon Iii, F. (2009). A Fortran 90 library for multitaper spectrum analysis. *Computers & Geosciences*, 35(8):1701–1710. DOI: https://doi.org/10.1016/j.cageo.2008.06.007.

Rodriguez-Marek, A., Montalva, G. A., Cotton, F., and Bonilla, F. (2011). Analysis of single-station standard deviation using the KiK-net data. *Bulletin of the Seismological Society of America*, 101(3):1242–1258. DOI: https://doi.org/10.1785/0120100252.

Ruegg, J., Campos, J., Armijo, R., Barrientos, S., Briole, P., Thiele, R., Arancibia, M., Canuta, J., Duquesnoy, T., Chang, M., et al. (1996). The Mw=8.1 Antofagasta (North Chile) earthquake of July 30, 1995: first results from teleseismic and geodetic data. *Geophysical Research Letters*, 23(9):917–920. DOI: https://doi.org/10.1029/96GL01026.

Ruiz, S., Klein, E., del Campo, F., Rivera, E., Poli, P., Metois, M., Christophe, V., Baez, J. C., Vargas, G., Leyton, F., et al. (2016). The seismic sequence of the 16 September 2015 Mw 8.3 Illapel, Chile, earthquake. *Seismological Research Letters*, 87(4):789–799. DOI: https://doi.org/10.1785/0220150281.

Ruiz, S. and Madariaga, R. (2011). Determination of the friction law parameters of the Mw 6.7 Michilla earthquake in northern Chile by dynamic inversion. *Geophysical Research Letters*, 38(9). DOI: https://doi.org/10.1029/2011GL047147.

Ruiz, S. and Madariaga, R. (2018). Historical and recent large megathrust earthquakes in chile. *Tectonophysics*, 733:37–56. DOI: https://doi.org/10.1016/j.tecto.2018.01.015.

Ruiz, S., Metois, M., Fuenzalida, A., Ruiz, J., Leyton, F., Grandin, R., Vigny, C., Madariaga, R., and Campos, J. (2014). Intense foreshocks and a slow slip event preceded the 2014 Iquique Mw 8.1 earthquake. *Science*, 345(6201):1165–1169. DOI: https://doi.org/10.1126/science.1256074.

Ruiz, S., Moreno, M., Melnick, D., Del Campo, F., Poli, P., Baez, J., Leyton, F., and Madariaga, R. (2017). Reawakening of large earthquakes in south central Chile: The 2016 Mw 7.6 Chiloé event. *Geophysical Research Letters*, 44(13):6633–6640. DOI: https://doi.org/10.1002/2017GL074133.

Ruiz, S. and Saragoni, G. (2005). Fórmulas de atenuación para la subducción de Chile considerando los dos mecanismos de sismogénesis y los efectos del suelo. *IX Congreso Chileno de Sismología e Ingeniería Antisísmica*, Concepción, Chile, 16-19 November.

Salazar, P., Kummerow, J., Wigger, P., Shapiro, S., and Asch, G. (2017). State of stress and crustal fluid migration related to west-dipping structures in the slab-forearc system in the northern Chilean subduction zone. *Geophysical Journal International*, 208(3):1403–1413. DOI: https://doi.org/10.1093/gji/ggw463.

Sambridge, M. (1999a). Geophysical inversion with a neighbourhood algorithm—I. Searching a parameter space. *Geophysical journal international*, 138(2):479–494. DOI: https://doi.org/10.1046/j.1365-246X.1999.00876.x.

Sambridge, M. (1999b). Geophysical inversion with a neighbourhood algorithm—II. Appraising the ensemble. *Geophysical Journal International*, 138(3):727–746. DOI: https://doi.org/10.1046/j.1365-246x.1999.00900.x.

Scherbaum, F., Cotton, F., and Smit, P. (2004). On the use of response spectral-reference data for the selection and ranking of ground-motion models for seismic-hazard analysis in regions of moderate seismicity: The case of rock motion. *Bulletin of the seismological society of America*, 94(6):2164–2185. DOI: https://doi.org/10.1785/0120030147.

Scherbaum, F., Delavaud, E., and Riggelsen, C. (2009). Model selection in seismic hazard analysis: An information-theoretic perspective. *Bulletin of the Seismological Society of America*, 99(6):3234–3247. DOI: https://doi.org/10.1785/0120080347.

Scholz, C. H. and Campos, J. (2012). The seismic coupling of subduction zones revisited. *Journal of Geophysical Research: Solid Earth*, 117(B5). DOI: https://doi.org/10.1029/2011JB009003.

Schurr, B., Asch, G., Hainzl, S., Bedford, J., Hoechner, A., Palo, M., Wang, R., Moreno, M., Bartsch, M., Zhang, Y., et al. (2014). Gradual unlocking of plate boundary controlled initiation of the 2014 Iquique earthquake. *Nature*, 512(7514):299–302. DOI: https://doi.org/10.1038/nature13681.

Sigbjörnsson, R., Snæbjörnsson, J. T., Higgins, S., Halldórsson, B., and Ólafsson, S. (2009). A note on the Mw 6.3 earthquake in Iceland on 29 May 2008 at 15:45 UTC. *Bulletin of Earthquake Engineering*, 7(1):113–126. DOI: https://doi.org/10.1007/s10518-008-9087-0.

Sippl, C., Schurr, B., Asch, G., and Kummerow, J. (2018). Seismicity structure of the northern Chile forearc from > 100,000 double-difference relocated hypocenters. *Journal of Geophysical Research: Solid Earth*, 123(5):4063–4087. DOI: https://doi.org/10.1002/2017JB015384.

Sobiesiak, M. and Schurr, B. (2007). Tocopilla Project. *GFZ Data Services. Other/Seismic Network*. DOI: https://doi.org/10.14470/L47552843299.

Soto, H., Sippl, C., Schurr, B., Kummerow, J., Asch, G., Tilmann, F., Comte, D., Ruiz, S., and Oncken, O. (2019). Probing the northern Chile megathrust with seismicity: the 2014 M8.1 Iquique earthquake sequence. *Journal of Geophysical Research: Solid Earth*, 124(12):12935–12954. DOI: https://doi.org/10.1029/2019JB017794.

Stafford, P. J., Rodriguez-Marek, A., Edwards, B., Kruiver, P. P., and Bommer, J. J. (2017). Scenario dependence of linear site-effect factors for short-period response spectral ordinates. *Bulletin of the Seismological Society of America*, 107(6):2859–2872. DOI: https://doi.org/10.1785/0120170084.

Strasser, F. O., Abrahamson, N. A., and Bommer, J. J. (2009). Sigma: Issues, insights, and challenges. *Seismological Research Letters*, 80(1):40–56. DOI: https://doi.org/10.1785/gssrl.80.1.40.

Strasser, F. O., Arango, M., and Bommer, J. J. (2010). Scaling of the source dimensions of interface and intraslab subduction-zone earthquakes with moment magnitude. *Seismological Research Letters*, 81(6):941–950. DOI: https://doi.org/10.1785/gssrl.81.6.941.

Tassara, A. and Echaurren, A. (2012). Anatomy of the Andean subduction zone: three-dimensional density model upgraded and compared against global-scale models. *Geophysical Journal International*, 189(1):161–168. DOI: https://doi.org/10.1111/j.1365-246X.2012.05397.x.

Trugman, D. T. and Shearer, P. M. (2018). Strong correlation between stress drop and peak ground acceleration for recent M 1–4 earthquakes in the San Francisco bay area. *Bulletin of the Seismological Society of America*, 108(2):929–945. DOI: https://doi.org/10.1785/0120170245.

Universidad de Chile (2012). Red Sismológica Nacional. *International Federation of Digital Seismograph Networks*. DOI: https://doi.org/10.7914/SN/C1.

Vasyura-Bathke, H., Dettmer, J., Dutta, R., Mai, P. M., and Jonsson, S. (2021). Accounting for theory errors with empirical Bayesian noise models in nonlinear centroid moment tensor estimation. *Geophysical Journal International*, 225(2):1412–1431. DOI: https://doi.org/10.1093/gji/ggab034.

Vasyura-Bathke, H., Dettmer, J., Steinberg, A., Heimann, S., Isken, M. P., Zielke, O., Mai, P. M., Sudhaus, H., and Jónsson, S. (2020). The Bayesian earthquake analysis tool. *Seismological Research Letters*, 91(2A):1003–1018. DOI: https://doi.org/10.1785/0220190075.

Victor, P., Oncken, O., and Glodny, J. (2004). Uplift of the western Altiplano plateau: Evidence from the Precordillera between 20° and 21°S (northern Chile). *Tectonics*, 23(4). DOI: https://doi.org/10.1029/2003TC001519.

Vigny, C., Rudloff, A., Ruegg, J.-C., Madariaga, R., Campos, J., and Alvarez, M. (2009). Upper plate deformation measured by GPS in the Coquimbo Gap, Chile. *Physics of the Earth and Planetary Interiors*, 175(1-2):86–95. DOI: https://doi.org/10.1016/j.pepi.2008.02.013.

Wada, I. and Wang, K. (2009). Common depth of slab-mantle decoupling: Reconciling diversity and uniformity of subduction zones. *Geochemistry, Geophysics, Geosystems*, 10(10). DOI: https://doi.org/10.1029/2009GC002570.

Wang, R. (1999). A simple orthonormalization method for stable and efficient computation of Green's functions. *Bulletin of the Seismological Society of America*, 89(3):733–741.

Weichert, D. H. (1980). Estimation of the earthquake recurrence parameters for unequal observation periods for different magnitudes. *Bulletin of the Seismological Society of America*, 70(4):1337–1346. DOI: https://doi.org/10.1785/BSSA0700041337.

Wessel, P., Smith, W. H., Scharroo, R., Luis, J., and Wobbe, F. (2013). Generic mapping tools: improved version released. *Eos, Transactions American Geophysical Union*, 94(45):409–410. DOI: https://doi.org/10.1002/2013EO450001.

Wigger, P., Salazar, P., Kummerow, J., Bloch, W., Asch, G., and Shapiro, S. (2016). West–Fissure- and Atacama-Fault Seismic Network (2005/2012). *Deutsches GeoForschungsZentrum GFZ. Other/Seismic Network*. DOI: https://doi.org/10.14470/3S7550699980.

Yoshida, K., Hasegawa, A., and Okada, T. (2015). Spatial variation of stress orientations in NE Japan revealed by dense seismic observations. *Tectonophysics*, 647:63–72. DOI: https://doi.org/10.1016/j.tecto.2015.02.013.

Yuan, X., Sobolev, S. V., Kind, R., Oncken, O., Bock, G., Asch, G., Schurr, B., Graeber, F., Rudloff, A., Hanka, W., et al. (2000). Subduction and collision processes in the Central Andes constrained by converted seismic phases. *Nature*, 408(6815):958–961. DOI: https://doi.org/10.1038/35050073.

Zhao, J. X., Zhang, J., Asano, A., Ohno, Y., Oouchi, T., Takahashi, T., Ogawa, H., Irikura, K., Thio, H. K., Somerville, P. G., et al. (2006). Attenuation relations of strong ground motion in Japan using site classification based on predominant period. *Bulletin of the Seismological Society of America*, 96(3):898–913. DOI: https://doi.org/10.1785/0120050122.